Optical readout and control of correlated electron phases in 2D semiconductor moiré superlattices

William G. Holtzmann

A dissertation
submitted in partial fulfillment of the
requirements for the degree of

Doctor of Philosophy

University of Washington
2025

Reading Committee:
Xiaodong Xu, Chair
David Cobden
Ting Cao

Program Authorized to Offer Degree:
Department of Physics

University of Washington

Abstract

Optical readout and control of correlated electron
phases in 2D semiconductor moiré superlattices

William G. Holtzmann

Chair of the Supervisory Committee:
Xiaodong Xu
Department of Physics

Ever since the isolation of the first single layer of a van der Waals material in 2004, the field of 2D materials has been continuously accelerating. The ever-growing list of correlated electronic phenomena observed in 2D materials, and in particular 2D moiré systems, has created a sandbox for fundamental condensed matter research. Combined with the unique optoelectronic properties of the transition metal dichalcogenides (TMDs), we now have unprecedented access to correlated electronic phases with optical probes and optical controls. In this dissertation two main projects will be presented. First, Raman scattering experiments on WS_2/WSe_2 moiré heterobilayers have revealed two emergent scattering modes that are as of now unidentified. These Raman modes show evidence of coupling with the underlying correlated physics in the moiré system in addition numerous unusual and uncommon Raman signatures, including an anti-symmetric Raman tensor and a distinct excitation power dependence for the scattering cross section of the modes. Second, optical probes, and more importantly optical control, of the integer and fractional Chern insulator states in $tMoTe_2$ will be presented. By leveraging the unique spin-valley-polarization coupling of the TMDs, we demonstrate the ability to deterministically choose the magnetization direction and

thus sign of the Chern number for a domain encompassed by our optical pump. This represents the first step in optically controlling correlated electron phases in 2D materials rather than just optically probing them.

Contents

List of Figures

Acknowledgments

First and foremost, I would like to thank my PhD advisor Professor Xiaodong Xu. I don't think I can thank you enough for the opportunities you provided me with in your lab. I am constantly in awe of your ability to not only keep track of all the different projects across our group and collaborators, but also you constant effort to help each of your students succeed. It is obvious to me that you care for each and everyone one of your students, and the success of your former students in their ventures after their PhD is a testament to your ability to help us grow and improve in our scientific abilities while here.

Next, I would like to thank Professors Ting Cao, Dave Cobden, Daniel Gamelin, Mark Rudner, and Subhadeep Gupta for serving on my PhD supervisory committee. I appreciate all of you taking the time to serve on my committee and put up with my 5 reminder emails about my general and final exam. In particular, I would also like to thank Professors Ting Cao and Dave Cobden for taking on the extra burden of serving on my reading committee.

I want to extend a thank you to all my long-time friends who have stayed in touch during these past 5 years and made anywhere I saw them feel like home. Joel, Tom, Liz, Kyle, Reyn, Matt, Marianne, Kaylene, and so many others, thank you for always being there for me.

To my friends Adam and Ansh, thank you not just for your friendship these past 5 years, but also for providing much needed perspective and reassurance during my PhD while you both were pursuing your own at the same time. It's always nice getting to talk about research that isn't my own, even if particle physics is a bit too complicated for me and biology is, well, biology.

I can't say thank you enough to my friend Hannah, who has been with me every step of the way

during this journey. Even if most of our communication was in the form of one to two word text messages, your constant friendship was a reminder of home and a light during even the most difficult days of my PhD.

Finally, I want to thank my family. Mom, dad, and Jake, you're constant, unwavering support made all of this possible. It's been such a blessing to get to live with Jake the past three years. I love you all so much and hope that one day I'll be able to repay a tenth of what you've done for me these past 5 years.

Chapter 1
Introduction

Although the field of 2D materials is often said to have only begun recently, the first observation of a single layer of graphene was as early as 1975 [1]. However, it was not until 2004 that a monolayer of graphene was isolated [2] so that it could be studied alone [3, 4], independent of whatever substrate or bulk crystal it came from.

The isolation of monolayer graphene led to an explosion in the isolation and identification of 2D materials, with multiple other layered materials being reported to have been exfoliated to the monolayer limit within a year [5].

The next revolution for the field came in 2010, when graphene was transferred onto a thin piece of hBN [6]. By incorporating the graphene into a heterostructure consisting of other 2D materials, it was ensured that the surface the graphene sat on would be as atomically flat and pristine as it was.

During this time, proposals were starting to come out for twisting one layer of graphene on top of another to generate moiré patterns [7, 8]. And while moiré patterns weren't a new concept, indeed moiré patterns from graphene on graphite had been observed more than 10 years prior in the 90s [9], the prediction of exciting new physics due to the presence of the moiré was new.

While the moiré concept took time to develop, transition metal dichalcogenides, or TMDs for short, had their unique optoelectronic properties in the monolayer limit revealed [10] and studied [11–13].

As the field continued to develop, with more layers being added to devices every year, the final piece of the puzzle fell into place with the experimental discovery of correlated electronic phases

in a moiré system, namely magic-angle twisted bilayer graphene [14, 15]. Just a few years later, correlated electronic phases in TMD moiré s were found [16, 17].

At the same time theoretical studies on TMD moiré systems continued to push experiments forward with the realization of the potential for topology and Chern insulators, and potentially even fractional Chern insulators at zero field, to exist in the twisted TMDs [18]. This eventually led to the experimental realization of fractional Chern insulators at zero field in $tMoTe_2$ [19, 20] with numerous experimental probes confirming and studying the correlated electronic phase [21, 22]. Shortly after, fractional Chern insulators at zero field were discovered in a graphene-based system [23], bringing the field full circle back to graphene.

1.1 Outline of the dissertation

The remainder of this dissertation is divided into 5 chapters. Chapter 2 will provide a brief overview of the theory behind optical probes and light-matter interaction, starting with a discussion of normal-incidence reflection as a simple example of an optical probe. Then the Drude model will be introduced as a starting point for understanding the microscopic theory of light-matter interaction before interband transitions are used as a way to discuss light-matter interaction from a quantum mechanical perspective.

Chapter 3 will provide an overview and history of the TMD family of 2D materials, with special focus on TMDs in the 2H crystal phase. This chapter begins with a discussion of the monolayer TMD optoelectronics, with a focus on spin-valley physics and excitonic physics. After that, TMD multilayers and heterostructures will be introduced, but moiré heterostructures will be intentionally delayed until the final section of Chapter 3. This final section of Chapter 3 will be divided into two parts: homobilayer moiré s and heterobilayer moiré s. Each part will go through some of the basic theory used to describe the moiré system in question before discussing recent experimental results in the systems.

Chapter 4 will discuss anomalous Raman signatures of WS_2/WSe_2 moiré heterobilayers. The chapter will begin with establishing that these anomalous Raman signatures do indeed arise due to the moiré, as well as evidence for connection between the scattering modes and the charge order in the WS_2/WSe_2 moiré system. Afterwards, additional data that only further complicates the story will be introduced before briefly discussing possible explanations for the unusual Raman signatures.

Chapter 5 is an intermediary chapter focused on giving a brief overview of optical probes of $tMoTe_2$. The chapter will begin with a discussion of how photoluminescence (PL) can be used as a way to detect gapped and incompressible states in $tMoTe_2$. Then methods to optically detect ferromagnetic phases in $tMoTe_2$ will be discussed. The chapter will end with a discussion about two different data sets. The first of the data sets will be reflectance data that bears the signature of a dipolar exciton, despite being far from neutral doping. The second set of data will show an unusual paramagnetic response of one of the excitons in a smaller twist angle $tMoTe_2$ device.

Finally, Chapter 6 will discuss recent experiments on optically controlling the integer and fractional Chern insulator states in $tMoTe_2$. First, an overview of the experiment will be given, before a presentation of data demonstrating the ability to optically initialize spin-up or spin-down domains on demand in $tMoTe_2$. Next, data demonstrating the ability to not just initialize a domain with the desired sign of the Chern number but instead directly switch a domain from being spin-up to spin-down and back again will be presented. This will be followed by an outlook on the future of optical control experiments.

Chapter 2
Optical probes of 2D materials

The primary reference for sections 2.1 to 2.3 is Dresselhaus, Dresselhaus, Cronin, and Souza Filho's *Solid State Properties* [24]. The primary reference for section 2.4 is Yu and Cardona's *Fundamentals of Semiconductors* [25].

2.1 An introduction to light-matter interaction

The amount of information we can extract from a given experiment relies on our knowledge of how our probe couples to the properties we are investigating. In the case of optical probes of solid state systems, their interaction is mediated exclusively by electromagnetism. So, the natural starting point for understanding of light-matter interactions is Maxwell's equations, which in SI units are

$$\nabla \times \boldsymbol{H} - \frac{\partial \overrightarrow{D}}{\partial t} = \boldsymbol{j} \tag{2.1}$$

$$\nabla \times \boldsymbol{E} + \frac{\partial \boldsymbol{B}}{\partial t} = 0 \tag{2.2}$$

$$\nabla \cdot \boldsymbol{D} = 0 \tag{2.3}$$

$$\nabla \cdot \boldsymbol{B} = 0 \tag{2.4}$$

The charge density has been assumed to be zero in the above equations, which is true for a solid on the length scale of optical probes. Additionally, we will assume that the electric displacement field

$\boldsymbol{D}$, the magnetic field $\boldsymbol{B}$, and the current density $\boldsymbol{j}$ inside of the material are all linearly related to $\boldsymbol{E}$, $\boldsymbol{H}$, and $\boldsymbol{E}$, respectively, allowing us to write:

$$\boldsymbol{D} = \epsilon \boldsymbol{E} \tag{2.5}$$

$$\boldsymbol{B} = \mu \boldsymbol{H} \tag{2.6}$$

$$\boldsymbol{j} = \sigma \boldsymbol{E} \tag{2.7}$$

The assumption of linearity is valid in the case of low intensity optical probes, which will apply to all optical probes used in this dissertation.

From the above equations, we can obtain an equation for an optical field in the material

$$\boldsymbol{E} = \boldsymbol{E_0} e^{i(\boldsymbol{K}\cdot\boldsymbol{r} - \omega t)} \tag{2.8}$$

where ω is the frequency of the light and $\boldsymbol{K}$ is the complex propagation constant. Further manipulation of the above equations eventually yields

$$\boldsymbol{K} = \frac{\omega}{c}\sqrt{\epsilon_c \mu}\widehat{z} \tag{2.9}$$

where $\widehat{z}$ is the direction of propagation and ϵ_c is material's complex dielectric function, defined as

$$\epsilon_c(\omega) = \epsilon + \frac{i\sigma}{\omega} = \epsilon_1 + i\epsilon_2 \tag{2.10}$$

It is also customary to define the complex optical conductivity, σ_c, and and the complex index of refraction, $\widetilde{N}$:

$$\sigma_c(\omega) = \sigma - i\epsilon\omega = \sigma_1 + i\sigma_2 \tag{2.11}$$

$$\widetilde{N}(\omega) = c\sqrt{\mu\epsilon_c} = \widetilde{n}(\omega) + i\widetilde{k}(\omega) \tag{2.12}$$

Equation (2.12) can also be rearranged to yield equations for the real and imaginary parts of ϵ_c as

$$\epsilon_1 = \widetilde{n}^2 - \widetilde{k}^2 \tag{2.13}$$

$$\epsilon_2 = 2\widetilde{n}\widetilde{k} \tag{2.14}$$

Substitution of Eq. (2.9) and Eq. (2.12) back into Eq. (2.8) yields

$$\boldsymbol{E}(z,t) = \boldsymbol{E_0} e^{-\frac{\omega}{c}\widetilde{k}z} e^{i(\frac{\omega}{c}\widetilde{n}z - \omega t)} \tag{2.15}$$

where it becomes clear that $\widetilde{n}(\omega)$ is the frequency dependent index of refraction and $\widetilde{k}(\omega)$, the extinction coefficient, determines how quickly the optical field attenuates inside the material.

With Eq. (2.15), we can confidently relate the properties of our optical probe to the frequency and material dependent properties $\widetilde{N}$, ϵ_c, and ω_c. The challenges now are understanding how to use these relations in a real experiment and understanding how these properties relate to the specific information we would like to learn about our material of interest, for example carrier mass, lattice impurities, phonon energies, etc.

2.2 A simple example - reflection

Perhaps the simplest example of an optical experiment is normal-incidence reflection. While straightforward, reflection measurements can reveal a significant amount of information about a material's optical properties.

To obtain an equation for the reflection of linearly polarized light with frequency ω from a material with complex index of refraction $\widetilde{N}(\omega)$, we first simplify our problem by assuming that the material is thick enough such that the light transmitted into the material is fully attenuated inside of the material, allowing us to consider only three optical fields: the incident light in free space, the reflected light in free space, and the transmitted light inside of the material. Thus, we can write the total electric field outside of the material and inside of the material as

$$E_{out} = E_0 e^{i(\frac{\omega}{c}z - \omega t)} + E_r e^{i(-\frac{\omega}{c}z - \omega t)} \tag{2.16}$$

$$E_{in} = E_{abs} e^{i(\frac{\omega}{c\widetilde{N}z - \omega t})} \tag{2.17}$$

where the light is assumed to be linearly polarized and E_0, E_r, and E_{abs} are the amplitudes of the electric field of the incident, reflected, and absorbed light, respectively.

The continuity of the electric field at the surface of the material requires

$$E_0 + E_r = E_{abs} \tag{2.18}$$

while the continuity of the magnetic field combined with Eq. (2.2) imposes a continuity relation on the derivative of the electric field with respect to z, resulting in

$$\frac{i\omega}{c}E_0 + \frac{i\omega}{c}E_r = \frac{i\omega}{c}\widetilde{N}E_{abs} \tag{2.19}$$

Using Eq. (2.18) and Eq. (2.19), we can obtain equations for E_0 and E_r in terms of E_{abs}

$$E_0 = \frac{1}{2}E_{abs}(1+\widetilde{N}) \tag{2.20}$$

$$E_r = \frac{1}{2}E_{abs}(1-\widetilde{N})E_{abs} \tag{2.21}$$

Since a material's reflectivity $\mathscr{R}$ is defined as the ratio of the incident and reflected intensities of light, we can now obtain an equation for a material's normal-incidence reflectivity as

$$\mathscr{R} = \left|\frac{E_r}{E_0}\right|^2 = \left|\frac{1-\widetilde{N}}{1+\widetilde{N}}\right|^2 = \frac{(1-\widetilde{n})^2+\widetilde{k}^2}{(1+\widetilde{n})^2+\widetilde{k}^2} \tag{2.22}$$

where $\widetilde{N}(\omega) = \widetilde{n}(\omega) + i\widetilde{k}(\omega)$ is once again the material's complex index of refraction.

2.3 Optical response of free carriers - the Drude model

In metals and semiconductors, free carriers often play an important role in a material's response to light in the visible and below frequency bands. Perhaps the simplest model that still captures the essentials of the optical response of free carriers is the Drude model.

The starting point for the Drude model is to consider the classical equation of motion for an electron in an optical field of amplitude E_0 and frequency ω, which is given by

$$m\frac{d\boldsymbol{v}}{dt} + \frac{m\boldsymbol{v}}{\tau} = e\boldsymbol{E_0}e^{-i\omega t} \tag{2.23}$$

where the relaxation time τ is used to add a phenomenological damping term, $m\boldsymbol{v}/\tau$. By assuming

the electrons undergo a sinusoidal motion described by $\boldsymbol{v} = \boldsymbol{v_0} e^{-i\omega t}$ and substituting into Eq. (2.23), we obtain an equation for the drift velocity $\boldsymbol{v_0}$:

$$\boldsymbol{v_0} = \frac{e\boldsymbol{E_0}}{-mi\omega + \dfrac{m}{\tau}} \tag{2.24}$$

The current density $\boldsymbol{j}$ is then given by

$$\boldsymbol{j} = ne\boldsymbol{v_0} \tag{2.25}$$

where n is the carrier density.

Substituting into Eq. (2.7) yields an equation for the complex electrical conductivity:

$$\sigma_c = \frac{ne^2\tau}{m(1 - i\omega\tau)} \tag{2.26}$$

In the limit of $\omega \to 0$, Eq. (2.26) reduces to the Drude model formula for the material's DC conductivity. In the case where there are multiple types of free carriers in a material, their contributions to the optical conductivity are summed together.

For a real material, two primary changes need to be made. First, the conductivity is a second rank tensor with a form determined by the crystal symmetries. Second, the mass above should be replaced by the effective mass m^* of the free carriers. The effective mass, also a second rank tensor, is related to the curvature of the energy band of the free carrier by

$$\left(\frac{1}{m^*}\right)_{\alpha\beta} = \frac{1}{\hbar}\frac{\partial^2 E(\boldsymbol{k})}{\partial k_\alpha \partial k_\beta} \tag{2.27}$$

If the only contribution to the material's conductivity is the Drude free carrier contribution, then we

can substitute Eq. (2.26) into Eq. (2.10) to obtain the following equation for the dielectric function

$$\epsilon_c(\omega) = \epsilon_{core}(\omega) + \frac{i}{\omega}\frac{ne^2\tau}{m^*(1-i\omega\tau)} \tag{2.28}$$

where $\epsilon_{core}(\omega)$ encapsulates all other contributions to the dielectric function. Like the optical conductivity, $\epsilon_c(\omega)$ is once again a second-rank tensor in a real material. Away from resonances, such as optically active phonon frequencies and interband transitions, $\epsilon_{core}(\omega)$ can generally be approximated by the value of the material's DC dielectric constant $\epsilon_{core}(0) = \epsilon_r(0)\epsilon_0$.

It is instructive to examine the low and high frequency response of a material's reflectivity based on Eq. (2.28). In the low frequency limit, where $\omega\tau \ll 1$, we can Taylor expand Eq. (2.28) about $\omega\tau = 0$ to obtain

$$\epsilon_c(\omega) \simeq \epsilon_{core}(\omega) + \frac{ine^2\tau}{m^*\omega} \tag{2.29}$$

As ω approaches 0, the free carrier contribution to ϵ_c grows as $\frac{1}{\omega}$ and thus dominates over ϵ_{core} for low frequencies. As a result,substituting into Eq. (2.12) gives us

$$\widetilde{N} = \widetilde{n} + i\widetilde{k} \simeq \sqrt{\frac{ine^2\tau}{\epsilon_0 m^*\omega}} \tag{2.30}$$

which, after separating into real and imaginary components, gives

$$\widetilde{n} = \widetilde{k} \simeq \sqrt{\frac{ne^2\tau}{2\epsilon_0 m^*\omega}} \tag{2.31}$$

Since both $\widetilde{n}$ and $\widetilde{k}$ go as $\frac{1}{\sqrt{\omega}}$ in the low frequency limit, they will both be large, allowing us to simplify Eq. (2.22) to

$$\mathscr{R}(\omega \ll \frac{1}{\tau}) \simeq \frac{(1-\widetilde{n})^2+\widetilde{k}^2}{(1+\widetilde{n})^2+\widetilde{k}^2} \simeq 1 - \frac{4\widetilde{n}}{\widetilde{n}^2+\widetilde{k}^2} \simeq 1 - \frac{2}{\widetilde{n}} = 1 - 2\sqrt{\frac{2\epsilon_0 m^* \omega}{ne^2\tau}} \tag{2.32}$$

As can be seen in Eq. (2.32), in materials with a high number of free carriers n, the reflectivity $\mathscr{R}$ is near unity in the low frequency regime. In other words, metals and small band gap semiconductors behave as mirrors for low frequencies of light.

In the high frequency limit, where $\omega\tau \gg 1$, Eq. (2.28) can instead be approximated by Taylor expanded about $\frac{1}{\omega\tau} = 0$, resulting in

$$\epsilon_c(\omega) \simeq \epsilon_{core}(\omega) - \frac{ne^2}{m^*\omega^2} \tag{2.33}$$

As the free carrier contribution decreases as $\frac{1}{\omega^2}$ when $\omega \gg 1$, we are left with only the core dielectric contribution ϵ_{core}. As metioned earlier, assuming there aren't any resonances in the frequency range being probed, ϵ_{core} can be approximated as the DC dielectric constant, which is a real number. This implies that the extinction coefficient $\widetilde{k}$ drops to zero and the material behaves as a dielectric in the high frequency limit with near zero attenuation for the transmitted light and a reflectivity of

$$\mathscr{R}(\omega \gg \frac{1}{\tau}) \simeq \frac{(1-\widetilde{n})^2}{(1+\widetilde{n})^2} \simeq \frac{(\sqrt{\epsilon_{core}(0)/\epsilon_0}-1)^2}{(\sqrt{\epsilon_{core}(0)/\epsilon_0}+1)^2} \tag{2.34}$$

Generally, the optical response of metals is reasonably well described by the Drude model. However, for semiconductors like the 2D transition metal dichalcogenides that will be discussed in the remaining chapters, interband and in-gap transitions play very important roles in their optical responses.

2.4 Interband transitions

To discuss interband transitions, it becomes necessary to move away from the Drude model. In this section, the Bloch electrons inside of the material will be treated quantum mechanically in the presence of a classical electromagnetic field. The Hamiltonian for a single electron in the presence of some potential $V(r)$ is

$$\mathscr{H}_0 = \frac{p^2}{2m} + V(r) \tag{2.35}$$

We ad in the vector and scalar potentials, $\boldsymbol{A}(\boldsymbol{r}, t)$ and $\Phi(\boldsymbol{r}, t)$, to describe the electromagnetic fields. By choosing the Coulomb gauge, which requires that $\Phi = 0$ and $\nabla \cdot \boldsymbol{A} = 0$, the electric and magnetic fields are given by

$$\boldsymbol{E} = -\frac{\partial \boldsymbol{A}}{\partial t} \tag{2.36}$$

$$\boldsymbol{B} = \nabla \times \boldsymbol{A} \tag{2.37}$$

We now obtain the Hamiltonian for an electron in the presence of an electromagnetic field by replacing $\boldsymbol{p}$ in Eq. (2.35) with $\boldsymbol{p} + e\boldsymbol{A}$, resulting in

$$\mathscr{H} = \frac{(\boldsymbol{p} + e\boldsymbol{A})^2}{2m} + V(r) \tag{2.38}$$

The first term in the Hamiltonian can be expanded to give

$$\frac{(\boldsymbol{p} + e\boldsymbol{A})^2}{2m} = \frac{p^2}{2m} + \frac{e}{2m}\boldsymbol{A} \cdot \boldsymbol{p} + \frac{e}{2m}\boldsymbol{p} \cdot \boldsymbol{A} + \frac{e^2 A^2}{2m} \tag{2.39}$$

Under typical optical excitation, we can drop the final term of Eq. (2.39) since it is quadratic in $\boldsymbol{A}$ and thus negligible for a weak perturbation. Additionally, expanding the term $\boldsymbol{p} \cdot \boldsymbol{A}$ using the definition of the momentum operator, $\boldsymbol{p} = (\hbar/i)\nabla$, and the fact that for our gauge, $\nabla \cdot \boldsymbol{A} = 0$, we can find that $\boldsymbol{p} \cdot \boldsymbol{A} = \boldsymbol{A} \cdot \boldsymbol{p}$, allowing us to simplify Eq. (2.38) into

$$\mathscr{H} = \frac{p^2}{2m} + \frac{e}{m}\boldsymbol{A} \cdot \boldsymbol{p} + V(r) = \mathscr{H}_0 + \frac{e}{m}\boldsymbol{A} \cdot \boldsymbol{p} \tag{2.40}$$

This has allowed us to isolate the interaction term for the Hamiltonian, which is

$$\mathscr{H}_{eR} = \frac{e}{m}\boldsymbol{A} \cdot \boldsymbol{p} \tag{2.41}$$

and is often referred to as the electron-radiation interaction Hamiltonian. From here, we proceed with the assumption that $\boldsymbol{A}$ is weak enough that time-dependent perturbation theory is applicable. Then, we take $\mathscr{H}_{eR}$ as our time-dependent perturbation and calculate the probability rate R of exciting an electron in a valance band state $|v\rangle$ to a conduction band state $|c\rangle$ using Fermi's Golden Rule, given by

$$R = \frac{2\pi}{\hbar} \sum_{\boldsymbol{k_c}, \boldsymbol{k_v}} |\langle c| \mathscr{H}_{eR} |v\rangle|^2 \, \delta(E_c(\boldsymbol{k}) - E_v(\boldsymbol{k}) - \hbar\omega) \tag{2.42}$$

where the sum is over all states in the valence and conduction bands that have an energy difference $E_c(\boldsymbol{k}) - E_v(\boldsymbol{k})$ that matches the energy of the incoming photons $\hbar\omega$. To evaluate this, we start with the matrix element of the electron-radiation interaction Hamiltonian between any pair of valence and conduction band states:

$$|\langle c| \mathscr{H}_{eR} |v\rangle|^2 = \left(\frac{e}{m}\right)^2 |\langle c| \boldsymbol{A} \cdot \boldsymbol{p} |v\rangle|^2 \tag{2.43}$$

From Eqs. (2.15) and (2.36), we can see that the amplitude of the vector potential A is given by

$$A\widehat{e} = -\frac{E_0}{2\omega}\left(e^{i(\boldsymbol{K}\cdot\boldsymbol{r}-\omega t)} + c.c.\right)\widehat{e} \tag{2.44}$$

where $\widehat{e}$ is the unit vector in the direction of the vector field and $c.c.$ is the complex conjugate to account for both incoming and outgoing radiation. We can also write the Bloch wavefunctions for electrons in the valance and conduction bands, respectively

$$|v\rangle = u_{v,\boldsymbol{k_v}}(\boldsymbol{r})e^{i(\boldsymbol{k_v}\cdot\boldsymbol{r})} \tag{2.45}$$

$$|c\rangle = u_{c,\boldsymbol{k_c}}(\boldsymbol{r})e^{i(\boldsymbol{k_c}\cdot\boldsymbol{r})} \tag{2.46}$$

Inserting Eqs. (2.44) to (2.46) into Eq. (2.43) and integrating over all space gives

$$\left|\langle c|\,\mathscr{H}_{eR}\,|v\rangle\right|^2 = \frac{|E|^2}{4\omega^2}\left|\int u^*_{c,\boldsymbol{k_c}}e^{i(\boldsymbol{K}-\boldsymbol{k_c})\cdot\boldsymbol{r}}(\widehat{e}\cdot\boldsymbol{p})u_{v,\boldsymbol{k_v}}e^{i\boldsymbol{k_v}\cdot\boldsymbol{r}}dr\right|^2 \tag{2.47}$$

Through select application of Bloch's theorem as well as assuming that $\boldsymbol{K}$ is small relative to wavevectors in the crystal, which is known as the electric-dipole approximation and is well satisfied for visible or longer wavelength photons, we eventually arrive at

$$\left|\langle c|\,\mathscr{H}_{eR}\,|v\rangle\right|^2 = \left(\frac{e}{m}\right)^2|A|^2|P_{cv}|^2 \tag{2.48}$$

where we have replaced $\left|\langle c|\,\widehat{e}\cdot\boldsymbol{p}\,|v\rangle\right|^2$ with $|P_{cv}|^2$ as the matrix element in question can be approximated as being independent of $\boldsymbol{k}$. A more complete derivation of Eq. (2.48) can be found in Yu and Cardona's *Fundamentals of Semiconductors* [25].

Substituting Eq. (2.48) back into Eq. (2.42) yields

$$R = \frac{2\pi}{\hbar}\left(\frac{e}{m\omega}\right)^2 \left|\frac{E(\omega)}{2}\right|^2 \sum_k |P_{cv}|^2 \delta(E_c(\boldsymbol{k}) - E_v(\boldsymbol{k}) - \hbar\omega) \tag{2.49}$$

which is the probability per unit time per unit volume of a photon of frequency ω being absorbed via an interband transition in the material of interest. By multiplying this quantity by $\hbar\omega$, we can arrive at the rate of power loss for the incident light. Notably, we can arrive at a different expression for the same quantity by taking the derivative with respect to time of the intensity of the optical field inside the material. Squaring Eq. (2.15) gives an equation for the intensity of the light within a material, which is

$$I(z) = I_0 e^{-2\frac{\omega}{c}\widetilde{k}z} \tag{2.50}$$

Taking the derivative of Eq. (2.50) with respect to time and then evaluating it at the surface of the material yields

$$\left.\frac{dI}{dt}\right|_{z\to 0} = \frac{dI}{dz}\frac{dz}{dt} = -2I_0\frac{\omega\widetilde{k}}{\widetilde{n}} \tag{2.51}$$

We can further substitute Eq. (2.14) into Eq. (2.51) to obtain the rate of absorption as a function of the imaginary part of the material's dielectric function:

$$\left.\frac{dI}{dt}\right|_{z\to 0} = -I_0\frac{\epsilon_2\omega}{\widetilde{n}^2} \tag{2.52}$$

Since the rate R of absorption given by Fermi's Golden Rule is per unit volume, we need I to be per unit volume as well, which is given as

$$I = \frac{\widetilde{n}^2}{8\pi}|E(\omega)|^2 \tag{2.53}$$

Finally, substituting Eq. (2.53) into Eq. (2.52) and setting it equal to the rate of absorption $R\hbar\omega$ calculated from Fermi's Golden Rule, we obtain an equation for ϵ_2:

$$\epsilon_2(\omega) = \frac{8\pi\hbar}{|E(\omega)|^2} R = \left(\frac{2\pi e}{m\omega}\right)^2 \sum_k |P_{cv}|^2 \delta(E_c(\boldsymbol{k}) - E_v(\boldsymbol{k}) - \hbar\omega) \tag{2.54}$$

The Kramers-Kronig Relationships allow us to use ϵ_2 to find ϵ_1 as well. Doing so yields

$$\epsilon_1(\omega) = 1 + \frac{4\pi e^2}{m} \left[\sum_k \left(\frac{2}{m\hbar\omega_{cv}}\right) \frac{|P_{cv}|^2}{\omega_{cv}^2 - \omega^2}\right] \tag{2.55}$$

From here, it is possible to substitute substitute Eqs. (2.54) and (2.55) into Eq. (2.11) and add it as a correction to the optical conductivity for free carriers derived using the Drude model in Eq. (2.26).

Chapter 3
Transition metal dichalcogenides

The transition metal dichalcogenides (TMDs) are materials with three atoms in their unit cell and the chemical makeup MX_2, where M is a transition metal and X is a chalcogen atom. Research on materials in the TMD family is not new, with the structure a TMD called molybdenite, better known today as MoS_2, first determined in 1923 [26]. By the 60s there were near 60 different TMDs identified, with about two-thirds of them having been identified to have a layered structure [27]. While not realized at the time, the layered nature of these materials would lead to TMDs becoming one of the most promising platforms for exploring optoelectronics, correlated electronic physics, and more.

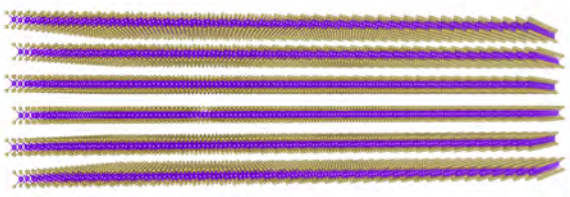

Figure 3.1: Perspective view of 6 layers of a 2H-MoS_2 crystal. Image created using VESTA 3 [28].

The isolation of the first atomically thin material, graphene, from a layered material in 2004 using little more than tape and a microscope [2] created a mad dash for the isolation of monolayers of all different layered materials. Figure 3.1 shows a to-scale illustration of 6 layers of a 2H-MoS_2 crystal and demonstrates what is meant by ”layered” material. The weak interlayer bonds meant mechanical exfoliation could easily separate layers from each other, and just a year after graphene was isolated, monolayers of two TMDs, including MoS_2, were exfoliated and studied [5]. The

basics of these monolayers will be explained in the first section of this chapter, with a focus on the unique optical properties of the 2H-phase monolayer TMDs.

The second chapter will then explore recent advances in the understanding of both natural multilayers of TMDs and TMDs inside of heterostructures. TMD moiré heterostructures will then be discussed in section three with a focus on recent correlated electronic phenomena discovered in both homobilayer and heterobilayer TMD moiré systems.

3.1 Monolayer physics

Monolayer TMDs exist in three main crystal phases. There is the 2H phase, shown in Fig. 3.2a and b, which include the semiconducting TMDs and will be the main focus of this dissertation. As such, we will briefly overview the other two phases before coming back to the 2H phase.

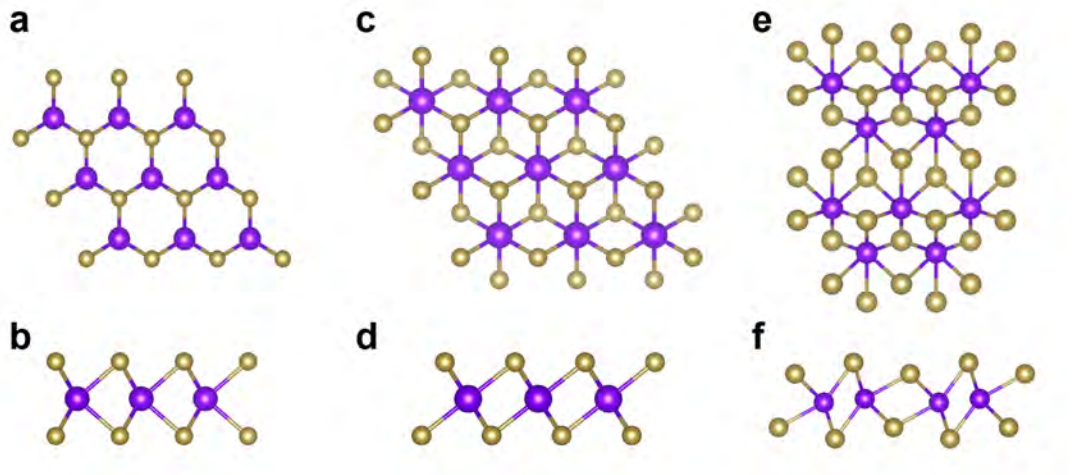

Figure 3.2: Different crystallographic phases for TMDs. Purple atoms represent the transition metal atoms and gold atoms represent the chalcogen atoms. a) Top- and b) side-views of a 2H phase TMD, such as 2H-MoS_2. c) Top- and d) side-views of a 1T phase TMD, such as 1T-TaS_2. e) Top- and f) side-views of a 1T' phase TMD, such as 1T'-WTe_2. Lattice images created using VESTA 3 [28].

Besides the 2H phase, some TMDs exist in the 1T crystal structure, shown in Fig. 3.2c and d. Examples of 1T TMDs include 1T-TaS_2 and 1T-$TaSe_2$, which both host various charge density waves

(CDWs) phases in bulk crystals [29]. 1T-TaS_2 has a particularly rich electronic phase diagram, hosting multiple types of CDW phases, a Mott state at low temperature, and metallic and superconducting phases when the interlayer coupling is tuned via high pressures [30]

The 1T' phase TMDs, with 1T'-WTe_2 taking the forefront of recent interest, have crystal structures as shown in Fig. 3.2e and f. Monolayer 1T'-WTe_2 was reported to have the transport signatures of a topological insulator [31, 32], followed by numerous other experiments confirming the signatures of topology in WTe_2 [33–35]. Additionally, gating monolayer WTe_2 revealed a nearby superconducting phase [36] and revealed the hallmarks of ferroelectricity in two- and three-layer WTe_2 [37].

Of course, this is just a small selection from an vast body of literature on non 2H phase TMDs, but demonstrates that the rich physics of the TMDs is not limited to the 2H phase TMDs. That being said, all experimental results reported in this dissertation will be on 2H semiconducting TMDs, so we will now turn our focus to those for the remainder of this chapter.

While monolayer 2H phase TMDs like MoS_2 have been studied since 2005 [5], the extent of the unique optoelectronic coupling that occurs in monolayer TMDs was not fully realized until 2012, when spin-valley locking, and importantly selective optical coupling based on light's polarization was predicted [10] and experimentally confirmed and confirmed via experiments [11–13].

3.1.1 Spin-valley locking

As shown in Fig. 3.2a and b, 2H TMDs have a hexagonal crystal structure and monolayers of them belong to the D_{3h} point group. As a result, they have 2D hexagonal Brillouin with the valence band maximum and conduction band minimum occurring at the corners, or K-points, of the Brillouin zone [38–40].

Importantly, in the monolayer limit, 2H TMDs have broken inversion symmetry, which was predicted to lead to valley-dependent optoelectronic properties for graphene with broken inversion

symmetry [41]. But the addition of strong spin-orbit coupling due to the heavy transition metal atoms also lead to large spin-splitting in the valence band with opposite signs at the +K and -K points in the Brilloiun zone for the 2H TMDs [40]. As a result, the +K and -K valleys experiment opposite circular polarization optical selection rules for interband transitions [10].

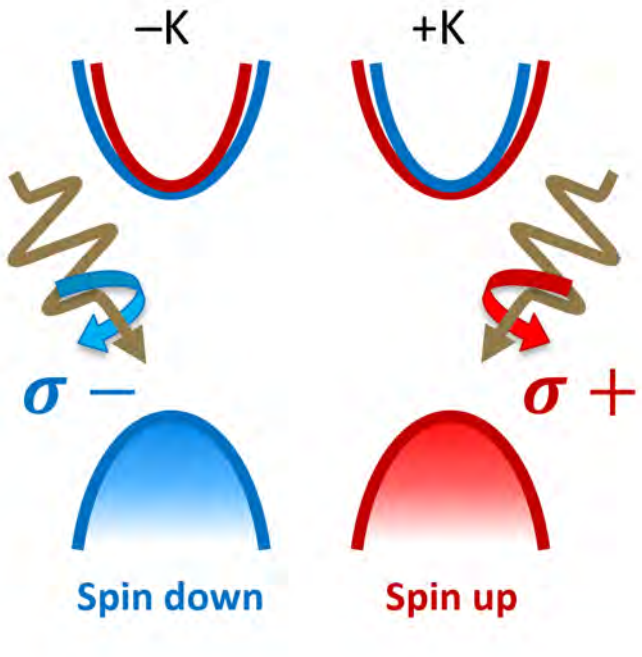

Figure 3.3: Band diagram illustrating spin-valley locking in the 2H phase TMDs. Red (blue) denotes a spin-up (-down) band. The lowest energy optically bright transitions in the +K (-K) valley couple only to $\sigma+$ ($\sigma-$) polarized light.

Figure 3.3 illustrates the main finding of [10], in which interband transitions in the +K (-K) valley couple exclusively to $\sigma+$ ($\sigma-$) polarized light. This can be understood by going back to Eq. (2.48), derived during the discussion of interband optical transitions in section 2.4. In [10], they replace $|v\rangle$ and $|c\rangle$ with the basis functions for the symmetry group of the band edges, C_{3h}, resulting in

$$|v\rangle = \frac{1}{\sqrt{2}}(|d_{x^2-y^2}\rangle + i\tau\,|d_{xy}\rangle) \tag{3.1}$$

$$|c\rangle = |d_{z^2}\rangle \tag{3.2}$$

where $\tau = \pm 1$ is the valley index. This allows them to evaluate the optical coupling strength $|P_x|^2$, which we had left un-evaluated. Specifically, they evaluate $|P_\pm|^2$, where $P_\pm = P_x \pm iP_y$ so as to calculate the coupling strength for $\sigma+$ (P_+) and $\sigma-$ (P_-) polarized light, which they find to be [10]

$$|P_\pm(\boldsymbol{k})|^2 = \frac{m_0^2 a^2 t^2}{\hbar^2}\left(1 \pm \tau \frac{\Delta'}{\sqrt{\Delta'^2 + 4a^2t^2k^2}}\right)^2 \tag{3.3}$$

where m_0 is the free electron mass, a is the lattice constant, t is the effective hopping integral, and $\Delta' = \Delta - \tau\widehat{s}_z\lambda$ is the spin-dependent band gap where Δ is the bare band gap, $\widehat{s}_z$ is the Pauli spin matrix, and 2λ is the valence band spin-splitting. The values for these are all obtained using a two-band $\boldsymbol{k}\cdot\boldsymbol{p}$ Hamiltonian of the form [10]

$$\mathscr{H}_0 = at(\tau k_x\widehat{\sigma}_x + k_y\widehat{\sigma}_y) + \frac{\Delta}{2}\widehat{\sigma}_z \tag{3.4}$$

where $\widehat{\sigma}$ are the Pauli matrices for the two basis functions given in Eqs. (3.1) and (3.2). The bands given by this symmetry-restricted Hamiltonian is then fit to a band structure produced via first-principle calculations and lead to the result that $\Delta' \gg atk$, allowing Eq. (3.3) to be simplified to [10]

$$|P_\pm(\boldsymbol{k})|^2 = \frac{m_0^2 a^2 t^2}{\hbar^2}(1 \pm \tau)^2 \tag{3.5}$$

As a result, in the +K valley where $\tau = +1$, $|P_+(\boldsymbol{k})|^2 \neq 0$ and $|P_-(\boldsymbol{k})|^2 = 0$, with the opposite true in the -K valley. Thus, to first order, interband transitions in the +K (-K) valley couple exclusively with $\sigma+$ ($\sigma-$) polarized light [10]. This spin-valley-polarization coupling was quickly experimentally confirmed by multiple groups within a year by exciting with a circularly polarized probe near resonance with the band gap and observing PL with a degree of circular polarization matching the polarization of their probe [11–13].

It was further shown that the valley-dependent optical selection rules are robust against magnetic fields up to fields as large as 7 T [42] owing to the large spin splitting and the suppression of spin-flip intervalley scattering by time-reversal symmetry [43].

In addition to the unique optical selection rules reviewed above, the spin-valley locking in the TMDs produces other effects as well [44, 45], such as the valley Hall effect, in which carriers of opposite spins accumulate on opposite sides of a sample perpendicular to the direction of current flow [46].

Much of the optical control and readout of the spin-valley physics relies on exciton formation and photoluminescence in the TMDs. As such, the next section will give an overview of excitons, trions, and many other species of excitons in the TMDs.

3.1.2 Excitons, trions, and more

Figure 3.4 shows perhaps the simplest of all gate dependent PL spectra across monolayer TMDs. Specifically, the doping dependent PL of an encapsulated monolayer $MoTe_2$ sample is shown.

In Fig. 3.4, we see that at neutral doping, there is a single strong PL peak corresponding to the emission energy of the neutral exciton. However, almost immediately upon doping free carriers into the system, the exciton PL is quenched and a new, lower energy peak appears. These lower energy peaks are charged excitons, or trions, which consist of an exciton

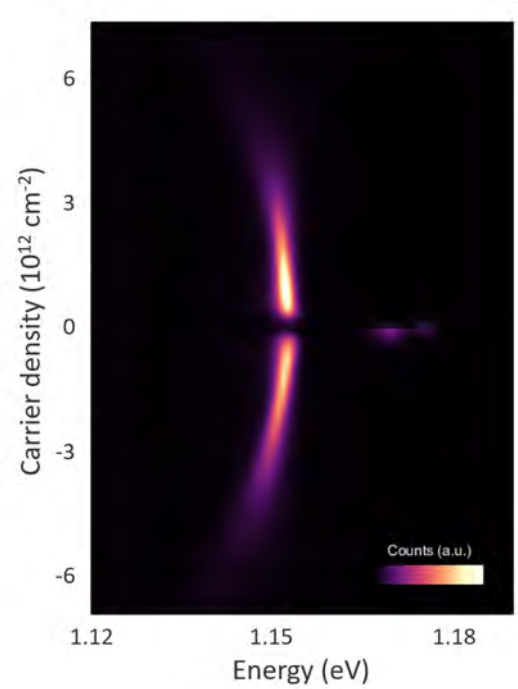

Figure 3.4: Carrier density dependent PL spectra for a monolayer $MoTe_2$ sample.

bound to a free carrier [47–49]. The additional
binding energy further reduces the energy of the three-body state, decreasing the emission energy should the trion dissociates through radiative recombination.

Figure 3.5 shows a band schematic of the trion formation. At the top of Fig. 3.5, we see the case where the system has been excited with a linearly polarized excitation laser, resulting in an equal population of excitons in the +K and -K valleys. In the bottom left, we see that upon doping holes into the system, trions form due to an exciton in one valley binding with a free hole in the opposite valley [50]. For simplicity, only the +K valley trion is shown, but under linear optical excitation its time-reversed partner in the -K valley will exist in equal populations. The same will be true for electron doping.

For electron doping, the bottom right panel of Fig. 3.5 illustrates the trion configuration in the +K valley. Due to nearly negligible spin-splitting in the conduction band, electrons with both spins are populated into both valleys, allowing the negatively charged trion to form with a free electron with opposite spin in the same valley as the exciton, while the intervalley exchange interaction causes the intervalley configuration to be higher in energy [50]. Like the neutral excitons, the trions maintain their valley polarization for a relatively long time, with scattering rates between the two species of negative trions being much greater than 25 ps due to the intervalley scattering of one of the two electrons being energetically unfavorable for the same reason that formation of the intervalley trion is energetically unfavorable [51]. Additionally, intervalley scattering in the valence band is strongly suppressed due to time-reversal symmetry [43].

While the intervalley scattering of excitons and trions is often suppressed, it is still possible and can be aided by K-point phonons in the material. Additionally, although the PL in monolayer $MoTe_2$ is relatively straightforward, there are many other possible species of trions and excitons that are optically dark, but can be brightened under certain situations.

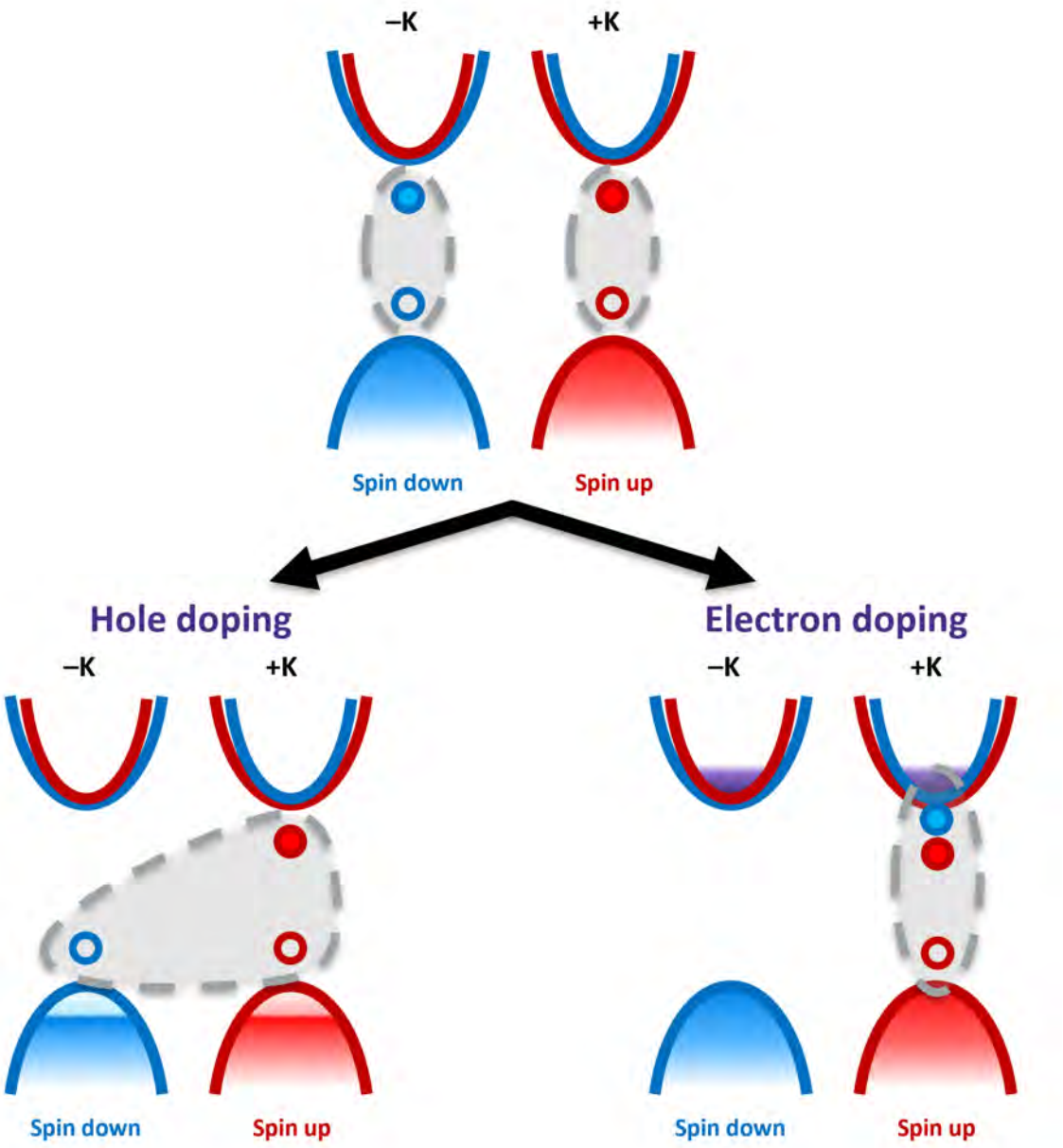

Figure 3.5: The top panel illustrates the case of exciton formation at neutral doping under a linearly polarized pump laser. In the bottom left, the case with moderate hole-doping is shown, where the exciton in one valley binds with a free hole in the opposite valley. In the bottom right, the case with moderate electron-doping is shown, where the exciton in one valley binds with a free electron of opposite spin in the same valley, owing to the negligible spin splitting in the conduction band. The bottom panels only show one species of trion, and under linearly polarized excitation it will only make up half of the trion population, where the other half will be it's time reversal partner.

The assignment of the trion configuration in Fig. 3.5 can by measuring the exciton/trion Landé g-factors. The Landé g-factor relates the Zeeman energy splitting between an exciton in the +K and -K valley via

$$\Delta E = E_{\sigma+} - E_{\sigma-} = g\mu_B B \tag{3.6}$$

where $E_{\sigma\pm}$ is the peak energy for $\sigma+$ and $\sigma-$ emission, g is the Landé g-factor, μ_B is the Bohr magneton, and B is the magnitude of the magnetic field. Based on Eq. (3.6), ΔE should increase linearly with field, allowing us to alternatively measure ΔE as a function of B and then use a linear fit to extract the slope of the dispersion, which will be

$$\frac{d(\Delta E)}{dB} = g\mu_B \tag{3.7}$$

We can use the Landé g-factor to understand what bands each constituent electron or hole comes from in an exciton or trion, as each band will have a g-factor specified by the orbital, valley, and spin contributions to the band's g-factor. A summary of theses different values is shown in [52] and reproduced for convenience in Fig. 3.6.

We will begin with finding the g-factor of the neutral bright exciton as an exercise. Figure 3.6 shows the spin, valley, and orbital contributions to the different bands in the +K valley. The right panel of the figure shows the contributions under a positive magnetic field, while the left panel shows the same under a negative magnetic field or, due to the +K and -K valleys being a time-reversal pair, the left panel shows the effect of a positive magnetic field on the -K valley. As such, we simply need to find the difference between the shifts for the spin-up valence band and spin-up conduction band for both the right and left panels. It is straightforward to see that $g_{X^0} = (g_{spin} + g_{valley}) - (g_{spin} + g_{valley} + g_{v,orbital}) = -g_{v,orbital}$.

From Eq. (3.1), we know that the valence band wavefunctions are made up of hybridized $d_{x^2-y^2} \pm$

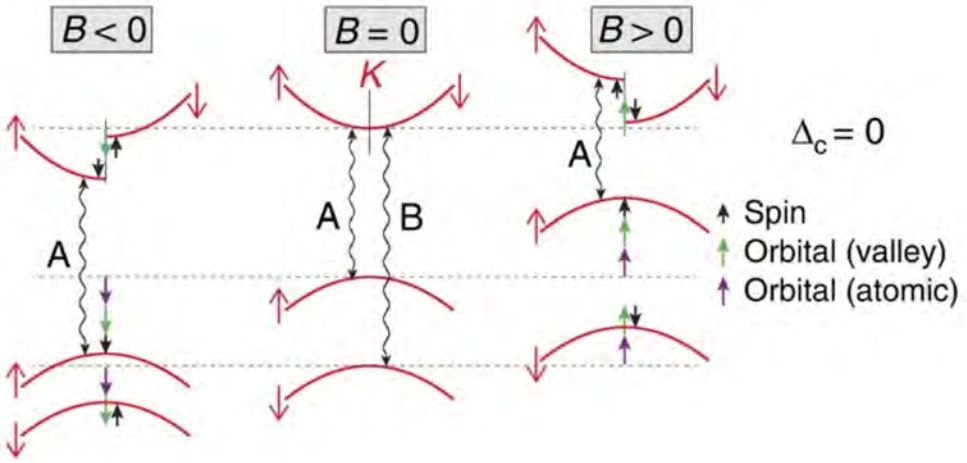

Figure 3.6: Illustration of the spin, valley, and orbital contributions to the g-factors of the conduction and valence bands in a monolayer TMD. Reproduced from [52].

id_{xy} orbitals [10] which have an orbital angular momentum of $l_z = \pm 2\hbar$, which implies that their contribution to the g-factor is $g_{v,orbital} = 4$. Thus, we can expect the neutral exciton to have an approximate Landé g-factor of $g_{X^0} \simeq -4$ [52]. And indeed, this is very nearly the value of the neutral exciton g-factor in numerous references [52–54].

Figure 3.7 shows a far richer doping dependent PL spectra taken in an encapsulated WSe_2 sample In addition to the excitons and trions shown in Fig. 3.5, which correspond to X^0, X^+, and X_s^-, the triplet, or intervalley, negative trion X_t^- is visible with the expected blueshift relative to X_s^-. Three momentum dark excitons/trions are also visible, D^0, D^-, and D^+, which are likely brightened via the use of a high numerical aperture (NA) objective and through phonon-assisted recombination, in which a K-point phonon scatters an electron from one valley to the other to allow it to radiatively recombine [53, 55]. The nature of these additional exciton and trion features was confirmed by extracting their Landé g-factor in a similar process to what was shown above [53].

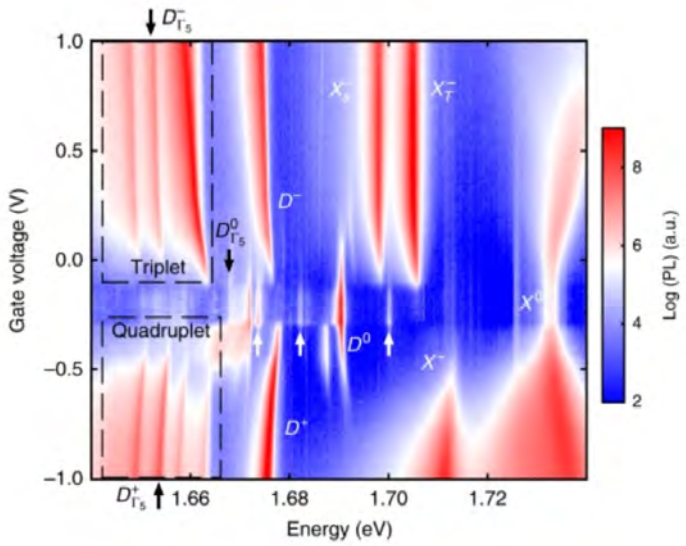

Figure 3.7: Gate dependent PL spectra in a monolayer WSe_2 sample. The bright excitons and trions correspond to X^0, X^+, and X_s^-. X_t^- is the triplet negative trion, and D_0, D^-, and D^+ are momentum dark excitons and trions. The boxed low energy features are phonon replicas of D^- and D^+. Reproduced from [53].

In addition, there are seven boxed low-energy peaks. These correspond to various phonon-assisted recombination pathways for the momentum or spin dark trions, in which either a K-point or Γ-point phonon is emitted by the electron or hole to induce an intervalley scattering or an intravalley spin-flip transition, thereby allowing the trion to radiatively recombine, where the energy emitted is the formation energy of the bare dark trion minus the energy of the phonon emitted in the scattering process [53, 56].

3.2 Non-moiré multilayers

One of the many advantages of 2D materials over bulk materials is the ability to stack layers of different 2D materials on top of each other to create devices with properties tailored to current research interests [57]. One of the simplest of such devices, but also one of the most useful for optical studies, is depicted in Fig. 3.8. This device is essentially a capacitor, in which top and bottom layers

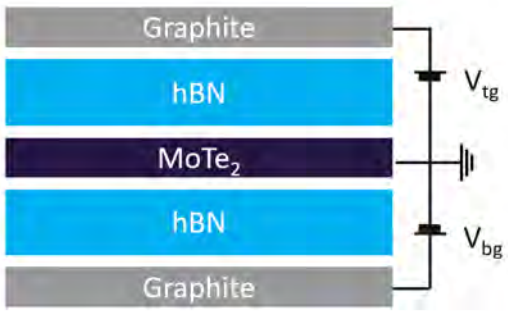

Figure 3.8: A simple dual-gated device.

of graphite act as gates separated from the sample, in this case monolayer $MoTe_2$, by a dielectric layer of hBN. By making the entire device out of 2D materials, the sample is sandwiched between atomically smooth faces and thus shielded from the extremely rough SiO_2 below [6].

The benefit of a dual-gated device like the one shown in Fig. 3.8 is that since the sample is grounded, by applying voltages to the top and bottom gates we can electrostatically tune both the carrier density inside of the sample and the out-of-plane electric field it experiences, where the carrier density and electric field are given by

$$n = \frac{\epsilon_{hBN}\epsilon_0}{e}\left(\frac{V_{top}}{d_{top}} + \frac{V_{bot}}{d_{bot}}\right) \tag{3.8}$$

$$D/\epsilon_0 = \frac{\epsilon_{hBN}}{2e}\left(\frac{V_{top}}{d_{top}} - \frac{V_{bot}}{d_{bot}}\right) \tag{3.9}$$

where $\epsilon_{hBN} \simeq 3$ is the relative permitivity of hBN, V_{top} (V_{bot}) is the voltage applied to the top (bottom) gate, and d_{top} (d_{bot}) is the thickness of the top (bottom) hBN dielectric layer.

Building devices as simple as that shown in Fig. 3.8 is all that is required to begin optically probing any 2D material or 2D material heterostructure. That being said, let's begin a brief overview of TMD heterostructures and the physics that can be explored within them.

3.2.1 Natural multilayers

The first TMD heterostructure we'll review isn't actually a TMD heterostructure. Rather, it's multilayer TMDs. While not a monolayer, natural TMD multilayers still retain some unique valley physics to explore. The main loss when moving from a monolayer TMD to a multilayer is the loss of the direct band gap. Bulk TMDs are indirect bandgap semiconductors, often with the valence band maximum at the Γ point in the center of the Brilloiun zone. As such, any TMD thicker than a monolayer suffers optically, namely the PL of the exciton becomes quenched as most the lowest

energy excitons in the system become momentum-indirect [58, 59].

This is illustrated nicely in Figure 1(a) of a 2010 paper from Professor Tony Heinz's group, which was one of the first to report on an optical study of a monolayer TMD [59]. The figure of note is reproduced here as Fig. 3.9 for the reader's convenience. Of note is the almost complete disappearance of PL from the exciton in the bilayer, indicating that indeed the direct bandgap of the monolayer is gone as soon as a second layer is added.

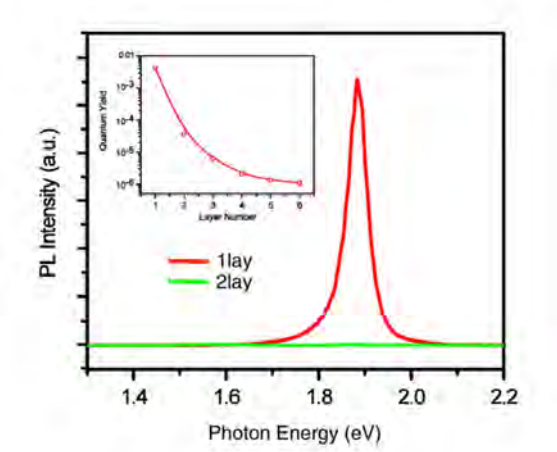

Figure 3.9: PL of monolayer and bilayer MoS_2. The inset shows the decreasing quantum yield of the PL as the number of MoS_2 layers increase. Reproduced from [59].

Despite the dramatic drop in PL, bilayer TMDs brought something unique to the table: layer psuedospin. For example, in a natural bilayer of WSe_2, and any TMD, the top layer and bottom layer have their Brillouin zone rotated by 180° relative to each other. As a result, it was found that by applying an out-of-plane electric field, a splitting in exciton energies between the top and bottom layers could be induced, allowing for optically addressing the +K and -K valleys of one layer independent of the other layer [60]. This presented the first opportunity to investigate how the electronic physics of the material could be affected with a two psuedospin parameters: valley and layer.

The additional layers in a multilayer TMD also allowed for the formation of a interlayer excitons, in which the electron and hole wavefunctions are spatially separated on different layers. However, owing to the low quantum yield of the PL in multilayer TMDs, studies on interlayer excitons in natural multilayers that rely on PL are still limited [61].

Other probes have shown more promise. In TMD samples with three or more layers, every-other layer's Brilloiun zone line up in momentum space. This means that while interlayer excitons be-

tween adjacent layers are spin-forbidden, interlayer excitons with the next-nearest layer are not spin-forbidden. By using differential reflectance (dR/R) as a probe, strong exciton resonances can still be observed, along with their anti-crossings with hybridized interlayer excitons [62].

Yet another non-PL probe of natural TMD multilayers is quantum capacitance [63]. Using a dual-gate architecture similar to Fig. 3.8 and a large magnetic field of $B = 14.9T$ to create flat bands within the system, the population of inidividual Landau levels within each layer was shown to be selectively tunable with gating, opening up the potential for tunable correlated physics, including signatures of an exciton condensate.

3.2.2 Heterostructures

TMD heterostructures had early interest due to the potential for heterostructures with tunable band gaps [64] and atomically smooth semiconductor junctions with easily tailored band alignments. [65–67].

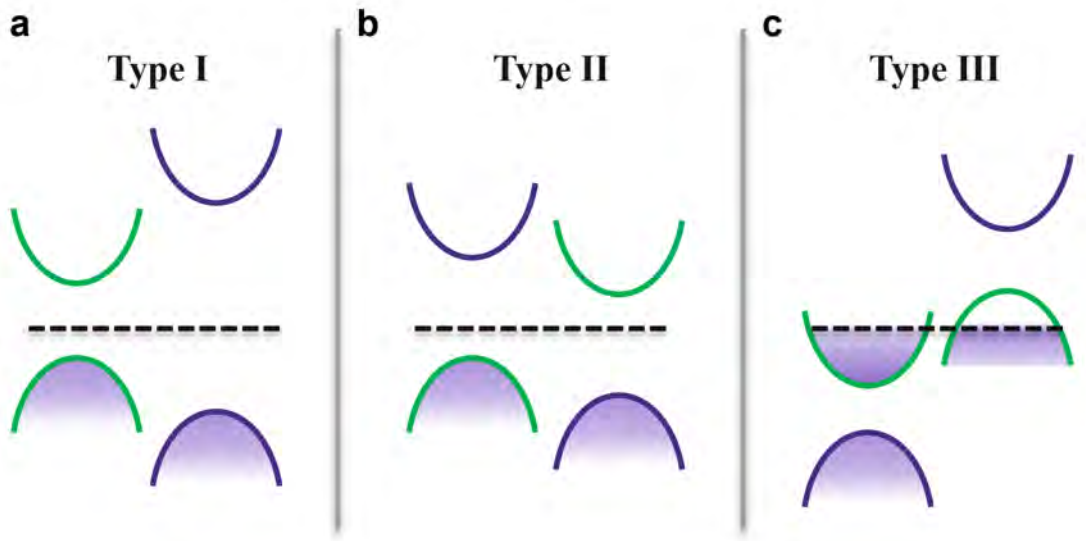

Figure 3.10: Illustrations of a) Type I, b) Type II, and c) Type III band alignments. Green denotes bands that are closest to the Fermi energy, denoted by a horizontal dashed line.

Figure 3.10 shows the three band alignments for two semiconductors coming into contact. Perhaps

the most common early TMD heterobilayer samples had Type II band alignment [68–70]. Type II TMD heterobilayers had the unique property of excited electrons and hole residing in different layers, and in fact different materials. This led to the formation of interlayer excitons with strongly suppressed radiative and nonradiative recombination pathways. As a result, interlayer exciton lifetimes in Type II heterostructures can exceed a few nanoseconds and sometimes reach 100s of nanoseconds [68, 71], long enough to be considered for use as a lasing medium [72] and far longer than the typical picoseconds or 10s of picoseconds lifetimes of intralayer excitons in monolayer TMDs [73–75].

Interlayer excitons in these Type II heterostructures often still retain their valley degree of freedom and have slow valley depolarization times due to the separation of the layers [71, 76]. However, what these misaligned heterostructures lack are correlated electronic phases. Conveniently, ever since the discovery of correlated electronic phases in twisted magic-angle bilayer graphene in 2018 [14, 15], moiré superlattices have proven to be an effective way to maintain the useful properties of multilayer devices while engineering the conditions for strongly correlated electronic phenomoena to occur.

3.3 Moiré effects

The observation of moiré patterns due to the interference of two similar atomic lattices which differ either by a small twist angle or a small lattice mismatch is nothing new. In fact, the observation of a moiré pattern in a material system has been reported as far back as the early 90s [9, 77]. In fact, Fig. 3.11a shows a reproduction of the graphene on graphite moiré pattern imaged in 1993 [9]. And even though the first experimental observation of strongly correlated physics in a moiré system wasn't until 2018 [14, 15], there were theoretical works on the potential for exotic correlated physics in moiré systems for several years already [8, 78–82], although the majority of papers were focused on moiré patterns in graphene-graphene or graphene-hBN systems.

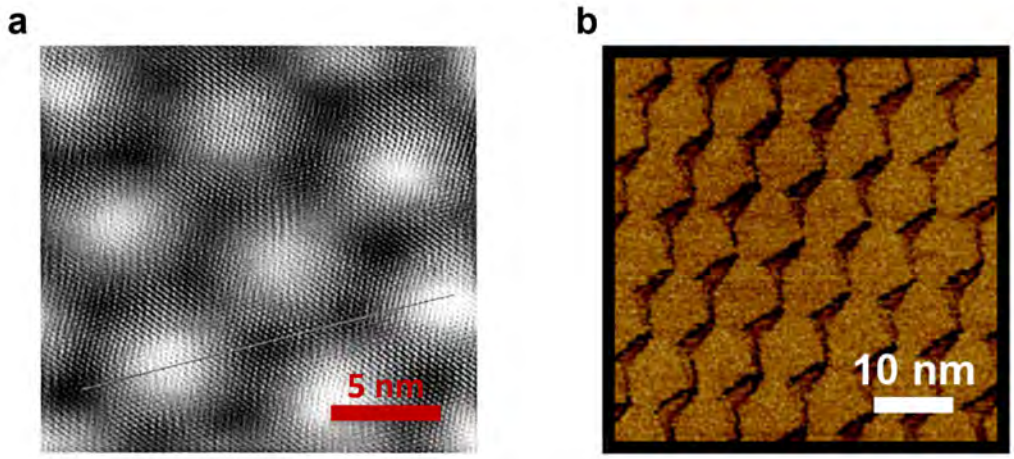

Figure 3.11: a) STM image of a moiré formed by the accidental rotation of the top layer of graphene on a graphite sample. Reproduced from [9]. b) PFM image of a moiré pattern formed by a WS_2/WSe_2 near 0° aligned heterobilayer.

However, TMD systems were not without attention either, with predictions of Hubbard model physics and strongly correlated electronic phases in TMD heterobilayer moiré s in 2018 [83] before the experimental realization of exactly that in 2020 [16, 17].

For a time, the focus in the world of TMDs was on heterobilayer moiré systems, like that shown in Fig. 3.11b, which is a piezo-force microscopy (PFM) [84] image of a WS_2/WSe_2 moiré superlattice during device fabrication.

TMD homobilayer moiré systems were still of interest theoretically, but the tendency for the valence band maximum to no longer occur at the K points often made them less appealing and more challenging to probe optically. Nevertheless, predicitions of topological insulators and other correlated electronic physics in TMD homobilayer moiré systems [18] maintained interest in the TMD homobilayers, the fruits of which will be discussed next.

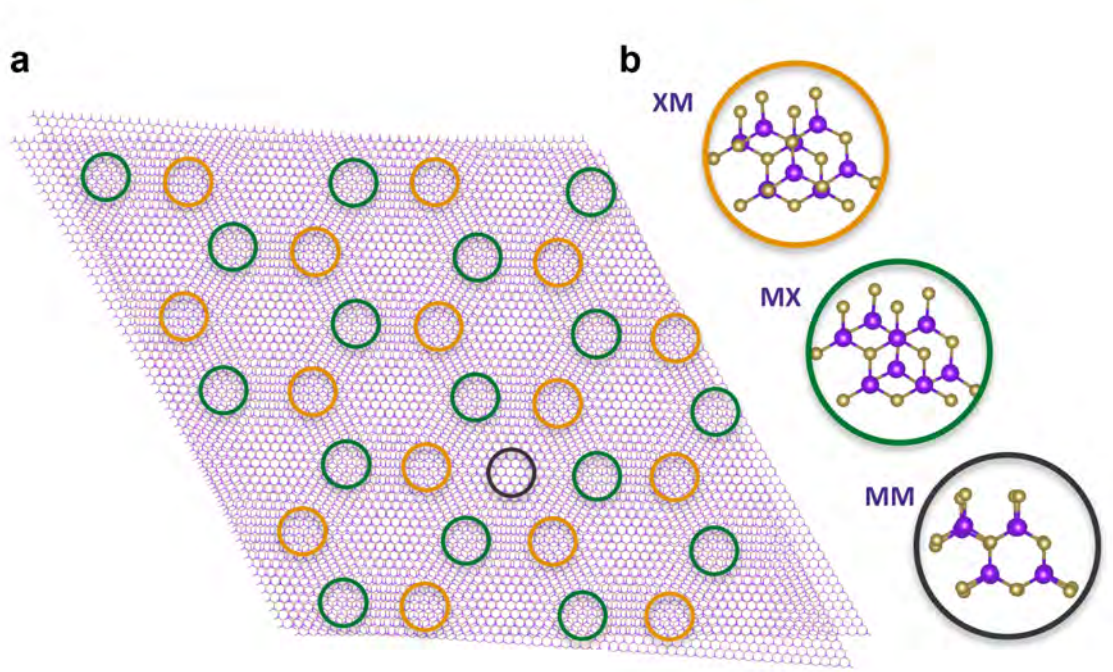

Figure 3.12: a) Moiré pattern created by stacking two identical monolayers of a 2H phase TMD on top of each other with a 4° twist angle relative to each other. The high symmetry sites are circled with orange (XM), green (MX), and black (MM) circles. The XM and MX high symmetry sites are the lowest energy sites in the moiré potential and form a honeycomb lattice [18]. b) Zoomed-in views of the 3 high symmetry points. Images made with VESTA 3 [28].

3.3.1 Homobilayer moirés

Figure 3.12 shows the moiré pattern formed by two layers of the same 2H phase TMD stacked with a twist angle of 4°. Of note is the fact that the XM and MX sites are related by a horizontal mirror plane. Thus, in the absence of anything to break the psuedo-mirror plane symmetry, the moiré potential must be degenerate at the MX and XM sites. It has been shown that the MX and XM sites are also potential minima for the moiré potential, with the MM site being a peak in the moiré potential, such that an effective honeycomb lattice is formed as a result of the moiré pattern [18, 85].

Furthermore, the symmetry relating the MX and XM sites means that carriers sitting at the MX and XM sites will have opposite layer psuedospins, as if carriers are in the top layer at the MX

site, then they must be in the bottom layer at the XM site, which will prove vital to much of the correlated electronic phenomena that has been observed in $tMoTe_2$ and other TMD homobilayer moiré systems.

To understand what might be able to arise due to the new honeycomb lattice and its layer psuedospin, we roughly follow the derivation and arguments made in [18]. First, we start in a similar place as when Eq. (3.4) was derived using a two-band model to describe the TMDs. Now, rather than be having the valence and conduction bands be the two bands used in the model, we consider just the +K valence bands in the top and the bottom layers. This leads to a two-band Hamiltonian of the form [18]

$$\mathscr{H}_{\uparrow}(\boldsymbol{d_0}) = \begin{pmatrix} -\frac{\hbar^2 k^2}{2m^*} + \Delta_b(\boldsymbol{d_0}) & \Delta_T(\boldsymbol{d_0}) \\ \Delta_T^{\dagger}(\boldsymbol{d_0}) & -\frac{\hbar^2 k^2}{2m^*} + \Delta_t(\boldsymbol{d_0}) \end{pmatrix} \tag{3.10}$$

where $\Delta_{b(t)}$ is the layer-dependent bias for top (bottom) layer and Δ_T plays the role of a complex hopping amplitude. Additionally, the layers are considered without a twist angle between them and instead $\boldsymbol{d_0}$ plays the role of the horizontal displacement between the two layers, allowing a psuedo-moiré to be constructed with an appropriate formulation of the dependence of the parameters on $\boldsymbol{d_0}$ to recreate the periodicity of the three high symmetry points.

Of particular interest is the role of the layer terms, which can be combined to form a layer psueodospin field given by [18]

$$\boldsymbol{\Delta}(\boldsymbol{r}) = (\Delta_x, \Delta_y, \Delta_z) = \left(Re\Delta_T^{\dagger}, Im\Delta_T^{\dagger}, \frac{\Delta_b - \Delta_t}{2} \right) \tag{3.11}$$

Due to the symmetry constraints of the expected moiré lattice, an equation for $\Delta_{t(b)}$ can be found by taking only the lowest order solutions that satisfy the symmetry requirements. Additionally, an equation for Δ_T can be found by considering symmetry requirements due to the d-orbitals that

make up the valence band states, leading to [18]

$$\Delta_l(\boldsymbol{d_0}) = 2V \sum_{j=1,3,5} \cos \boldsymbol{G_j} \cdot \boldsymbol{d_0} + l\psi \tag{3.12}$$

$$\Delta_T(\boldsymbol{d_0}) = w\left(1 + e^{-i\boldsymbol{G_2}\cdot\boldsymbol{d_0}} + e^{-i\boldsymbol{G_3}\cdot\boldsymbol{d_0}}\right) \tag{3.13}$$

where $l = +1(-1)$ for the bottom (top) layer, $\boldsymbol{G_j}$ is the jth rotation by 60° of one of the reciprocal lattice vectors, V and ψ characterize the moiré potential and can be fit to data from first principles calculations, and w is the tunneling strength, which must also be fit to data from first principles calculations. Doing this and incorporating the moiré band folding into Eq. (3.10) eventually allows the for the calculation of the spatial dependence of the layer psuedospin, which has been reproduced from [18] and is shown in Fig. 3.13.

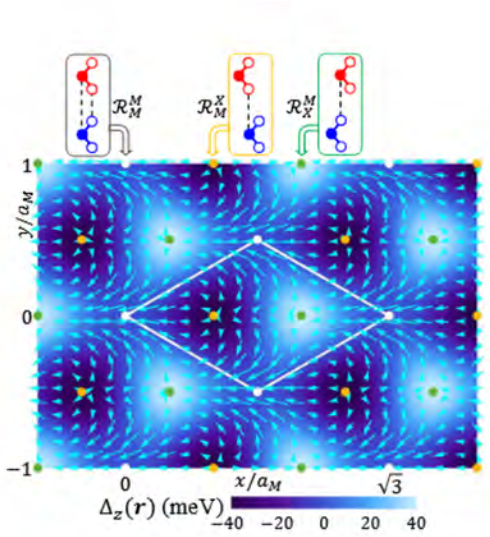

Figure 3.13: Spatial dependence of the layer psuedospin from Eq. (3.11). Reproduced from [18].

The layer psuedospin calculated by Wu et al. [18] and shown in Fig. 3.13 plays the role of an effective magnetic field for the two-band Hamiltonian from Eq. (3.10). Notably, the authors of [18] showed that the vortices and anti-vortices visible in Fig. 3.13 form what is effectively a real space skyrmion lattice for holes in the model, indicating the possibility of topological electronic bands [86].

At the end of their calculations, Wu et al. also verified that the two topmost valence bands for their model are topological by integrating Berry curvature over them [18], which emphasized the likelihood that twisted homobilayer TMD moiré systems could host exotic correlated electronic

phases. This was supported by later theoretical works as well [87, 88].

However, the model discussed above is only applicable if the valence band maximum is still at the K points, which it generally isn't for bilayer TMD systems. However, twisted $MoTe_2$ [18, 85] and twisted WSe_2 [88, 89] are exceptions, with their valence band maxima still occurring at the K points.

Eventually, the theoretical predictions of topology in $tMoTe_2$ came true, with the discovery first of ferromagnetic (FM) order in the material at a filling of $\nu = -1$ or 1 hole per moiré unit cell [85] before optical signatures [19] and transport signatures [20] of not just a topological Chern insulator phase, but of fractional Chern insulator phases, with multiple reports using different techniques supporting these claims [21, 22, 90].

3.3.2 Heterobilayer moirés

Figure 3.14 shows the moiré pattern formed by stacking two 2H TMDs, in this case WS_2 and WSe_2, on top of each other with no twist angle between the layers. Like the homobilayer case in Fig. 3.12, there are three high symmetry points. However, unlike the homobilayer case, the MX and XM sites are no longer related via a mirror symmetry due to the top and bottom layers being composed of different atoms. Thus rather than the formation of a honeycomb moiré lattice, a triangular lattice forms [28].

TMD heterobilayer moiré s were first studied as early as 2017, with some heterobilayer moiré systems being grown one layer on top of the other [91] and others being stacked [70] using the typical dry transfer technique [57].

The appearance of a triangular moiré lattice naturally led to modeling the system using the triangular Hubbard model [83], as it's phase space has been extensively explored [92] since it was first proposed by Hubbard [93]. Before long, the heterobilayer moiré system WS_2/WSe_2, which has Type II band alignment, was confirmed to be an experimental realization of the triangular Hubbard

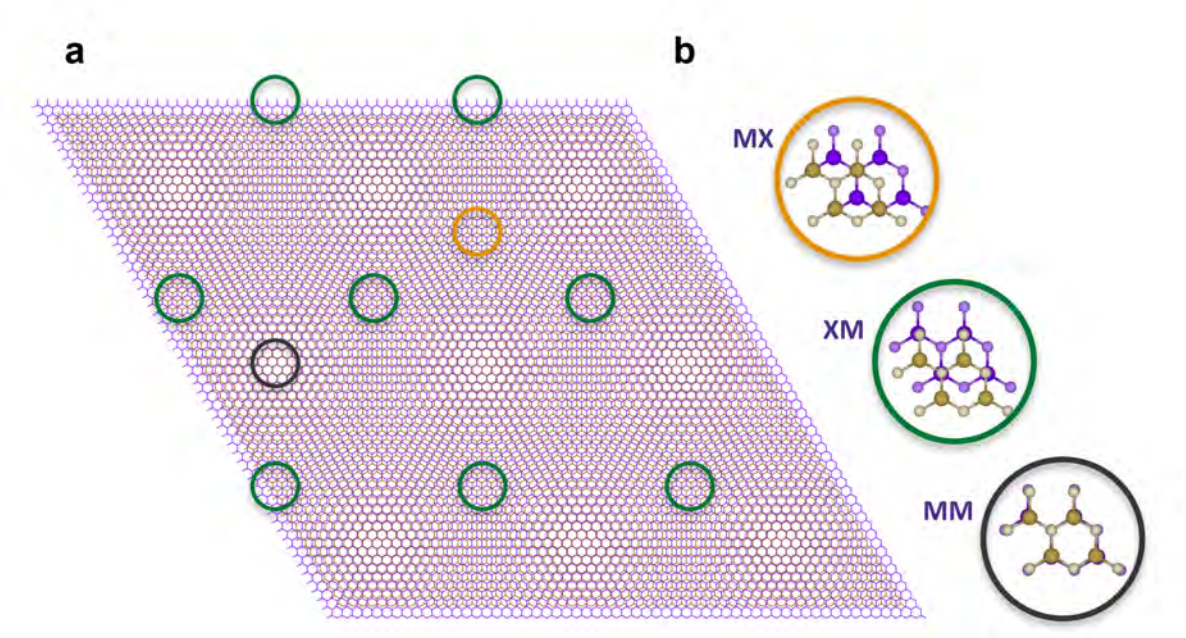

Figure 3.14: a) Moiré pattern created by stacking a monolayer of 2H-WS_2 on top of a monolayer of 2H-WSe_2 with a 0° twist angle between them The purple (gold) lattice is the WSe_2 (WS_2) layer. A moiré is created owing to the 5% lattice mismatch between the two layers. The high symmetry sites are circled with orange (MX), green (XM), and black (MM) circles. The XM and MX high symmetry sites are not degenerate in energy like in the homobilayer case, resulting in the formation of a triangular moiré lattice [83]. b) Zoomed-in views of the 3 high symmetry points. Images made with VESTA 3 [28].

model [16], with the discovery of generalized Wigner crystals at fractional fillings of the moiré lattice using an optical probe in addition to the Mott insulating state found at $\nu = -1$ [17]. This was further confirmed with microwave impedance microscopy [94] and STM imaging of the correlated electron lattice itself [95].

The unique optoelectronic properties of the TMDs were also exploited in attempts to optically manipulate the correlated states in WS_2/WSe_2 moiré systems. Ultimately, these efforts were successful in opticall-inducing ferromagnetism in a WS_2/WSe_2 moiré [96]. Specifically, the photo-excited excitons, which are Wannier-Mott like in the TMDs and thus free to diffuse through the material, mediated an effective long-range exchange interaction.

The long-lived interlayer excitons in these heterobilayer moiré systems also experience unique effects, such as being trapped by the moiré lattice for low interlayer exciton density before transitioning into a free interlayer exciton gas at higher densities in WSe_2/ mose moiré lattices [97].

In WS_2/WSe_2 moiré lattices, it has been shown that the interlayer excitons remain trapped by the moiré lattice to higher interlayer exciton densities. Instead of just forming a free interlayer exciton gas, interlayer excitons accumulate in the moiré potential traps, with the dipole-dipole interaction of interlayer excitons trapped in the same moiré site blue shifting them by discrete amounts depending on the number of interlayer excitons present [98].

It has also become reliable to use the doping dependent interlayer exciton PL as an indicator for correlated electronic order. For example, in WS_2/WSe_2 it was shown that the correlated electronic order reduced the nonradiative recombination rate and increased the interlayer exciton lifetime due to an effective attractive force between the correlated electrons and the interlayer excitons [99].

More recently the $MoTe_2$/ WSe_2 moiré system has also garnered interest due to correlated electronic phases discovered within it. Unlike the WS_2/WSe_2 system, $MoTe_2$/ WSe_2 has Type I band alignment, meaning that electrons and holes both localize in the $MoTe_2$ layer. As a result, the moiré lattice primarily affects charge carriers through the resulting in-plane strain from lattice relaxation

to maximize the size of the energetically favorable high symmetry stacking configurations [100, 101].

This system has been shown to be an integer Chern insulator under large out-of-plane electric fields, with the understanding being that band mixing between moiré bands in opposite layers leads to a topological phase transition [102]. Furthermore, under certain conditions a moiré Kondo lattice has been obtained in this system, the $MoTe_2$ layer is in a Mott insulating state while the WSe_2 layer hosts itenerant carriers that interact perturbatively with the magnetic order in the Mott insulating order. [103]

Overall, the 2H phase TMDs, especially when used to create moiré systems, have served as a fruitful platform for correlated electronic physics and optical interaction with these correlated phases. In the next few sections, I will discuss new work investigating the extent of optical interaction with correlated electron phases as well as introduce a new method for controlling the topological states in t$MoTe_2$.

Chapter 4

Anomalous Raman signatures of WS_2/WSe_2 moiré heterobilayers

Chapter 4 here.

4.1 Moiré induced Raman scattering modes in WS_2/WSe_2 heterobilayers

A comparison between the Raman spectra of monolayer WS_2, monolayer WSe_2, and a WS_2/WSe_2 moiré heterobilayer is shown in Fig. 4.1. The left panels show the full spectra while the right panels show a zoomed in portion of the low energy region, with the spectra for WS_2, WSe_2, and WS_2/WSe_2 shown in panels a-b, c-d, and d-f, respectively. Vertical red (blue) dashed lines indicate which Raman active modes in the WS_2/WSe_2 heterobilayer are inherited from the WSe_2 (WS_2) monolayer. As a guide to the eye, arrows point to peaks present in the WS_2/WSe_2 heterobilayer that are absent in either of the constituent monolayer spectra. The strong peak at 520 cm^{-1} comes from the silicon substrate [104] and is used to verify alignment of the experimental setup. It is important to note that all three spectra were taken from different spots on the same sample, as the WS_2 and WSe_2 monolayers did not have 100% overlap, so the sample had regions with only WS_2 or only WSe_2 in addition to the WS_2/WSe_2 region of the device.

In Fig. 4.1e, there are two new scattering modes of note that are absent in the constituent monolayer spectra. The peak at 318 cm^{-1} is the WSe_2 B^1_{2g} mode, which is Raman inactive in the monolayer

but become Raman active due to symmetry reductions in a heterobilayers [105].

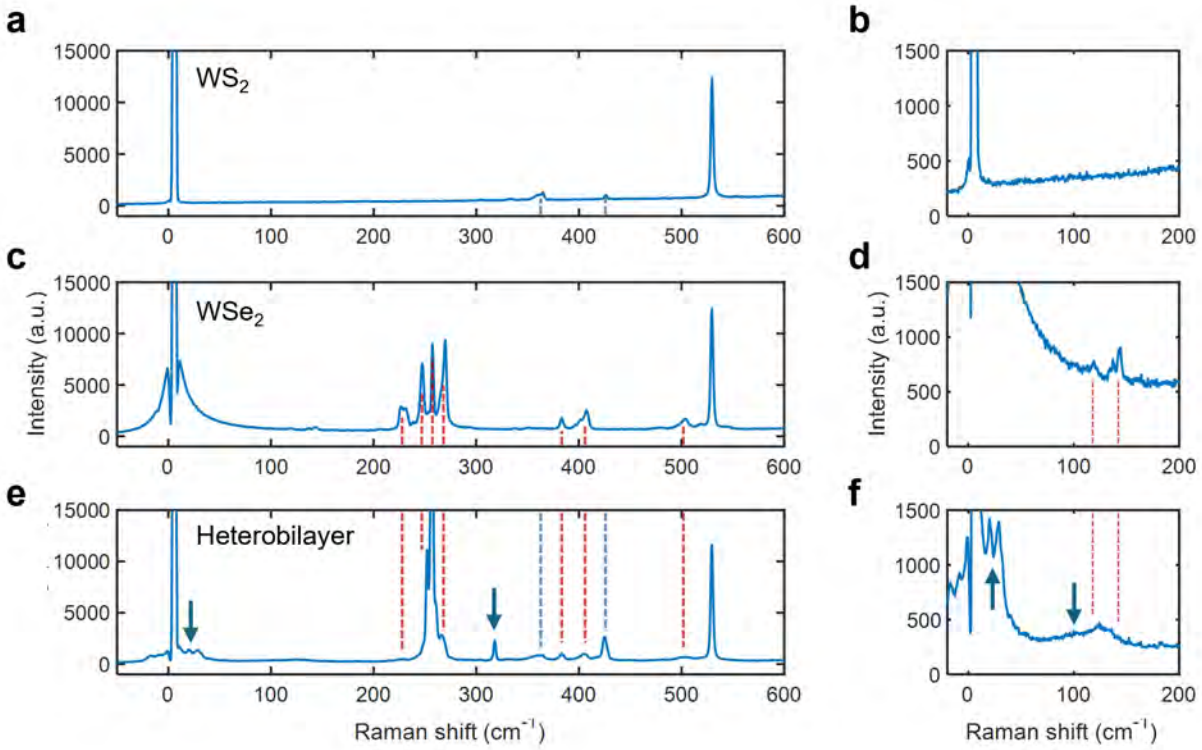

Figure 4.1: Data obtained from Device WW1. a) Raman spectrum from a monolayer WS_2 portion of the device. b) A zoom-in of the low-energy region of the WS_2 spectra. c) Full and d) low-energy Raman spectra from a monolayer WSe_2 portion of the device. e) Full and f) low-energy Raman spectra from a WS_2/WSe_2 moiré portion of the device. Blue (red) dotted lines indicate Raman peaks in the WS_2/WSe_2 spectrum that are also present in the monolayer WS_2 (WSe_2) Raman spectrum. Arrows in e) and f) indicate peaks only present in the heterostructure Raman spectrum.

The new low energy peak identified in Fig. 4.1e is more visible in panel f, and is identified as two peaks near the Rayleigh line with energies of 20 cm^{-1} and 29 cm^{-1}. These are likely the breathing and shear modes, which occur in both naturally grown bilayers [106] and artificially created heterobilayers [107]. For a two-layer sample like this, there should be one breathing and one shear mode, with their energies usually between 10 cm^{-1} and 50 cm^{-1} [106, 107], which is consistent with our observation here.

Figure 4.1f also reveals a weak feature near 100 cm^{-1}, which will be the focus of the remainder of this chapter. In this particular sample (WW1), the heterobilayer region was limited, so weak

features like the one at 100 cm^{-1} are difficult to distinguish from background. Figure 4.2 presents a much clearer picture.

Raman spectra from two different samples are shown in Fig. 4.2. The black curve is from an aligned WS_2/WSe_2 moiré heterobilayer sample (WW2), while the red curve is from an intentionally misaligned WS_2/WSe_2 heterobilayer sample (WW3). The inset shows piezoforce microscopy images [84] of the two samples during before the top hBN and gate were deposited. An FFT was performed for each to determine the moiré wavelength and twist angle between the WS_2 and WSe_2 layers. The aligned sample is determined to have a twist angle of 0.8°while the misaligned sample is determined to have a twist angle of 10.3°. As the strength of the moiré potential decreases drastically away from near 0° or near 60° alignment [108], the misaligned sample is expected to behave as two decoupled monolayers outside of charge transfer between the two layers due to their type II band alignment [70].

The purple shaded region in Fig. 4.2 highlights the main difference between the two Raman spectra. Firstly, the breathing modes previously discussed, while present in the aligned case, are nearly absent in the misaligned case. This is consistent with previous reports [109] and is evidence for the lack of structural coupling between the two layers. Additionally, the weak feature near 100 cm^{-1} previously shown in Fig. 4.1 is much clearer, likely due to the increased sample area and cleanliness of WW2 compared to WW1, and it is completely absent in the misaligned sample, indicating that this new mode is either absent in samples without a strong moiré potential or simply optically dark in such samples.

Unlike the lower energy moiré modes, the peak at 318 cm^{-1} identified as emerging due to the heterobilayer in Fig. 4.1 is present in both the algined and the misaligned sample in Fig. 4.2, albeit weaker in the misaligned case. This is potentially due to the fact that for the misaligned heterostructure, the layers only weakly couple, as evidenced by the loss of the shear and breathing modes [109]. Thus, the layers behave more independently and the symmetry responsible for darkening the B^1_{2g} mode is only weakly broken.

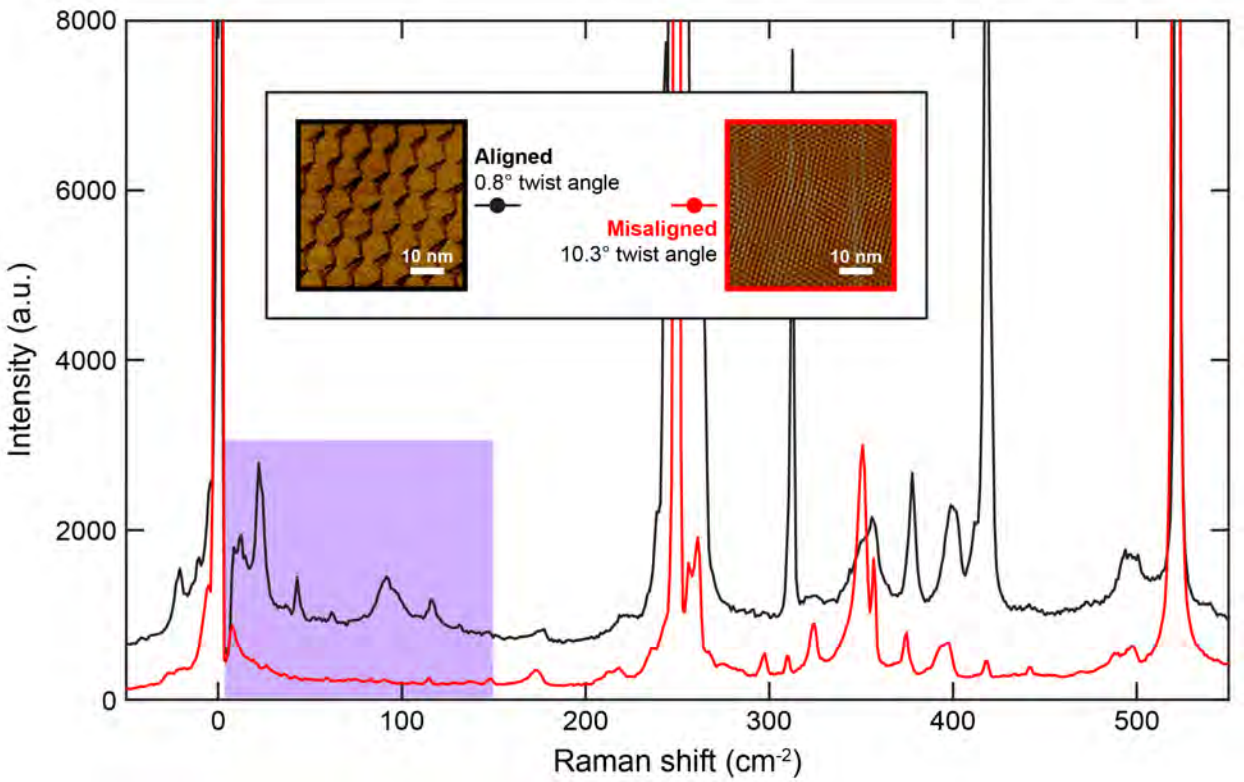

Figure 4.2: Raman spectra from an aligned (Devices WW2) and a misaligned (Device WW3) WS_2/WSe_2 heterostructure. The spectrum from the aligned (misaligned) heterostructure is shown in black (red). The inset shows piezo-force microscopy (PFM) images of the moiré patterns of the two heterostructures. The purple shaded region highlights the low energy peaks that are only present in the aligned heterostructure.

4.1.1 Determination of the Raman tensor

As discussed in **??**, polarization-resolved Raman spectroscopy allows us to determine the Raman tensor of the scattering mode. In non-resonant Raman spectroscopy, the form of the Raman tensor is solely determined by the symmetries of the excitation being probed. Figure 4.3 shows polarization-resolved Raman spectra for a WS_2/WSe_2 moiré sample, in this case sample WW2. Specifically, Fig. 4.3a shows scattering in the XX and XY channels, where the excitation is given an arbitrary linear polarization, and then the co-linearly polarized (XX) and cross-linearly polarized (XY) channels are collected. Figure 4.3b is similar to panel a, except the excitation is right-handed circularly polarized ($\sigma+$), and the co-circularly polarized ($\sigma+$ $\sigma+$) and cross-circularly polarized ($\sigma+$ $\sigma-$) channels are collected. With it, we can confirm many of the symmetry assignments of the modes

the heterobilayer has inherited from its constituent monolayers [110].

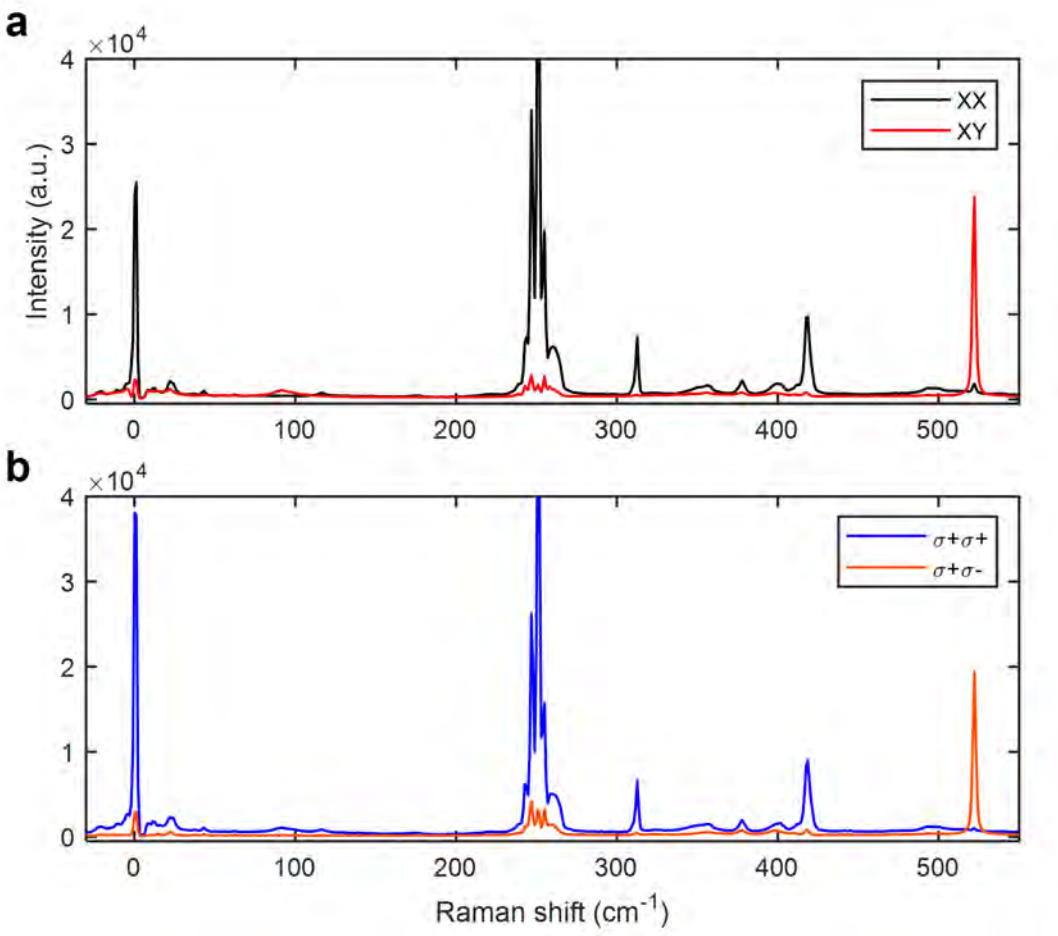

Figure 4.3: Polarization resolved Raman spectra from the moiré WS_2/WSe_2 heterostructure region of Device WW2. a) The Raman spectrum from the XX (XY) polarization channel is shown in black (red). b) The Raman spectrum from the $\sigma+\ \sigma+$ ($\sigma+\ \sigma-$) polarization channel is shown in blue (orange).

Figure 4.4 displays zoomed-in regions of Fig. 4.3. Panels a and c show the XX and XY channels, and panels b and d show the $\sigma+\ \sigma+$ and $\sigma+\ \sigma-$ channels. The $\sigma-\ \sigma-$ and $\sigma-\ \sigma+$ channels must be identical as time reversal symmetry is not broken in the sample.

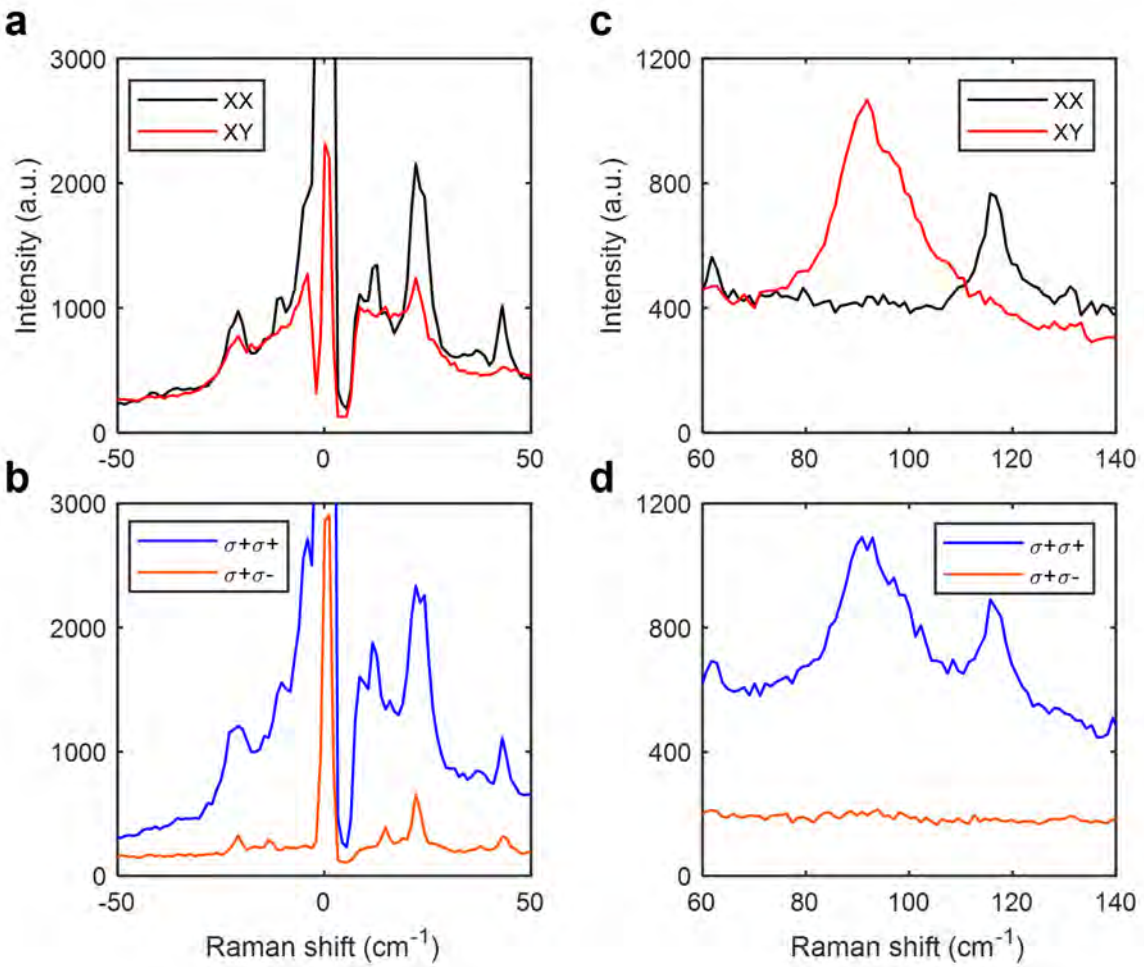

Figure 4.4: Low energy polarization resolved Raman spectra from the moiré WS_2/WSe_2 heterostructure region of Device WW2. a) The XX (black) and XY (red) polarization channels for the -50 cm^{-1} to 50 cm^{-1} region. b) the $\sigma+\ \sigma+$ (blue) and $\sigma+\ \sigma-$ (orange) polarization channels for the -50 cm^{-1} to 50 cm^{-1} region. c) and d) are the same as a) and b) but for the 60 cm^{-1} to 140 cm^{-1} region.

Of particular interest are the polarization selection rules for the unidentified mode at 90 cm^{-1}, which is bright in the XY and $\sigma+\ \sigma+$ channels and completely dark in the XX and $\sigma+\ \sigma-$ channels. As such, the only form of the Raman tensor that produces these selection rules is

$$R = \begin{pmatrix} 0 & a & \cdot \\ -a & 0 & \cdot \\ \cdot & \cdot & \cdot \end{pmatrix}$$

where the z-components of the tensor are unknown due to only probing in a backscattering geometry.

In the xy-plane, this Raman tensor is fully anti-symmetric. If we restrict ourselves to non-resonant Raman scattering, an anti-symmetric Raman tensor is forbidden in the absence of broken time reversal symmetry [111].

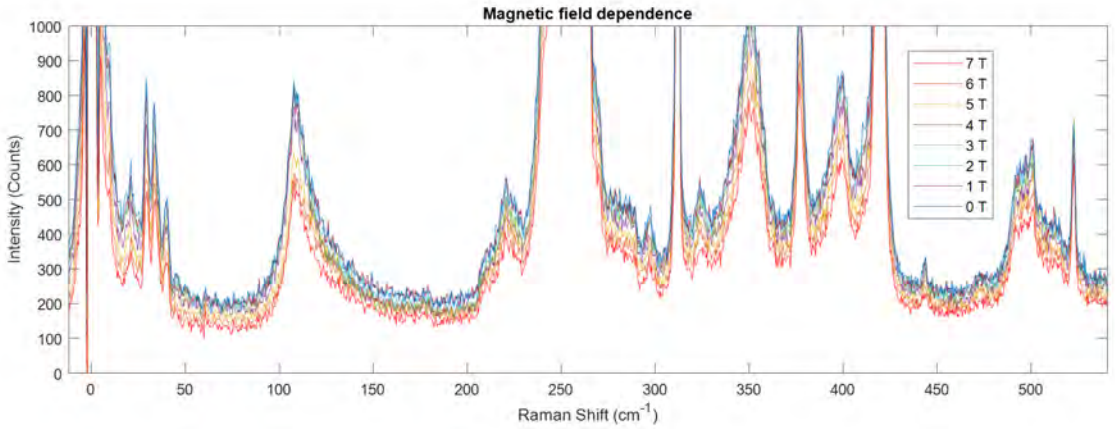

Figure 4.5: Magnetic field dependent Raman spectra from the moiré WS_2/WSe_2 heterostructure region of Device WW4. Notably, the moiré peak at 120 cm^{-1} shows no change with magnetic field relative to the known Raman peaks.

In order to check if the unidentified anti-symmetric mode is a magnon, we performed magneto-Raman measurements on the sample. The results are shown in Fig. 4.5 for device WW4. The $\sigma+$ $\sigma+$ channel is shown. Over a 7 Tesla range, the peak has no observable shift in energy or change in intensity relative to the phonon modes.

4.1.2 Influence of charge order on the moiré Raman mode

So far, all Raman measurements shown were at fixed doping and out-of-plane electric field. Figure 4.6 shows gate dependent photoluminescence in panel a and gate dependent Raman spectra in panel b. In this case, data from WW4 is shown, which only has a single gate and therefore does not allow for independent control of the electrostatic doping and applied out-of-plane electric field.

As described in section 3.3.2, the filling factor ν can be assigned using the intensity and energy shifts of the interlayer exciton. In doing so, we see that the unidentified Raman mode is bright only when the sample is in an insulating regime, either the trivial band insulator at $\nu = 0$ or the Mott insulating state at $\nu = 1$ [17]. This raises more questions than it answers.

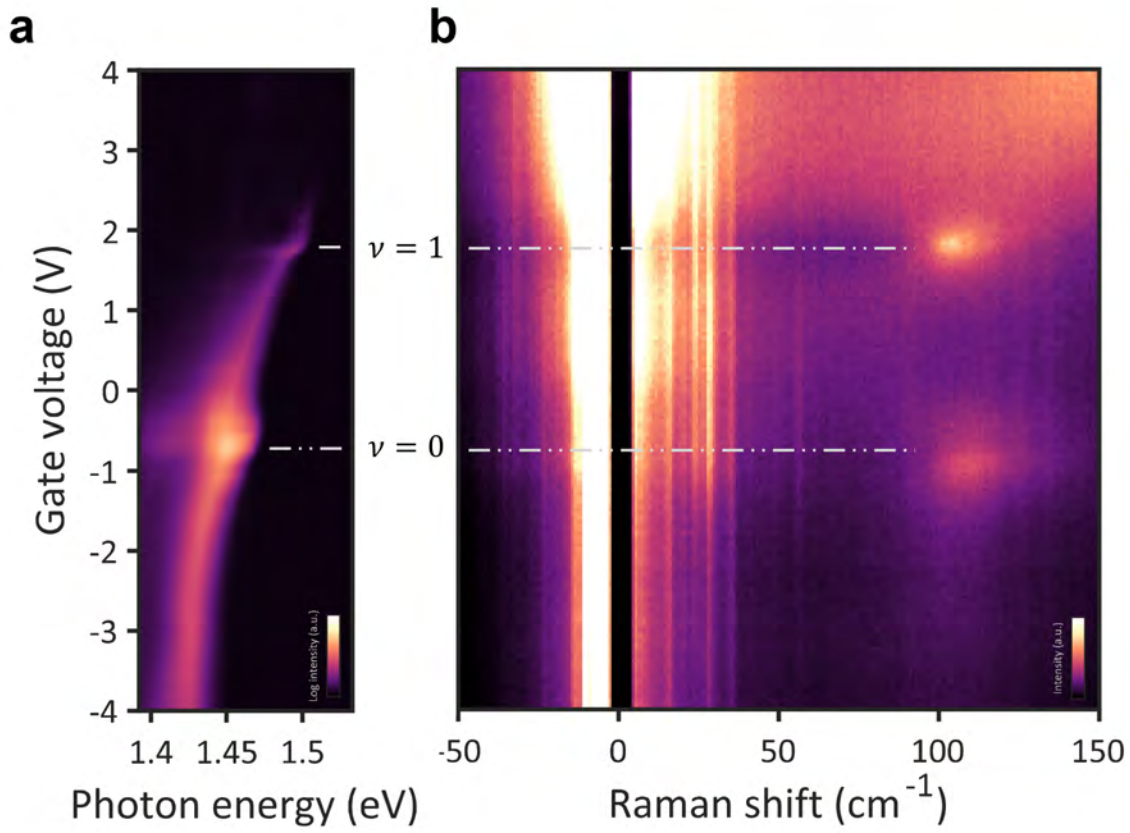

Figure 4.6: Gate dependent dependent a) PL and b) Raman spectra from the moiré WS_2/WSe_2 heterostructure region of Device WW4 is shown. Dashed lines denote the gate voltages that correspond to filling factors of $\nu = 1$ and $\nu = 0$ based off of the sample's twist angle and the features in the interlayer exciton PL.

A Raman mode that is so dependent on the sample's dielectric environment is unusual. In fact, to the author's knowledge no other Raman active excitation exhibits this kind of behavior, though the literature on the inelastic scattering of light in materials is vast.

The complexity of the unidentified Raman mode only increases in a dual-gated sample, where the carrier density and electric field can be independently tuned. Figure 4.7a shows Raman spectra taken in the XY channel from sample WW2. While the unidentified peak at 90 cm^{-1} does seem

brightest in the trivial band insulator regime, it is no longer completely dark in other regions of the phase space. Furthermore, a second peak near 120 cm^{-1} with the same selection rules appears at high hole doping.

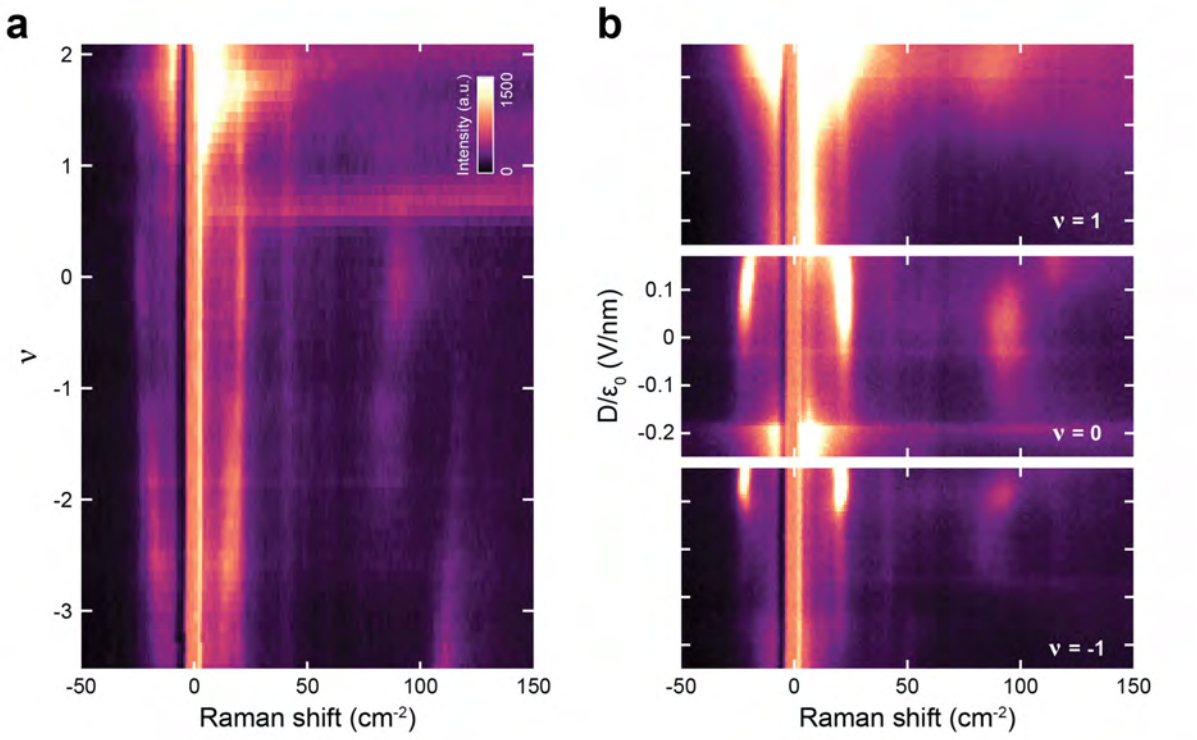

Figure 4.7: a) Filling factor and b) electric field dependence of the low energy WS_2/WSe_2 Raman modes in Device WW2. In b), the top, middle, and bottom panel have the doping fixed at $\nu = 1$, $\nu = 0$, and $\nu = -1$, respectively.

Figure 4.7b shows Raman spectra taken in the XY channel while the out-of-plane electric field is changed and the doping is kept constant at filling factors $\nu = 1$ (top), $\nu = 0$ (middle), and $\nu = -1$ (bottom). In this figure, the electric field is defined as positive when it is pointing from the WSe_2 layer towards the WS_2 layer, that is, a positive electric field is opposite the intrinsic bias from the Type II band alignment. In the top panel, we see that at $\nu = 1$ the 90 cm^{-1} mode appears only when the applied electric field is positive and thus opposite the sample's intrinsic bias. In the middle panel, we see that at neutral doping, the 90 cm^{-1} mode is present near zero applied electric field, the mode fades with negative applied field, and the 90 cm^{-1} mode is replaced by the 120 cm^{-1} mode at large positive applied field. In the bottom panel, we see that at $\nu = -1$ the behavior

of modes with applied electric field is similar to the case of neutral doping.

Now that a link has been established between the unidentified Raman modes at 90 and 120 cm^{-1}, we can explore their dependence on sample temperature. The left panel of Fig. 4.8 shows the temperature dependent Raman spectra for the 90 cm^{-1} mode at $\nu = 1$ and $D/\epsilon_0 = 0.2V/nm$, and the right panel shows the same for the 120 cm^{-1} mode at $\nu = 0$ and $D/\epsilon_0 = 0.2V/nm$.

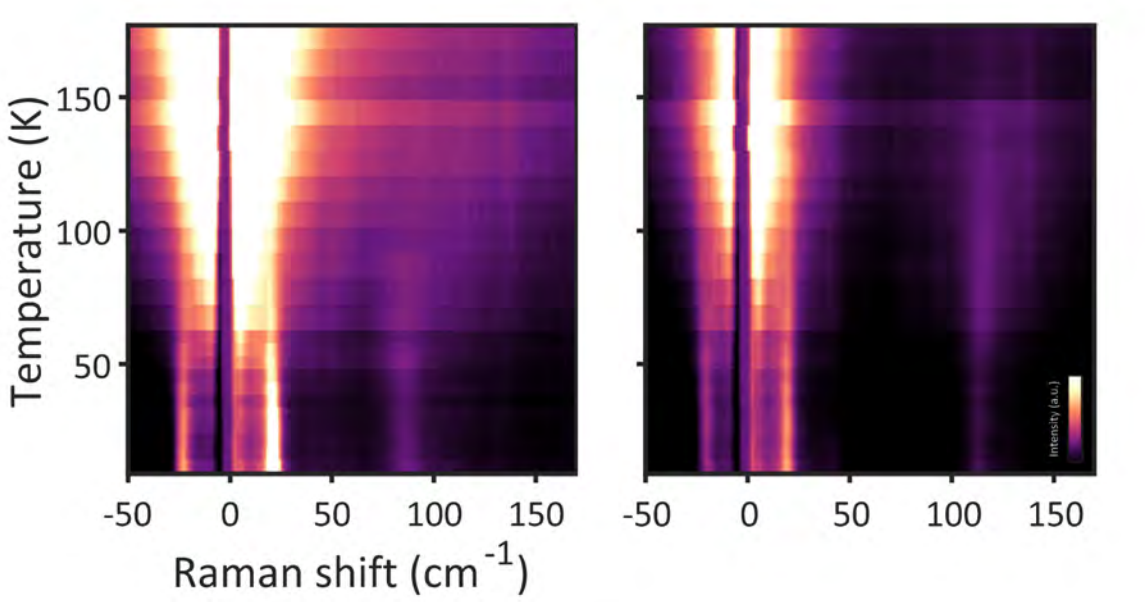

Figure 4.8: Temperature dependent Raman sepctra for the moiré WS_2/WSe_2 heterostructure region of Device WW2. The left panel shows the behavior of the 90 cm^{-1} moiré peak at $\nu = 2/3$ and $D = 0.2V/nm$. The right panel shows the behavior of the 120 cm^{-1} moiré peak at $\nu = 0$ and $D = 0.2V/nm$.

The 90 cm^{-1} and 120 cm^{-1} modes display similar behavior, broadening as temperature increases until their oscillator strength begins to decrease until they are no longer visible above 100 K for the left panel and 150 K for the right panel. The disappearance of the mode in the left panel, which has a doping of $\nu = 1$, coincides roughly with the melting of the Mott insulating state [17], again implying the importance of the dielectric environment. The right panel's higher temperature that the mode disappears at can understood as the result of the charge neutral band insulating state being much more robust, requiring larger temperatures to begin to introduce enough thermally activated charges into the sample to disrupt the dielectric environment.

4.2 The growing mystery of the unidentified WS_2/WSe_2 Raman modes

With no clear candidate explanation presenting itself given the data so far, it is time to face the elephant in the room: resonance. All data presented until now was taken with a 532 nm probe laser, in which each photon's 2.33 eV worth of energy exceeds the lowest energy excitations of both constituent monolayers and is certainly in resonance with something. Up until now, data has been viewed through the naive lens of non-resonant inelastic scattering presented in **??**. And while this is fine for many Raman features, indeed most phonon modes in the earlier spectra behave as they would for non-resonant scattering save for some changes in relative intensity, for an unidentified mode that is clearly coupled to the dielectric environment, resonance most certainly plays a role.

The easiest first check is to see if there are any noteworthy resonances in WS_2 or WSe_2 near 2.33 eV. We find that indeed, our probe laser is weakly resonant with the WS_2 B exciton [112] and the WSe_2 gamma point band-nesting energy [113]. Since signal for a below-bandgap excitation would likely be too weak to perform Raman spectroscopy, we can instead change our excitation source and target a different resonance to see if it brings new information to the table.

4.2.1 Resonant Raman as a probe of excitonic coupling to the mode

In order to investigate the dependence of the moiré Raman modes on the energy of the probe laser, we employ a tunable, narrow linewidth light-source (MSqaured SolsTiS) and a triple-grating Czerny-Turner spectrometer (Teledyne Princeton TriVista), to perform resonant Raman spectroscopy. Figure 4.9 shows gate dependent Raman spectra taken on sample WW4 with an excitation wavelength of 726 nm, which is resonant with the WSe_2 A exciton [114].

With 726 nm excitation, the WSe_2 phonon modes near 250 cm^{-1} are all strongly enhanced, showing up brighter than the broad photoluminescence and quasi-elastic tail in the background. The higher

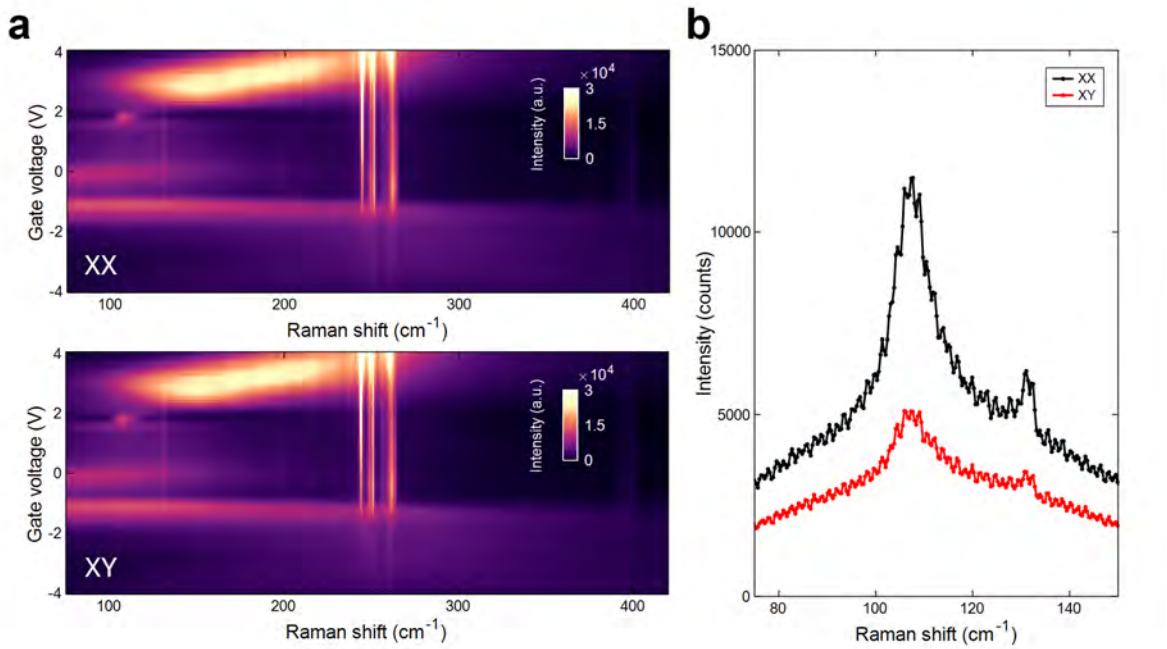

Figure 4.9: a) Gate dependent Raman spectra from Device WW4 with a 300 μW 726 nm probe. The top (bottom) panel of a) shows data from the XX (XY) polarization channel. b) A line cut of the moiré peak at a gate voltage of 1.9 V.

energy WS_2 phonon modes near 400 cm^{-1} do not see a similar enhancement, due to the confinement of the WSe_2 A exciton to its own layer. Interestingly, the unidentified mode at 120 cm^{-1} only appears near $\nu = 1$, whereas in Fig. 4.6b it appears at $\nu = 1$ and $\nu = 0$. The largest change with the change in excitation wavelength is the polarization selection rules of the moiré mode. Under 532 nm excitation, the mode is absent in the XX channel, but for 726 nm excitation it is now brighter in the XX channel than the XY channel.

Such a change in polarization selection rules, and thus the Raman tensor, often occur when a strong resonance condition is met. While in non-resonant Raman the scattering process is mediated by a virtual electronic state, for resonant Raman the photon excites an electron to a real state, and then the electron scatters and excites the observed mode before decaying back to the ground state, emitting a photon [115]. As a result, the symmetry selection rules of the real electronic state become important and can often outweigh the selection rules of the observed excitation. For example, in MoS_2, when the excitation is resonant with exciton, the coupling between the incident photons

and the E' phonon mode becomes primarily mediated by the exciton's coupling with the phonon through the Fröhlich interaction, resulting in the polarization selection rules changing to match those of the exciton instead of the phonon [116].

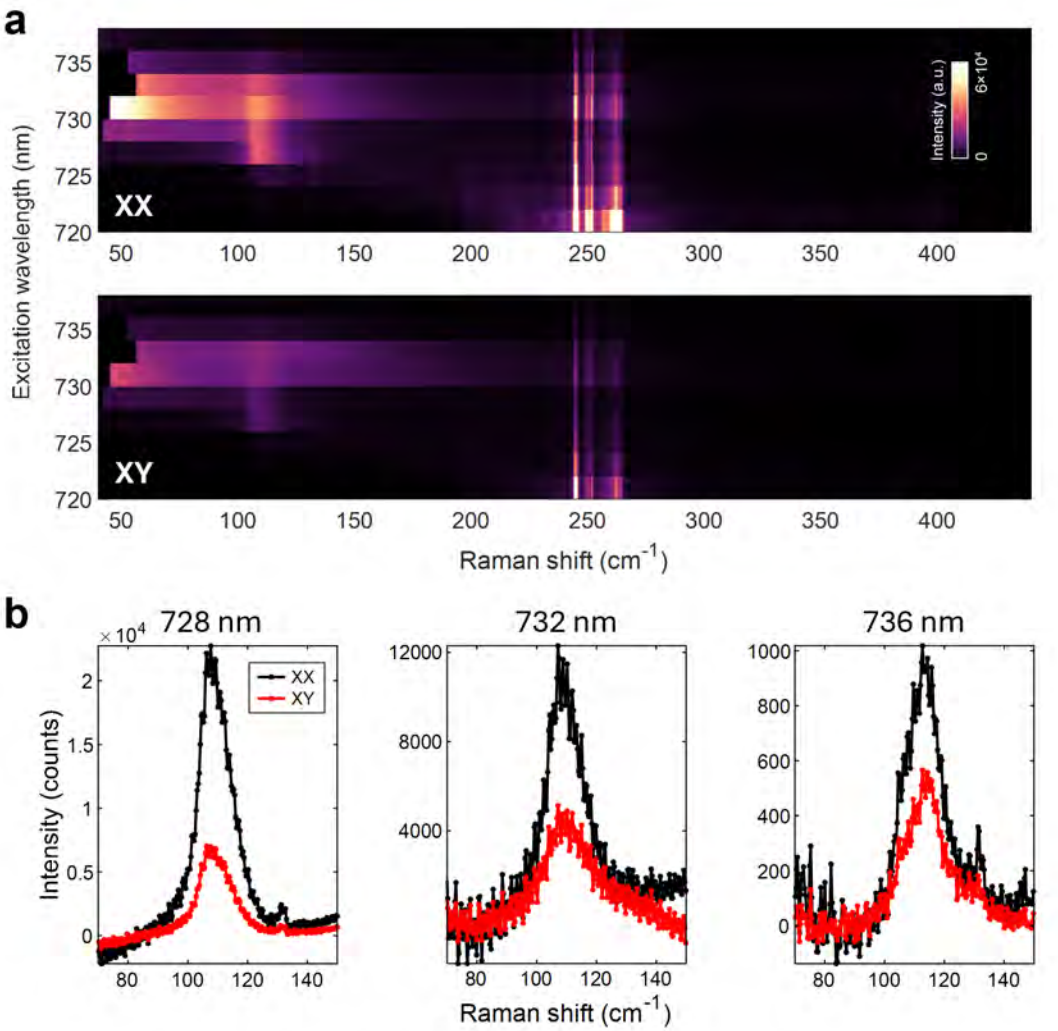

Figure 4.10: a) Excitation dependent Raman spectra from Device WW4 taken with a 300 μW probe with the gate voltage held at 1.9 V. The top (bottom) panel in a) shows the XX (XY) polarization channel. b) Raman spectra showing just the region with the moiré peak taken with an probe wavelength of 728 nm, 732 nm, and 736 nm for the left, middle, and right panels, respectively.

Figure 4.10a further illustrates the importance of the excitation wavelength matching a resonance condition, as it can be clearly seen that only over a narrow range of wavelengths (10 nm) is the resonance strong enough to see the large enhancement of the moiré mode. Figure 4.10b shows

linecuts at select excitation wavelengths after a linear background has been removed to account for the roughly linear tail of the WSe_2 exciton PL. As the excitation wavelength increases away from the optimal resonance condition, not only does the intensity of the moiré Raman mode decrease, but the ratio between the signal in the XX and XY channels also decreases. This suggests that as the excitation continues to increase until it is no longer resonant, the moiré Raman peak may once again be cross-linear polarized similarly to under 532 nm excitation.

4.2.2 Nonlinear power scaling

The final oddity of the moiré mode to be presented here is it's power dependence. Figure 4.11 shows the dependence of the WS_2/WSe_2 Raman spectrum on laser power for sample WW2 with 532 nm excitation (a and b) and for sample WW4 with 730 nm excitation (c and d). It is important to note that the colorscale corresponds to intensity recorded by the spectrometer divided by the excitation power. This is because typically in a scattering experiment, the scattered power (or intensity) is proportional to the incident power according to Feynman's golden rule. As such, if the intensity normalized by excitation power remains constant regardless of excitation power, then this condition is filled. It is evident from Fig. 4.11a and c that all of the phonon modes inherited from the WSe_2 and WS_2 monolayers indeed have a constant ratio between their scattered intensity and the excitation intensity. This is further confirmed in Fig. 4.11b and d, where the red dots are the integrated intensity of the phonon modes plotted with respect to the laser power, and the red dashed line is a power law fit to them giving scaling of very nearly unity, i.e. $I_{phonon} \propto I_{laser}$.

On the other hand, the moiré mode for both samples and excitation wavelengths exhibits a clear nonlinear relationship between the excitation power and integrated intensity. In Fig. 4.11b and d the moiré mode integrated intensity is plotted in blue, with a power law fit giving $I_{\text{moiré}} \propto I_{laser}^{1.58}$ and $I_{\text{moiré}} \propto I_{laser}^{1.45}$ for panel b and d, respectively.

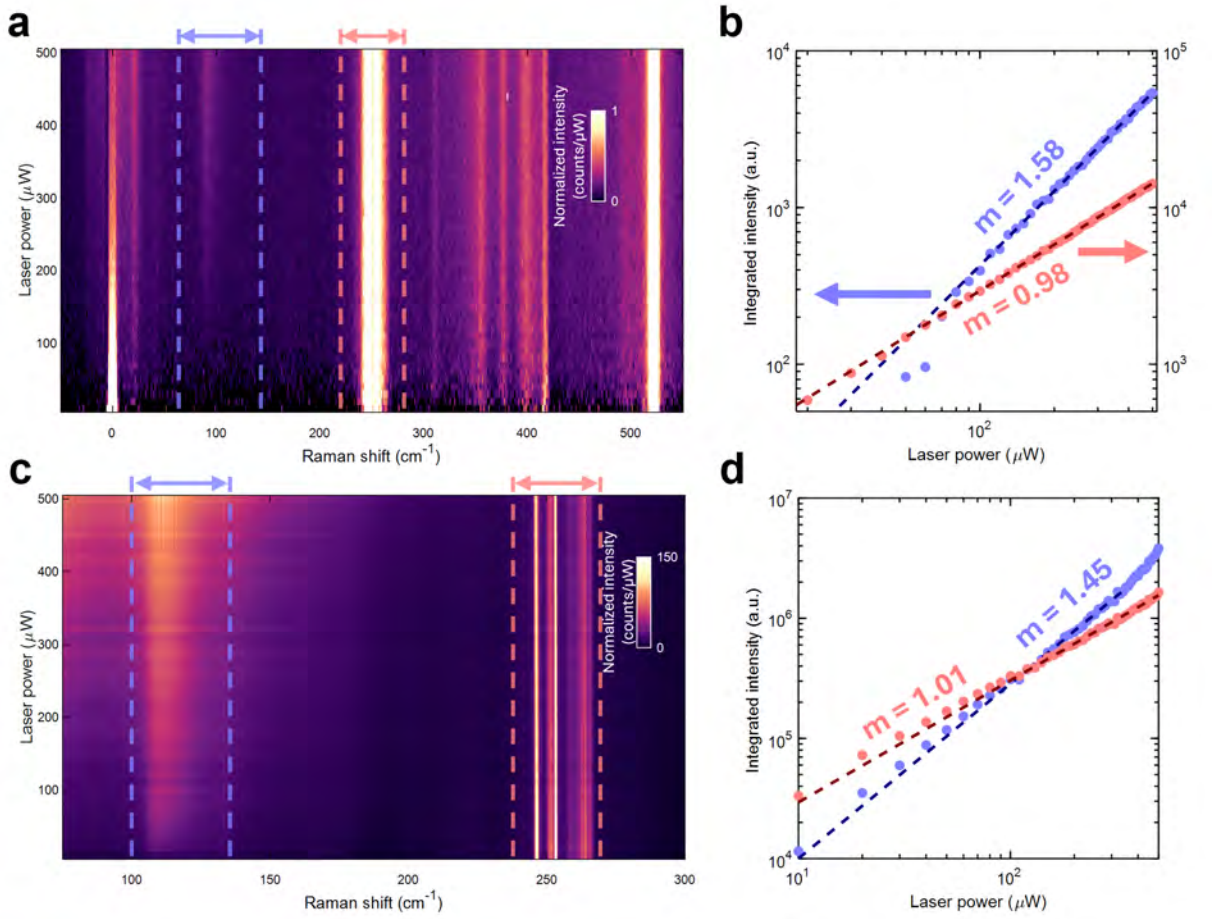

Figure 4.11: a) Power dependent Raman spectra for Device WW2 taken with a 532 nm probe. The color scale is in units of counts per μW, such that if a peak's color is unchanging with laser power then it scales linearly with power. b) A power law fit on a log-log scale for the moiré peak (phonon peaks) is shown in blue (red). The dots are integrated intensity over the regions indicated by the blue and red arrows in a), while the dashed lines are the power law fits. c) and d) are the same as a) and b) but for Device WW4 taken with a 730 nm probe.

4.3 Candidate explanations and future studies

The combination of the unique power scaling of the moiré Raman peak, its enhancement when resonant with WSe_2 excitons, and its dependence on the sample dielectric environment present a unique puzzle even before including the anti-symmetric Raman tensor for excitation under 532 nm. One candidate explanation for the mystery mode is that of the WSe_2 K-point phonons. While traditionally only excitations with a crystal momentum of zero are optically active [115], a more complex scattering process involving exciton scattering could provide the necessary momentum to

create a K-point phonon. Since the the acoustic phonons in WSe_2 have a similar energy at the K-point [53] to the modes observed in this section. The nonlinear power dependence and dependence on the dielectric environment point to the scattering process requiring an existing population of excitons or interlayer-excitons present in the system, which would be provided by a combination of a high power excitation beam and an increased interlayer exciton lifetime at insulating states [71]. However, this candidate explanation doesn't have a clear path towards explaining the anti-symmetric Raman tensor of the mode or the existence of two distinct peaks that don't seem to co-exist in the phase space.

Chapter 5

Optical probes of correlated states in twisted $MoTe_2$

Figure 3.12a shows the moiré pattern formed from two monolayers of $MoTe_2$ stacked on top of each other near AA stacking with a small twist angle (generally between 2° and 5°). Of the three high symmetry points, the MX and XM sites, also labeled as B and C in the diagram, often play the most important role. As seen in **??**b, these two high symmetry points are mirror images of them. As a result, until the horizontal mirror symmetry is explicitly broken on the scale of the sample, the two sites must be energetically degenerate. This allows for easy tuning between a honeycomb and triangular lattice using an out-of-plane electric field to lift their degeneracy.

While any 2H-phase transition metal dichalcogenides will share this moiré structure when stacked near AA-stacking, $tMoTe_2$ has a distinct advantage of still having the valance band maximum and conduction band minimums occur at the K-point [18]. Thus, the strong spin-valley locking of the monolayer TMDs remains, but now with the addition of a moiré potential. Furthermore, this means that unlike other homobilayer (natural or moiré) TMDs, $tMoTe_2$ retains its direct band gap, giving easy access to the underlying physics through the use of optical probes. This is illustrated in Fig. 5.1, where the PL spectrum for $tMoTe_2$ (panel b) has the same characteristics as that of monolayer $MoTe_2$ (panel a), save for an overall red shift of the features and the addition of new doping dependent features.

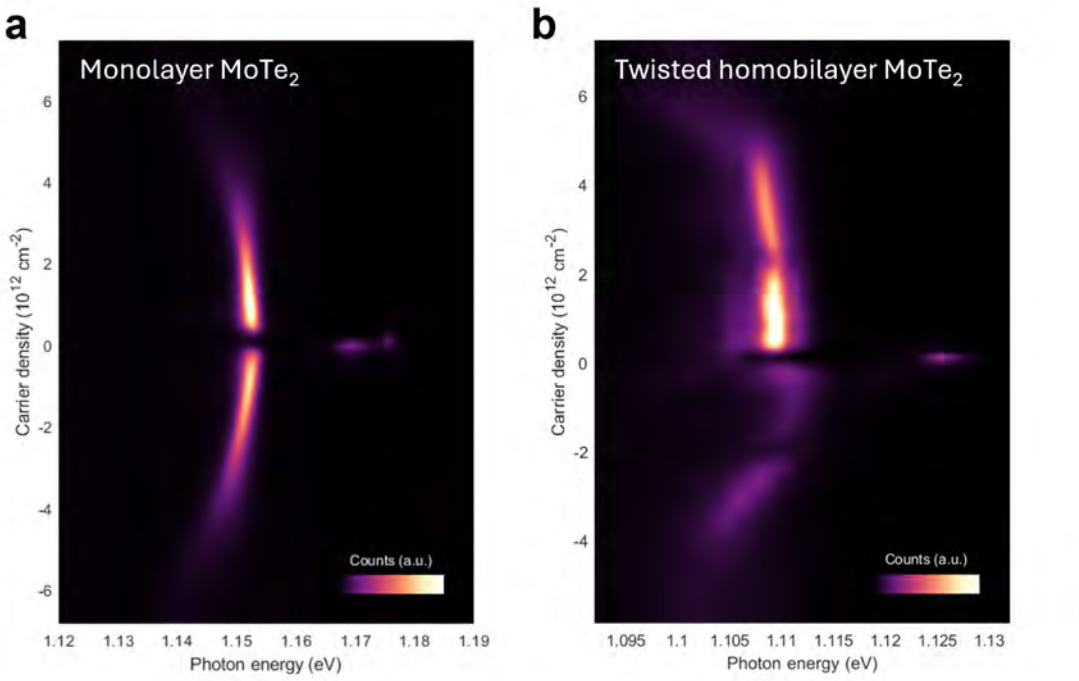

Figure 5.1: Doping dependent PL from a a) monolayer $MoTe_2$ sample and from a b) homobilayer moiré $MoTe_2$ sample.

5.1 Gapped state detection via photoluminescence

One of the simplest optical probes of charge order in moiré TMD devices is the intensity of the trion. As discussed in section 3.1.2, trions are formed by an exciton forming a bound state with a free carrier in the sample. Since trions are lower energy bound states than their excitonic precursors, they dominate the PL spectrum upon doping the sample away from charge neutrality, as can be seen in Fig. 5.1 and Fig. 5.2a. As such, the trion intensity becomes a proxy for the presence of free carriers in the sample.

When the Fermi energy of the sample intersects a gap in energy states, whether it be a trivial band gap or correlated insulating state, the number of free carriers is suppressed so long as the electronic temperature of the sample is sufficiently small as to not thermally excite a large population of carriers across the gap. With this significant reduction in the number of free charges, trion formation is slowed, leading to a reduction in trion intensity like what is seen at $\nu = 1$ in Fig. 5.2a. The differ-

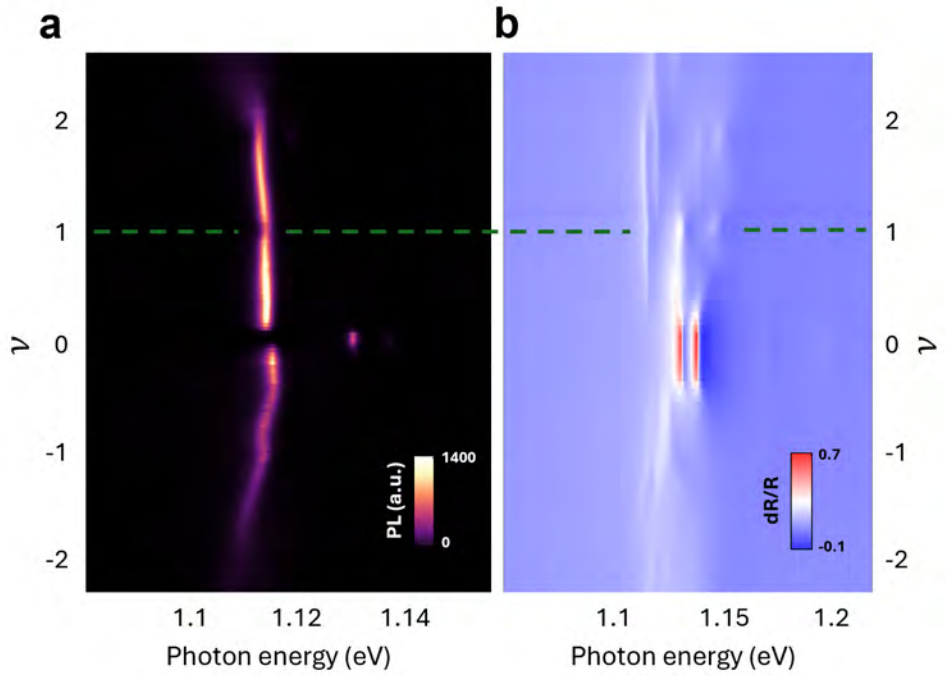

Figure 5.2: Doping dependent a) PL and b) dR/R from Device M1. The green dashed line is a guide to the eye indicating which features in the PL and dR/R spectra line up with $\nu = 1$.

ential reflectance spectrum in panel b further supports this, as the exciton resonance gains oscillator strength at $\nu = 1$ due to reduced electronic screening as the sample becomes more insulating.

An example of using PL as an indicator of the sample's dielectric environemtn is shown in Fig. 5.3. Panel a shows the integrated intensity of the trion peak as a function of out-of-plane electric field and filling factor. The checkerboard pattern in the doping ranges between $\nu = -1$ and $\nu = 0$ and between $\nu = 0$ and $\nu = 1$ is likely a result of layer dependent screening in those regions. For example, at $\nu > 0$, the excitons in the system bind with itinerant electrons to form negatively charged trions in both layers. As we have defined a positive electric field as pointing from the top gate electrode to the bottom, for $D/\epsilon_0 > 0$ the free electrons are pulled to the top layer, screening emission upwards towards the collection objective. On the other hand, for $D/\epsilon_0 > 0$ free electrons are depleted from the top layer, so screening of the trion emission upwards is reduced. As the sign of the free carriers is opposite for $\nu < 0$, the sign of D/ϵ_0 resulting in the brightest trion emission also switches.

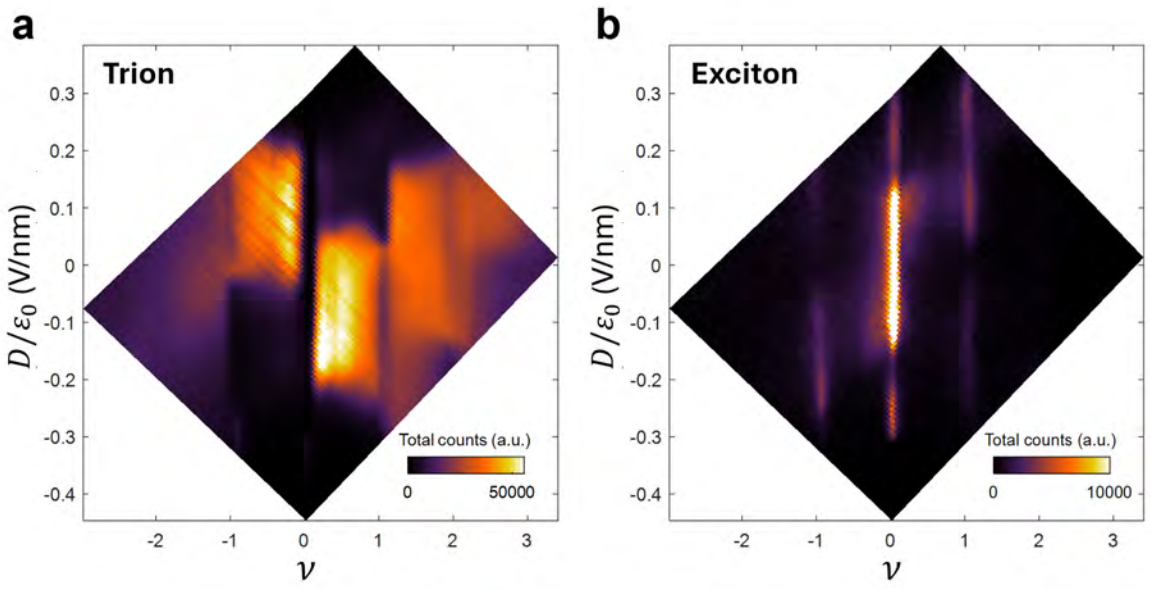

Figure 5.3: Integrated intensity of the a) trion energy range and b) exciton energy range with respect to doping and displacement field for Device M1.

Inspecting now the rest of the phase space mapped out by Fig. 5.3a, we see decreases in the trion intensity at filling factors of -1, 0, 1, and 2, indicating a more insulating environment at all these filling factors. Figure 5.3b displays the same data set, but now energy window the neutral exciton lies within is used as the integration window. Unsurprisingly, the exciton is bright at $\nu = 0$ and dark in metallic regions where trion emission is strongest. At $\nu = -1$ and $\nu = 1$, the exciton intensity re-emerges, but only for non-zero values of D/ϵ_0. Figure 5.4a shows a linecut of the same data set at $\nu = -1$ and $0 > D/\epsilon_0 > -0.2V/nm$. Indeed, the trion PL still dominates the spectrum near $D/\epsilon_0 = 0$, but with a larger out-of-plane electric field, the trion PL is completely quenched and the higher energy emission from the neutral exciton appears.

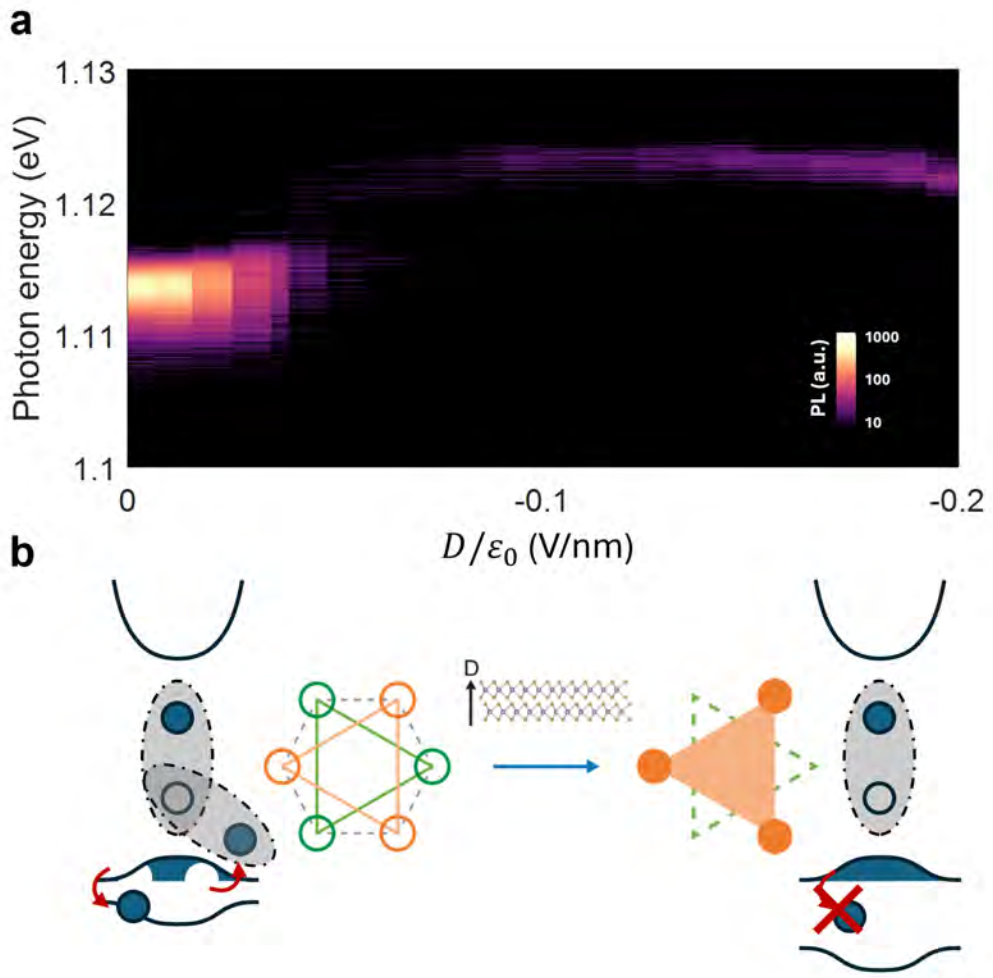

Figure 5.4: a) Electric field dependent PL at $\nu = -1$ for Device M1. b) Conceptual illustration of what is being demonstrated by a). The left side of b) demonstrates the case of small electric field, in which the $\nu = -1$ many-body gap is small enough to have frequent excitation of holes across the gap, allowing for the formation of positively charged trions. The right side of b) depicts the case for large electric field, in which the lattice is tuned to a triangular lattice and likely transitions to a Mott insulating state, at which point the Mott gap is larger and suppresses excitation of holes across the gap, thus suppressing trion formation and allowing for exciton radiative recombination instead.

Figure 5.4b presents a simplified picture of what is happening. Near $D/\epsilon_0 = 0$, the insulating gap is small, and thermal activation of free carriers allows for the creation of some trions. As D/ϵ_0 increases, the degeneracy between the XM and MX sites is lifted, until the sample transitions from a honeycomb lattice to an effective triangular lattice. The case of a half-filled triangular lattice has been extensively studied in the context of the Hubbard model, which predicts the formation of a

Mott insulating state in most cases [92] which, in this case, appears to have a larger insulating gap than the $D/\epsilon_0 = 0$ state.

As a final illustration of trion photoluminescence serving as a probe for charge order in $tMoTe_2$, Fig. 5.5 shows doping dependent photoluminescence from a cleaner device with a larger twist angle (M2) in panel a, accompanied by the extracted maximum intensity of the trion peak as a function doping in panel b. There are two clear dips in trion intensity at $\nu = -1$ and $\nu = -2/3$, along with a smaller dip occurring at $\nu = -3/5$. The next section will overview the other optical techniques that have been used to determine the identity of these three features.

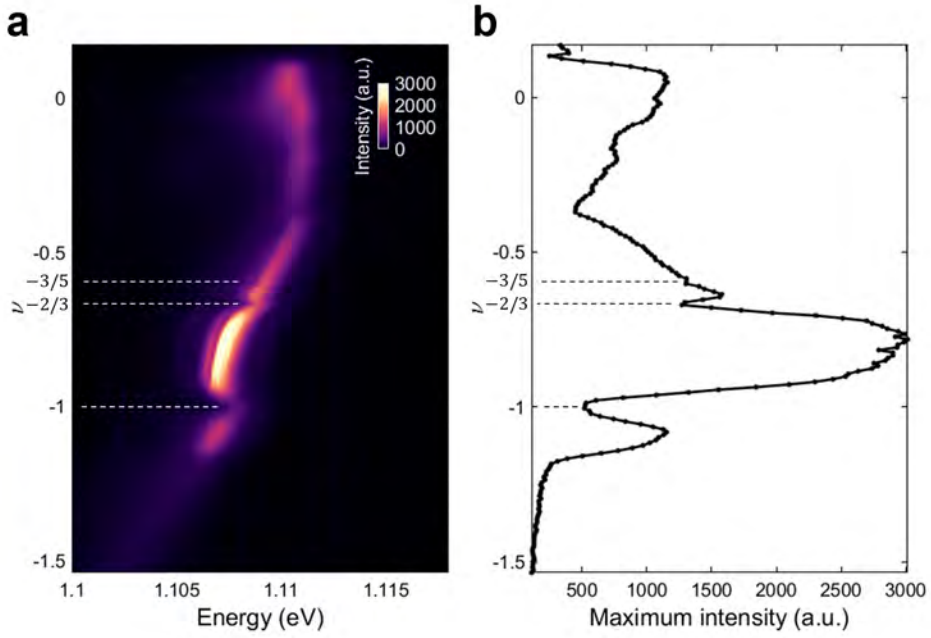

Figure 5.5: a) Doping dependent PL from Device M2. Notable kinks and dips in intensity can be seen at $\nu = -1$, $\nu = -2/3$, and $\nu = -3/5$. b) The maximum intensity of the spectra shown in a) at each doping value. There are dips in the maximum intensity at the same location as the kinks observed in a).

5.2 Optical detection of ferromagnetic phases

The topological phase considered in section 3.3.1 that has been predicted to exist in $tMoTe_2$ and similar systems has a prerequisite that the system have ferromagnetic order at $\nu = -1$ [18]. The inheritance of spin-valley locking from monolayer $MoTe_2$ and associated circular-polarization dependent optical selection rules mean polarization resolved reflectance and photoluminescence measurements are adequate to screen for ferromagnetic order in $tMoTe_2$.

5.2.1 RMCD

Figure 5.6a shows a doping dependent differential reflectance measurement where the probe light is linearly polarized and then the $\sigma+$ and $\sigma-$ components of the reflected signal are measured. Below a carrier density of approximately $-2x10^{12}cm^{-2}$ a clear difference between the $\sigma+$ and $\sigma-$ polarized reflectance appears. This is indicative of spontaneously broken time reversal symmetry and the presence of a ferromagnetic phase.

To simply determine the regions of phase space where the sample is ferromagnetic, spectrally resolved measurements like differential reflectance are unnecessary and slow. Instead, reflective magnetic circular dichroism (RMCD), can be used to rapidly screen for ferromagnetic phases. Since RMCD contains no spectral information, care must be taken when choosing a wavelength to measure RMCD with. Based on the polarization-resolved reflectance from Fig. 5.6a, we can determine that an excitation source near 1110 nm will give the highest contrast between $\sigma+$ and $\sigma-$ reflection. Using a supercontinuum laser combined with a homebuilt monochromator, we can freely tune our wavelength in this range to obtain the optimal RMCD signal. An example of the RMCD data acquired is given in Fig. 5.6b, where RMCD is measured while an out-of-plane magnetic field is swept to obtain a hysteresis loop and determine the coercive field of the ferromagnetic phase at $\nu = -1$.

With RMCD, scanning through the entire n-D phase space becomes efficient, which is done in

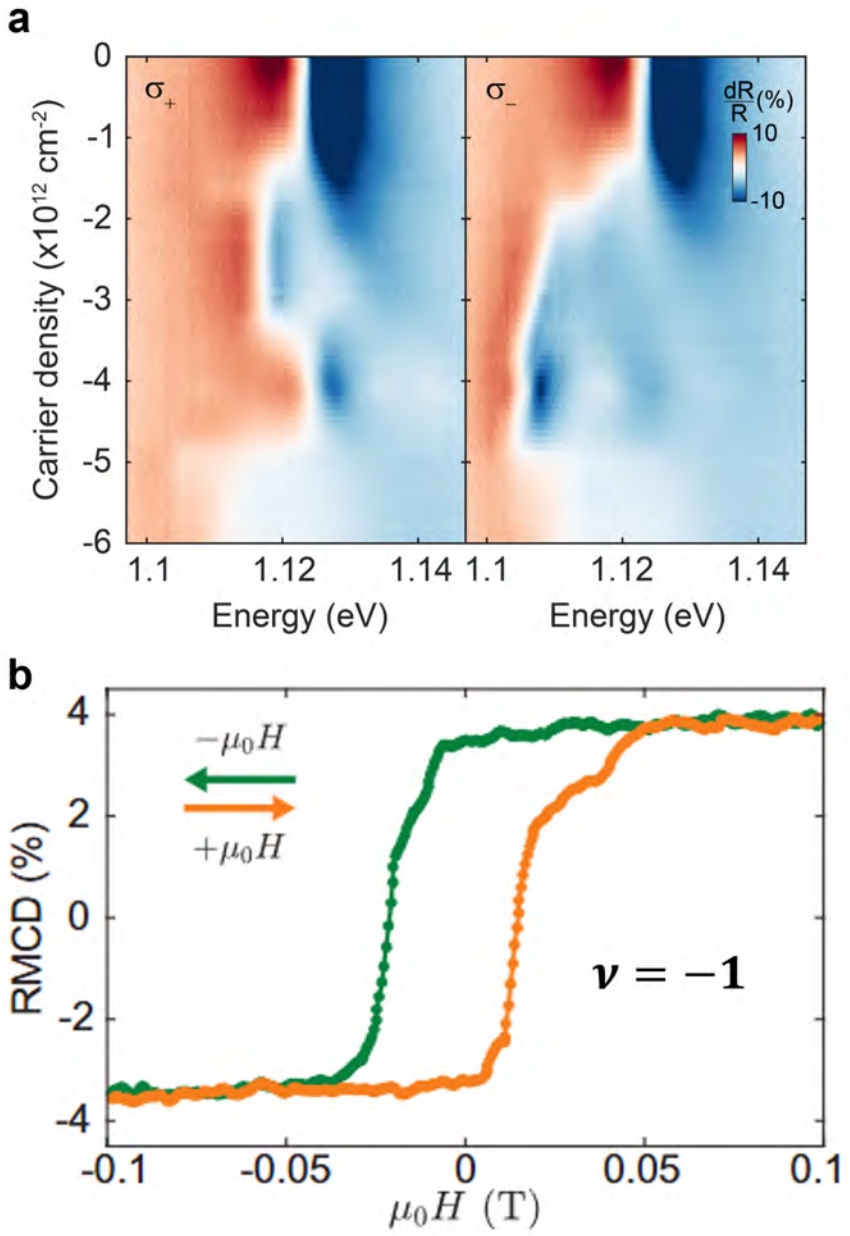

Figure 5.6: a) Polarization resolved dR/R spectra as a function of carrier density in Device M2. The $\sigma+$ ($\sigma-$) channel is shown on the left (right). b) Hysteresis loop of RMCD at $\nu = -1$ and zero displacement field using a probe laser tuned to to the trion resonance with a 30 meV bandwidth. Adapted from [85].

Fig. 5.7 and reveals the full extent of the ferromagnetic phase in the sample.

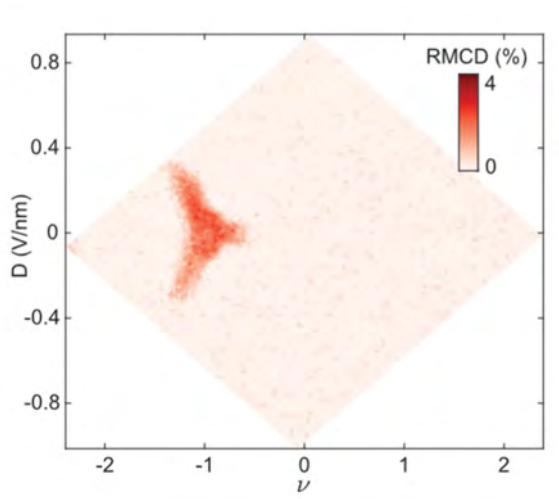

Figure 5.7: Doping and displacement field dependence of the zero-magnetic-field RMCD value in Device M2. Reproduced from [85].

5.3 Further investigations into the spectroscopic signatures of twisted $MoTe_2$

So far, the results discussed in this section are all well established at the time of writing. What follows in this section is a discussion of two unresolved spectroscopic measurements in $tMoTe_2$.

5.3.1 Dipolar exciton at $\nu = -1$

While RMCD and PL are powerful tools for probing $tMoTe_2$, they are each fundamentally restricted in their own way. For RMCD, the lack of spectral information means that outside of determining if there is an spin imbalance in the sample, there is little more information it can provide. PL, while containing spectral information and being able to probe spin-imbalance via trion polarization, is generally limited to information that can be gained from the trion alone. Any higher energy optical excitations in $tMoTe_2$ are quenched by the trion state. While higher excitation power would likely reveal higher energy excitonic species, it would also destroy the sensitive states that we are using PL to study in the first place.

An alternative here is differential reflectance. Figure 5.8a is a reproduction of Fig. 5.6a from earlier

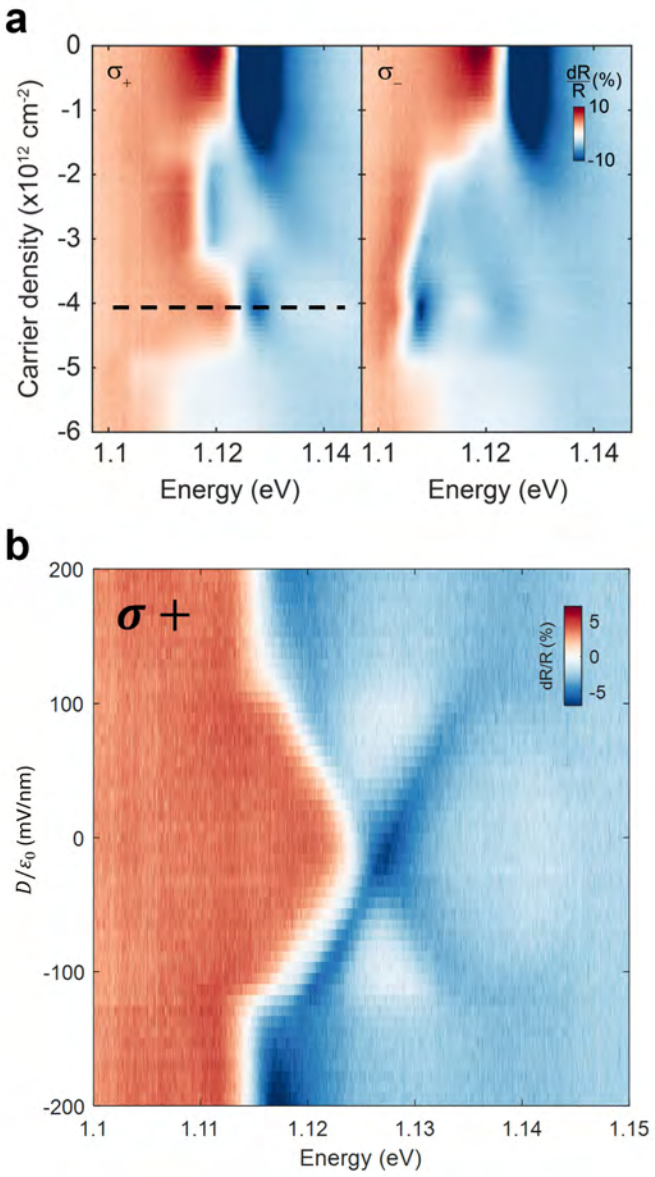

Figure 5.8: a) The same as Fig. 5.6a with a dashed line marking the doping value that b) is taken at. b) Electric field dependence of the $\sigma+$ polarized differential reflectance at $\nu = -1$.

in this chapter. While the $\sigma-$ spectrum on the left lacks any information that PL could not give, the $\sigma+$ channel shows a higher energy resonance that is absent in our PL measurements.

Figure 5.8b shows this higher energy $\sigma+$ polarized feature as a function of out-of-plane displacement field while the doping is held at $\nu = -1$. A clear "X" shape appears, generally indicating a

dipolar exciton experiencing a Stark shift. To better understand the origin of this resonance, it is necessary to extract the dipole moment from the slopes of the two features.

The lineshape of a resonance in a thin film heterostructure follows the form of Eq. (5.1) [117–119]

$$\frac{dR}{R}(E) = A * \left(\cos\alpha \frac{\gamma/2}{(E-E_0)^2+\gamma^2/4} + \sin\alpha \frac{E_0 - E}{(E-E_0)^2+\gamma^2/4} \right) \tag{5.1}$$

An example fit using only two resonances is shown in Fig. 5.9a. The residuals of the fit have clear structure to them, indicating failure of the fit equation to encompass the entirety of the spectrum. However, the addition of a third, broad, resonance to the fit equation in Fig. 5.9b corrects the error, leaving a random distribution of fit residuals, as expected from an accurate fit.

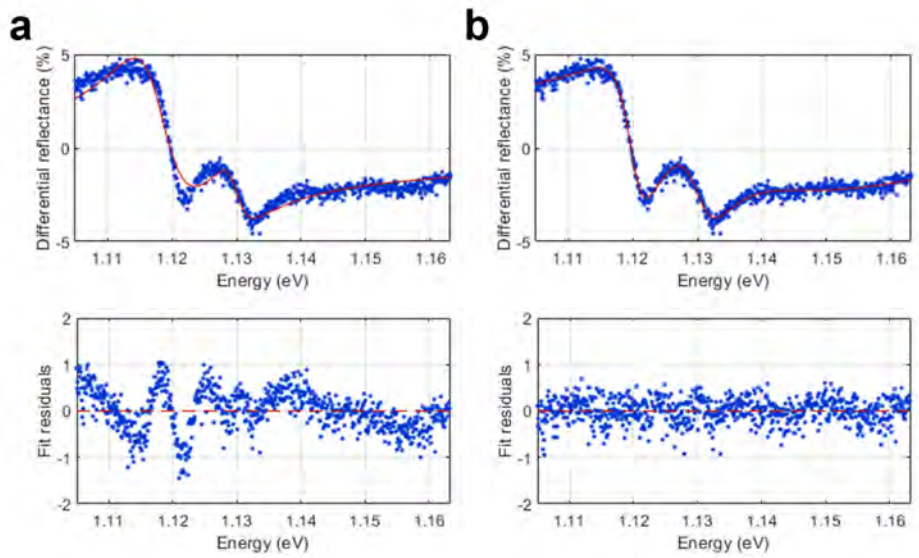

Figure 5.9: The blue dots in the top panels of a) and b) is the differential reflectance spectrum at $D/\epsilon_0 = 60mV/nm$ from Fig. 5.8b. The red line in the top panels of a) and b) is a fit with a) 2 resonances and b) 3 resonances to the data. The bottom panels of a) and b) show the residuals of the fit, with the red dashed line serving as a guide to the eye of where the zero is for the plot.

With the ability to simultaneously fit the two resonances, we proceed with fitting the spectra at all displacement field values and extracting the central energies of the two resonances. The results are shown in Fig. 5.10, with the black points being from spectra where the two resonances overlapped

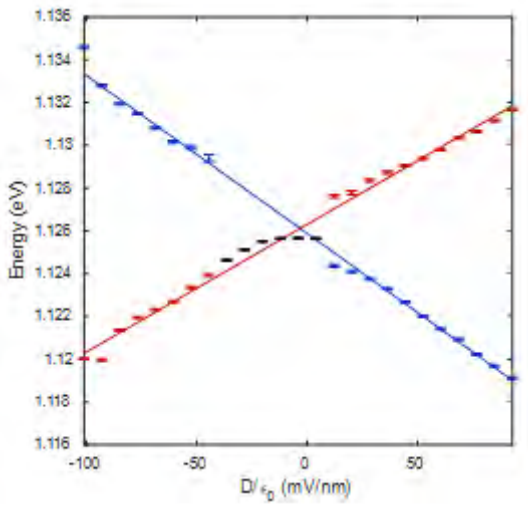

Figure 5.10: The red (blue) circles and error bars denote the extracted central energy and uncertainty for the first (second) resonance from Fig. 5.8b. The red (blue) line is a line of best fit to the extracted energy for the first (second) resonance. The black circles and error bars are the central energies for the single resonance that was used to fit the data in a limited displacement field range where the two resonances could not be fit independently. The data in black was removed when fitting the red and blue data points.

too much to be able to distinguish them via fitting. Omitting these points and then fitting the rest to a line yields an average slope of $0.067 \pm 0.002 \frac{eV}{V/nm}$. Assuming the feature is a neutral exciton, then we can separate the average separation of the electron and hole wave functions with $d = \frac{D}{e} * \frac{\epsilon_{MoTe_2}}{\epsilon hBN}$ gives an average separation of 2.

5.3.2 A paramagnetic exciton in twisted $MoTe_2$

This section introduces one final unexplained spectroscopic feature of near AA stacked $tMoTe_2$. Figure 5.11a shows magnetic field dependent photoluminescence from sample M1 (2.7°) at neutral doping. The lower energy neutral exciton shifts linearly as expected, consistent with previous reports [52]. However the higher energy feature has a clear nonlinear shift, with a quadratic fit shown in panel b fitting well. Interestingly, the quadratic shift is paramagnetic, despite high magnetic field studies repeatedly showing TMD excitons to have diamagnetic shifts at large field [52].

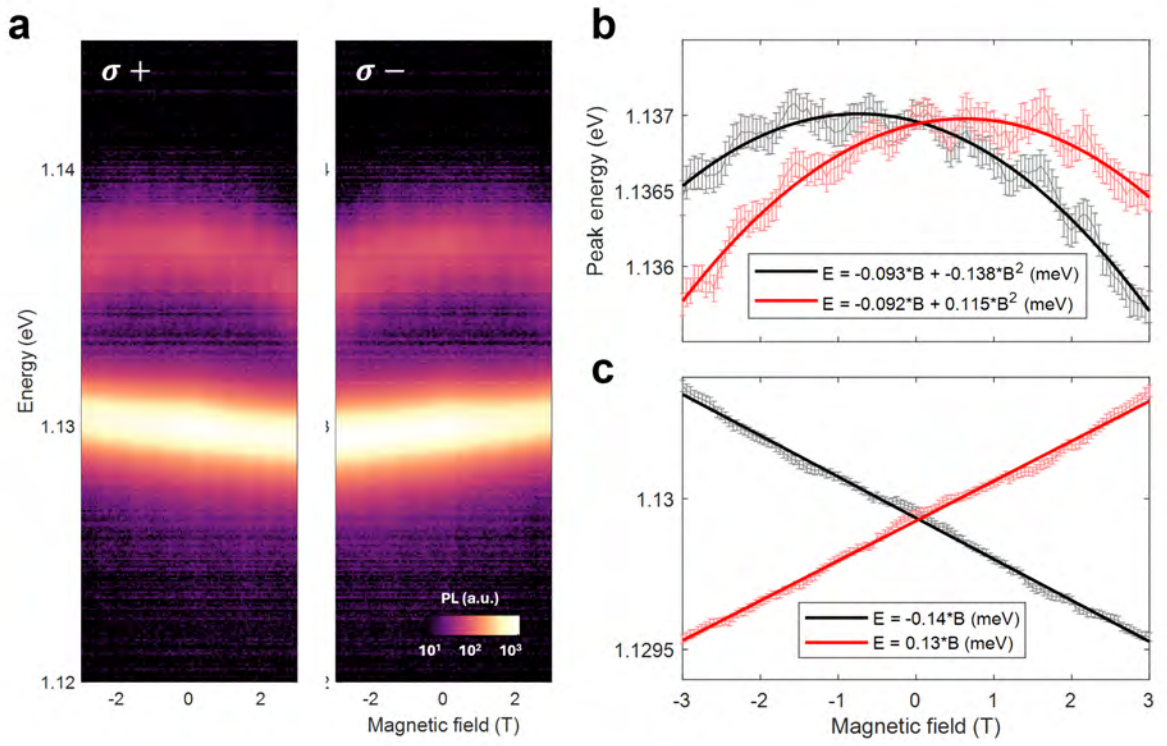

Figure 5.11: a) Magnetic field dependent PL for Device M1 taken at $\nu = 0$ and $D/\epsilon_0 = 0$. The $\sigma+$ ($\sigma-$) polarized PL is shown on the left (right). b) Quadratic fits of the fitted central energy for the high energy PL feature. c) Linear fits of the fitted central energy for the low energy PL feature.

Chapter 6
Optical control of topology in twisted $MoTe_2$

6.1 Experimental design

To achieve optical control of the topological states in $tMoTe_2$, we use an pump-probe protocol outlined in Fig. 6.1. Prior to the experiment, a known magnetization direction is prepared in the sample by sweeping the magnetic field to +300 mT at $\nu = -1$ and then sweeping the magnetic field back to 0 T and the gates back to charge neutrality. The initialization protocol then begins with the left panel of Fig. 6.1, with the sample in a non-FM state, typically at charge neutrality. Then, a circularly-polarized pump laser resonant with the trion is turned on and the gates are swept to the target gate voltages. During this time, the resonant pump laser excites trions in only one valley. In the case of the Fig. 6.1, the pump is $\sigma-$ polarized and thus photoexcites electron-hole pairs in the -K valley, which then bind with an itenerant hole in the +K valley to form a trion.

Once the gates reach their target value, for example $\nu = -1$, the pump beam is blocked and the gates are held constant. Next, a weak, linearly polarized probe beam is unblocked and polarization-resolved PL is recorded to determine the magnetization direction in the region that was pumped. Finally, the probe laser is blocked and the gates are swept back to charge neutrality before repeating the cycle for the next data point.

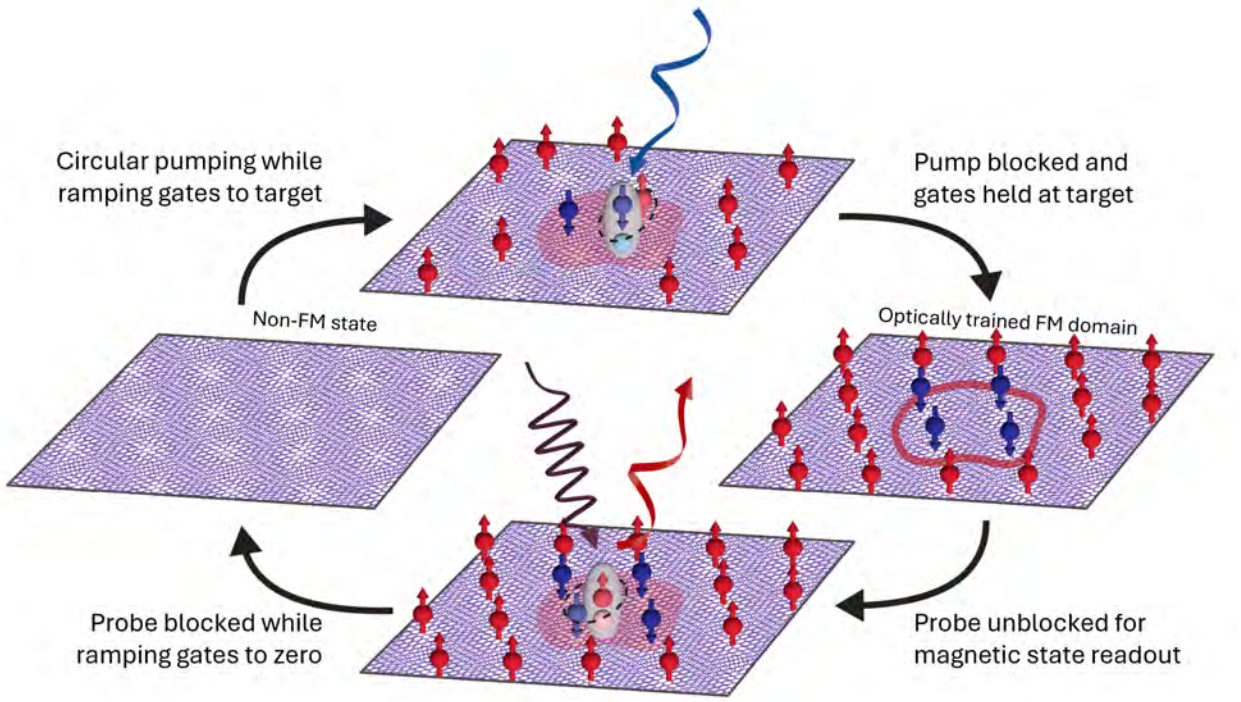

Figure 6.1: Schematic for the optical initialization protocol. The protocol begins in the left panel with the system in a non-FM state, typically at $\nu = 0$. Moving to the top panel, a circular pump resonant with the trion is turned on while the gates are ramped to the target voltages. Once the gates reach their targets, we move to the right panel, where the pump is turned off. Then, moving to the bottom panel, the weak 633 nm linearly polarized probe laser is turned on to readout the sign of the magnetic domain using poalarization-resolved PL. Finally, the probe laser is turned off and the sample is tuned back to a non-FM state before the process begins again with the left panel.

6.2 Gate-assisted optical training of topological states

Examples of the polarization-resolved PL spectra recorded during the experiment cycle detailed above are shown for filling factors $\nu = -1$ and $\nu = -2/3$ in Fig. 6.2a and b, respectively. The left side of a and b show the spectrum in the absence of the pump laser. The PL in this case is completely $\sigma-$ polarized, indicating that the sample is spin-up polarized. The right side of a and b show the spectra after a $\sigma-$ polarized pump is turned on during the gate sweep, as detailed in Fig. 6.1. Now, the PL is almost completely $\sigma+$ polarized, indicating that the domain being probed is

now spin-down polarized after the optical initialization process. Notably, in Fig. 6.2b, the emission after the pump is not fully polarized, likely due to the initialized domain being finite in size and slightly smaller than the region probed by the probe laser.

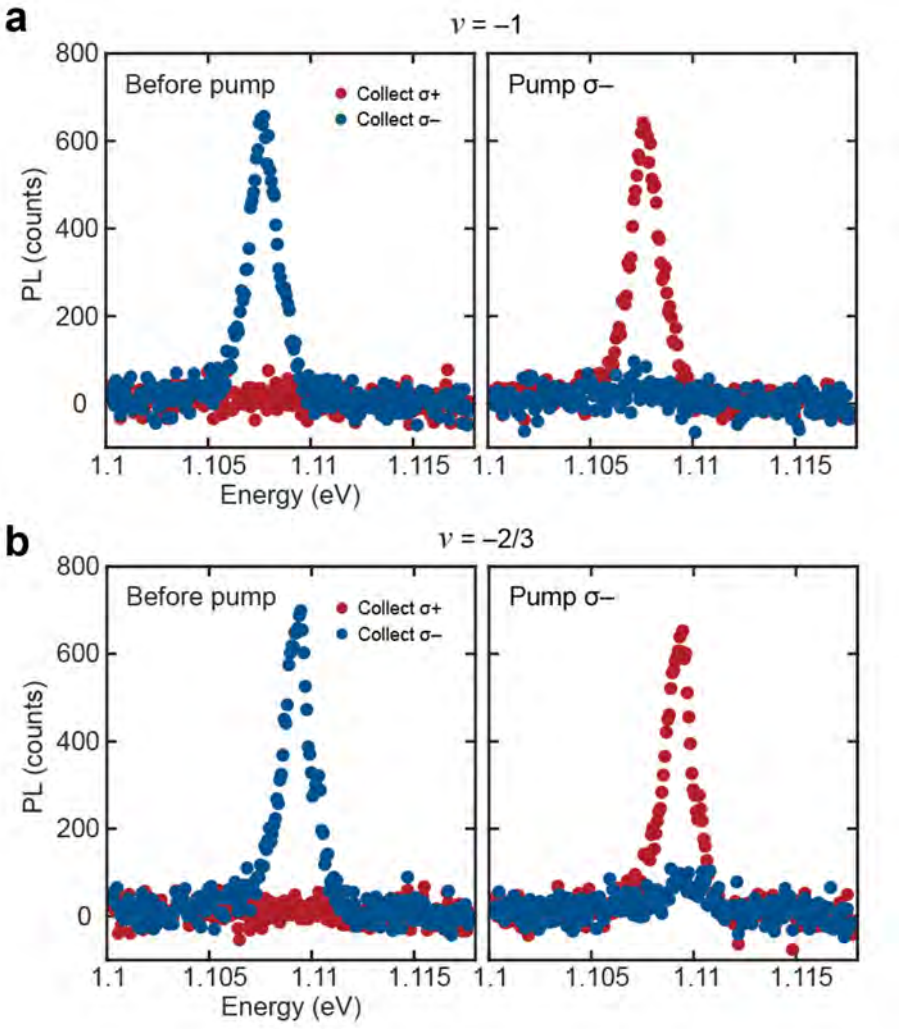

Figure 6.2: Spectra before and after the optical initialization protocol using a $\sigma-$ polarized pump at a) $\nu = -1$ and b) $\nu = -2/3$ for Device M2. Red (blue) data denotes $\sigma+$ ($\sigma-$) polarized PL. After the initialization protocol, the degree of circular polarization has completely flipped to be $\sigma+$ polarized, indicating formation of a spin-down despite the sample originally being trained to be spin-up.

Once a domain has been initialized in this manner, it is remarkably stable so long as the gates are held constant. An example of this is shown in Fig. 6.3. Once again, the sample was originally fully spin-up polarized before this measurement, and then a $\sigma-$ polarized pump laser was used to initial-

ized a spin-down $\nu = -1$ domain. The polarization resolved PL immediately after initialization is shown in panel a, confirming the domain is spin-down polarized. Panel b then shows just the $\sigma+$ polarized PL continuously measured for 1 hour after the domain was initialized while the gates were held constant.

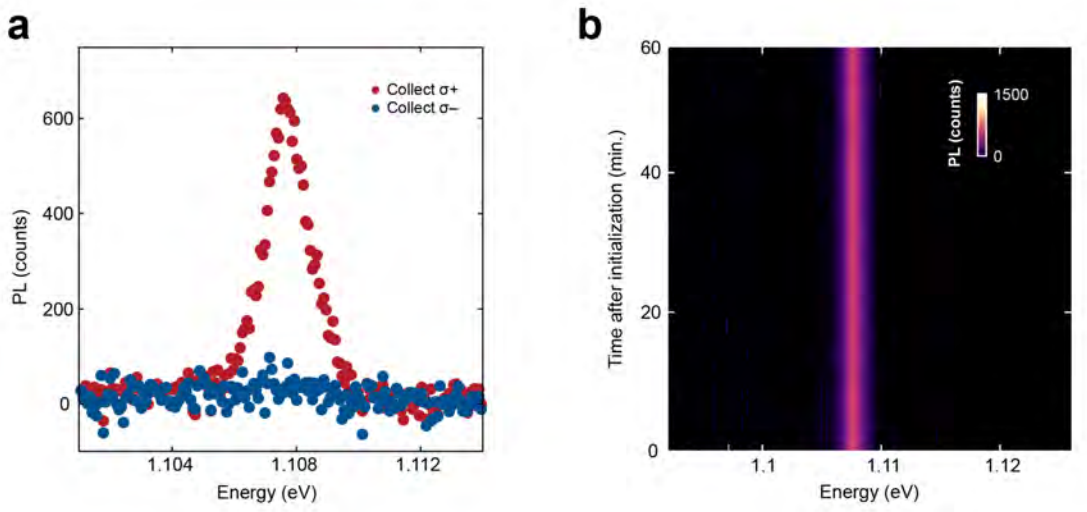

Figure 6.3: a) Polarization resolved PL at $\nu = -1$ after the optical initialization protocol using a $\sigma-$ polarized pump for Device M2. b) PL from the $\sigma+$ polarization channel, taken at 2 minute intervals over a 60 minute time period. There is no change in the PL, indicating the created domain is stable for a time period on the order of at least one hour.

Confirmation that this optical initialization effect relies on pumping resonantly with the trion is given by Fig. 6.4. Here, optical initialization of a spin-down domain at $\nu = -1$ with $\sigma-$ polarized light is attempted for various pump wavelengths before the magnetic state is readout with polarization resolved PL. The rightmost plot shows the degree of circular polarization (DOCP) after each initialization attempt. When the emission is $\sigma+$ polarized, that is when the DOCP plot is red, it means that a spin-down domain was successfully initialized despite the sample originally being spin-up polarized. As expected, when the pump photon energy falls too far below the energy of the trion, the optical initialization fails to generate a spin-down domain, as spin-polarized trions are no longer injuected into the sample by the pump laser.

The same type of experiment can be done but with a varying pump power, the results of which are

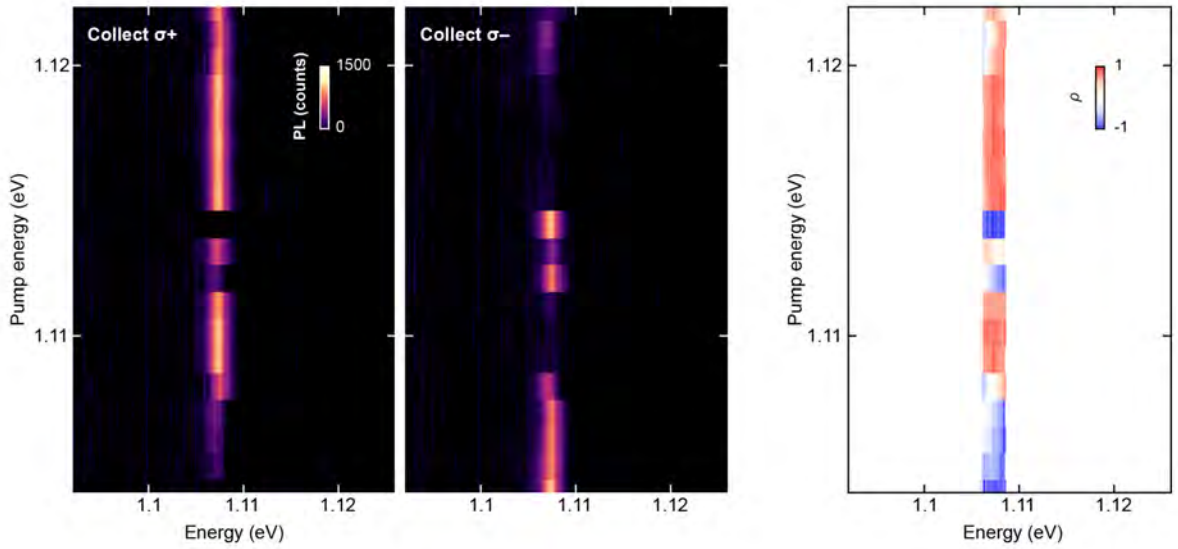

Figure 6.4: The left (middle) panel shows the $\sigma+$ ($\sigma-$) polarized PL after optical initialization is attempted with a 1 μW $\sigma-$ polarized pump at the specified pump energy. The right panel shows the resulting degree of circular polarization ρ. When ρ is positive, it means the optical initialization has succeeded. Data taken from Device M2.

shown in Fig. 6.5. It is important to not here that this time, the sample was originally trained to be spin-down polarized by a -300 mT magnetic field before performing the measurements at 0 T. As a result, Fig. 6.5 shows polarization resolved PL taken after attempting to initialize a spin-up domain with a $\sigma+$ polarized pump laser. As a result, the blue regions of this DOCP plot indicate that the initialization succeeded. Thus, we can determine that only with a sufficiently high pump power does the optical initialization protocol work.

6.2.1 Electrical control of the training mechanism

Now, the phase space for which optical initialization is possible will be explored more fully, starting with tuning the out-of-plane electric field. Once again, this measurement was performed after the sample was trained by a -300 mT magnetic field to be spin-down, so successful initialization of an opposite-sign domain will be evidenced by $\sigma-$ polarized emission.

Figure 6.6 shows the polarization-resolved PL after attempted optical initialization by a $\sigma+$ polar-

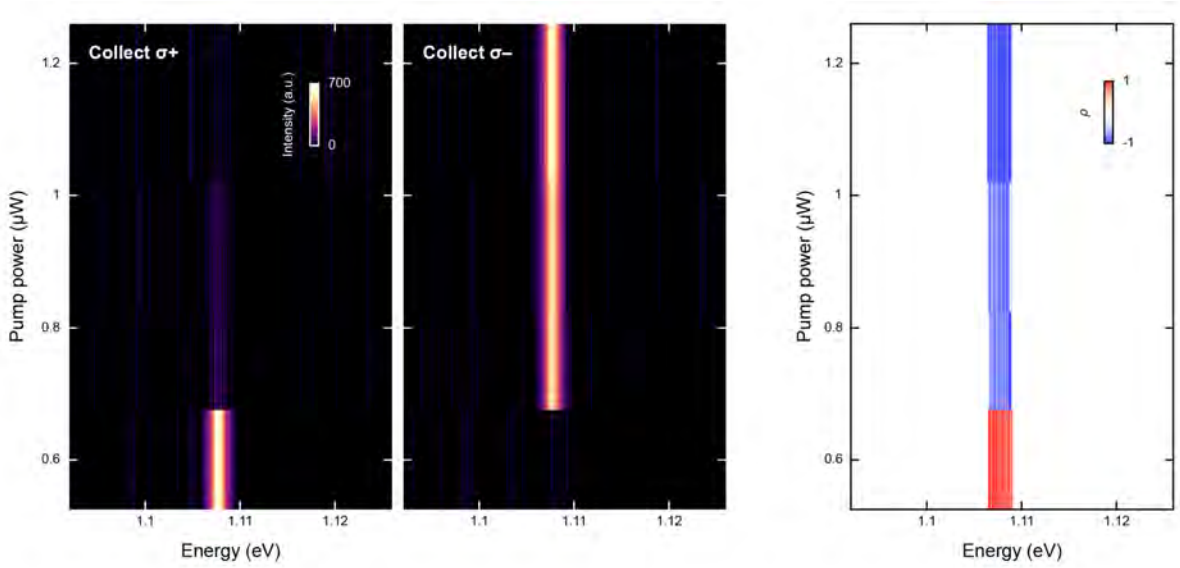

Figure 6.5: The left (middle) panel shows the $\sigma+$ ($\sigma-$) polarized PL after optical initialization is attempted with a $\sigma+$ polarized 1117 nm pump pumping with the specified pump power. The right panel shows the resulting degree of circular polarization ρ. In this data set, the sample was originally trained with $B < 0$ to be spin-down, and thus we initialized with a $\sigma+$ polarized pump to attempt to create a spin-up domain. As a result, $\rho < 0$ indicates that initialization of a spin-up domain is successful. Data taken from Device M2.

ized pump for $\nu = -1$ ($\nu = -2/3$) in panel a (b). Near 0 displacement field, the $\sigma-$ polarized emission indicates that initialization is successful. However, as the displacement field is increased, the sample remains ferromagnetic but the pump laser is no longer able to initialize a spin-up domain. Finally, at sufficiently high displacement field, the PL becomes unpolarized as the sample enters a likely AFM phase [85].

This behavior is reminiscent of transport results showing that in the integer and fractional Chern insulator states ($\nu = -1, -2/3$) as the out-of-plane displacement field is increased, the Chern gap first closes before a topologically trivial gap reopens, in which the sample is still ferromagnetic but no longer topological, before eventually leaving the FM phase entirely at higher still displacement field [20].

So far, data has only been shown at the $\nu = -1$ and $\nu = -2/3$. Figure 6.7 shows the results of optical intiailzation attempts as a function of doping. It is important to note that for this figure and all remaining figures in this section, the sample was originally trained to be spin-up by a +300

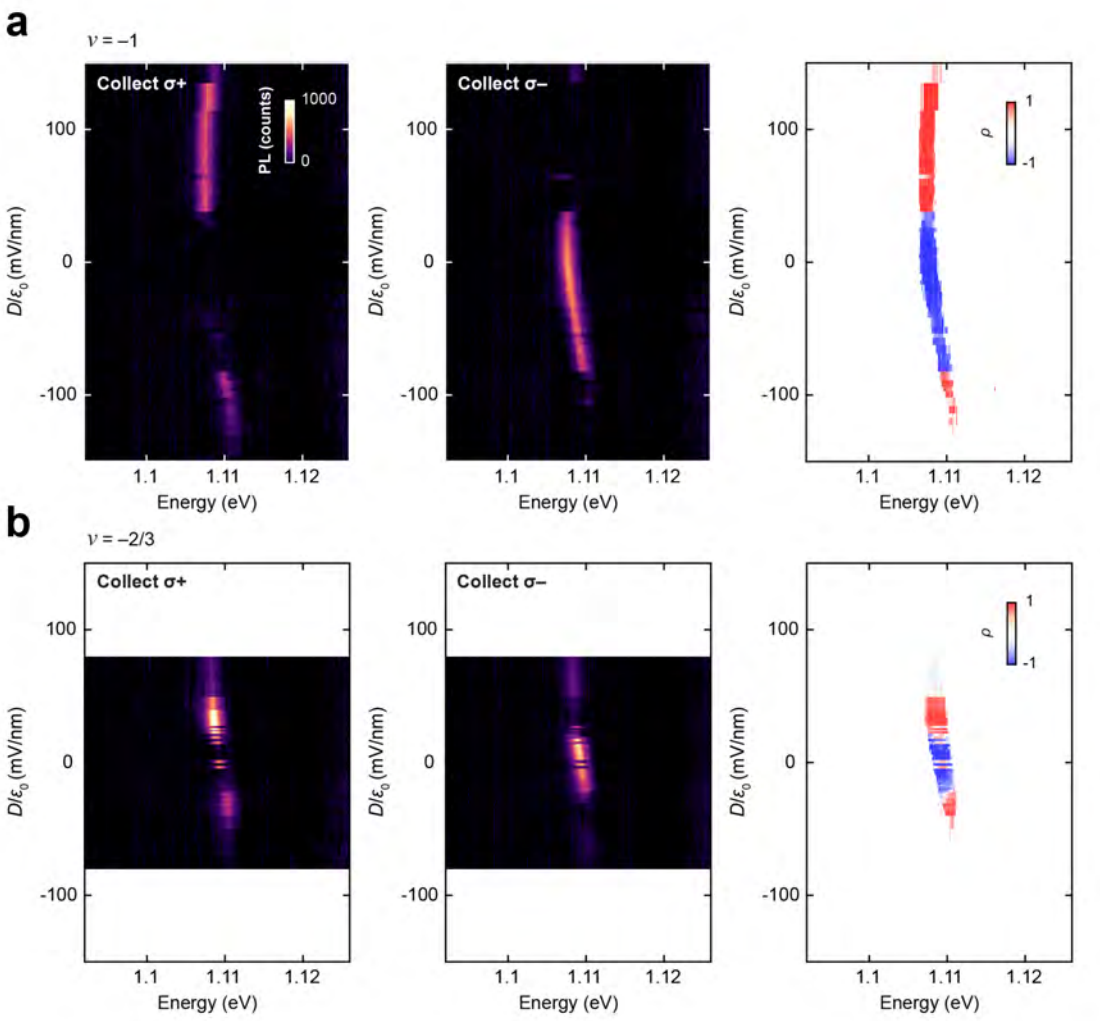

Figure 6.6: a) Polarization resolved PL and the resulting degree of circular polarization ρ after optical initialization is attempted at $\nu = -1$ at varying electric fields with a 1 μW, 1117 nm $\sigma+$ polarized pump. Optical initialization succeeded when $\rho < 0$. b) The same as a) but for $\nu = -2/3$. Data taken from Device M2.

mT field. So once again, successfully initializing a spin-down domain will be accompanied by $\sigma+$ polarized emission.

Figure 6.7a and b show the $\sigma+$ and $\sigma-$ polarized PL after attempting to initialized a spin-down domain with a $\sigma-$ polarized pump laser at various doping values. Panel c then shows the calculated DOCP. We find the optical initialization only succeeds near the integer and fractional Chern insulator states, while in the metallic or weakly insulating FM regimes away from the Chern states

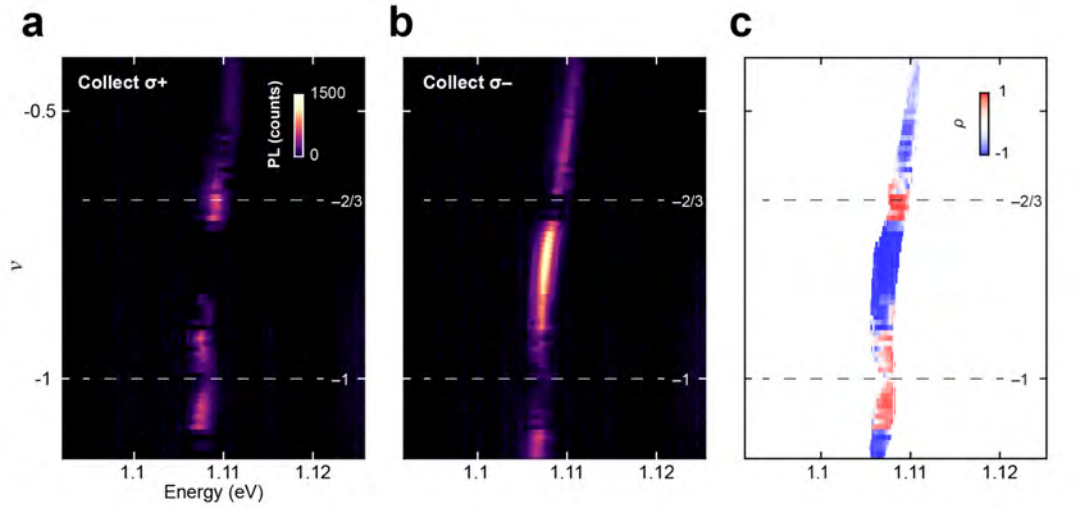

Figure 6.7: a) $\sigma+$ and b) $\sigma-$ polarized PL after optical initialization at the specified doping value is attempted with a 1 µW, 1117 nm $\sigma-$ polarized pump. c) The resulting degree of circular polarization. The sample was initially trainted to be spin-up with $B > 0$, so $\rho > 0$ indicates that a spin-down domain was successfully initialized by the $\sigma-$ polarized pump. All data take from Device M2.

see the pump laser unable to initialized a long-lived domain.

6.3 All optical switching of topological domains

It has already been shown that at sufficiently high power, a resonant, circularly polarized laser can selectively initialize either a spin-up or a spin-down domain via an effective spin-torque the is continuously applied while sweeping the gates in order to overwhelm the itinerant spin-polarized carriers from the rest of the sample. However, with both sufficiently high quality $MoTe_2$ crystals and high enough pump power, direct optical switching becomes possible.

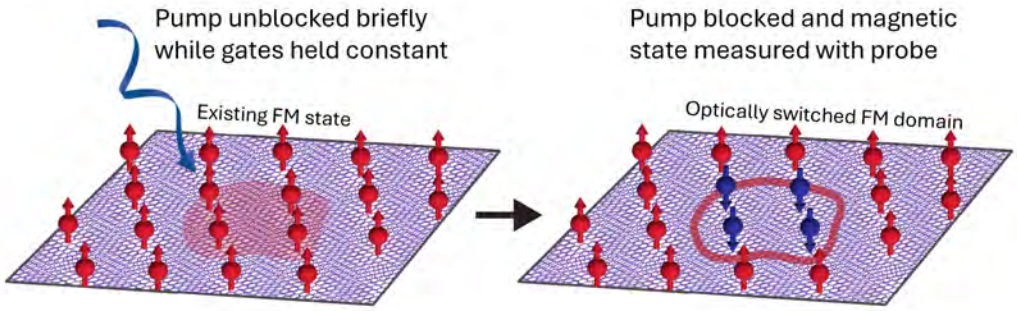

Figure 6.8: Illustration of the direct optical switching protocol. The sample begins in a FM state that has been previously trained to be spin-up by an external magnetic field. The $\sigma-$ pump is briefly unblocked, as shown in the left panel, before being blocked again. Then, the magnetic state of the domain is probed by turning on a linearly polarized probe laser to measure the polarization resolved PL.

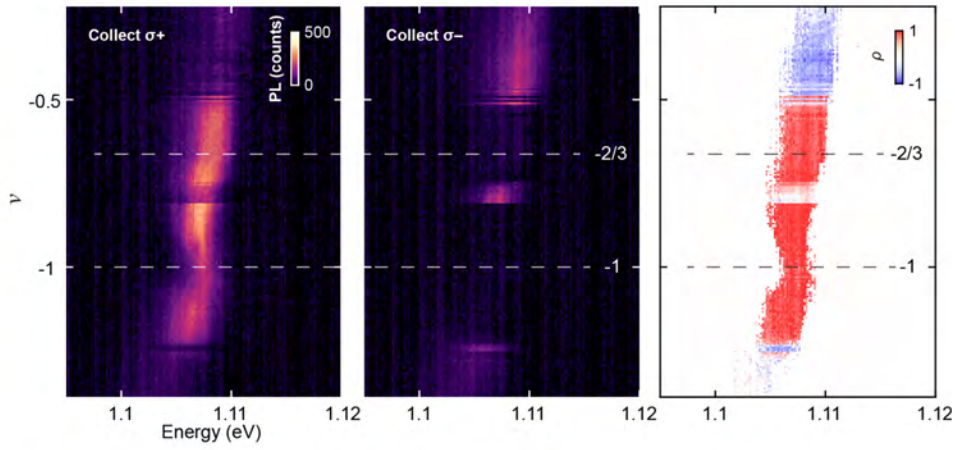

Figure 6.9: The left (middle) panel shows $\sigma+$ ($\sigma-$) polarized PL after attempting to optically switch the initially spin-up domain to be spin-down using a 4 μW, 1117 nm $\sigma-$ polarized pump. The right panel shows the resulting degree of circular polarization, where $\rho > 0$ indicates that the optical switching protocol succeeded in creating a spin-down domain for that doping value. Data taken from Device M3.

The protocol for a direct optical switching experiment is shown in Fig. 6.8. It consists of only three steps. First, the experimental parameters, i.e. gate values, are set to their desired value. Second, the circularly polarized pump laser is turned on for 5 seconds and back off, although the time the pump spends unblocked seems irrelevant. Finally, polarization resolved PL is measured in order to readout the magnetization direction of the domain. Once again, the sample is trained with a +300 mT magnetic field before all experiments, which are then performed at 0 T.

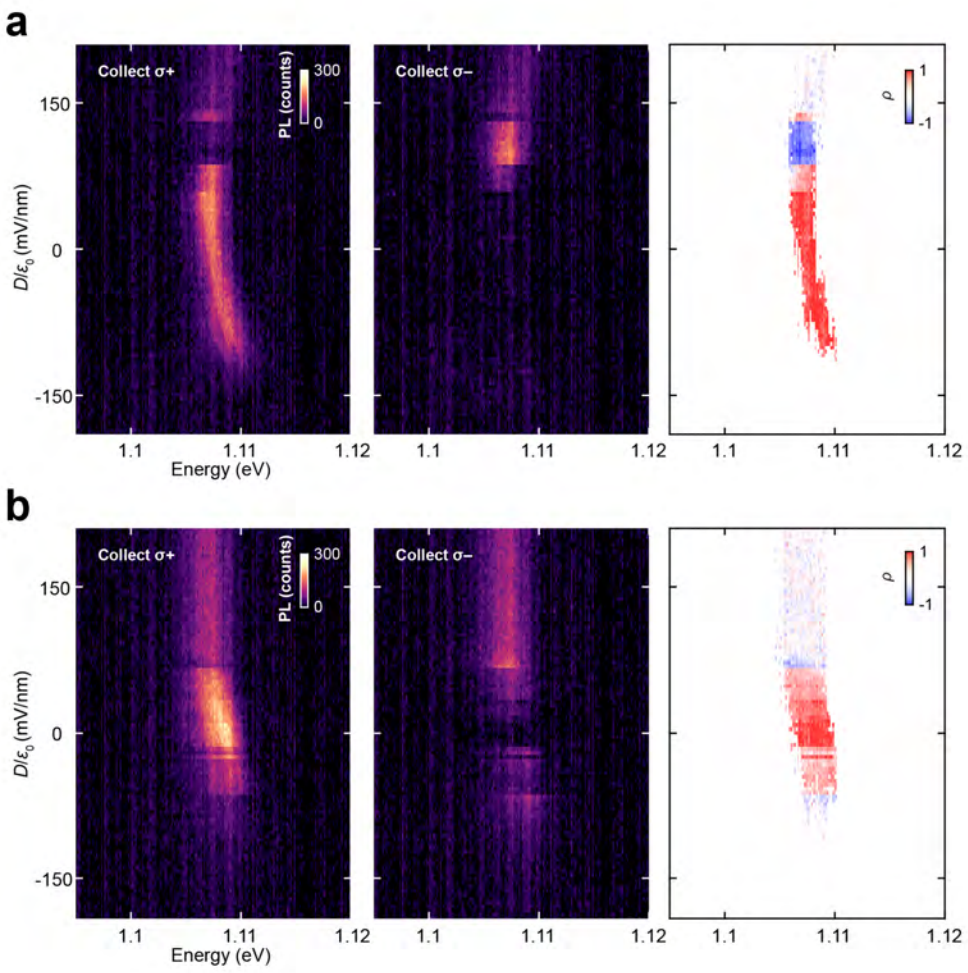

Figure 6.10: a) The left (middle) panel shows $\sigma+$ ($\sigma-$) polarized PL at after attempting to optically switch the initially spin-up domain to be spin-down using a 3 µW, 1110 nm $\sigma-$ polarized pump at $\nu = -1$. The right panel shows the resulting degree of circular polarization, where $\rho > 0$ indicates that the optical switching protocol succeeded in creating a spin-down domain for that calue of $D\epsilon_0$. b) The same as a) but at $\nu = -2/3$ instead of $\nu = -1$. Data taken from Device M3.

Figure 6.9 shows the results of direct optical switching using a $\sigma-$ polarized pump. While similar to Fig. 6.7, the doping range over which the initialization is successful is much larger.

A direct optical switching version of Fig. 6.6 is also shown in Fig. 6.10. The characteristics are similar, but once again the initialization is successful over a larger phase space than it's optical initialization counterpart.

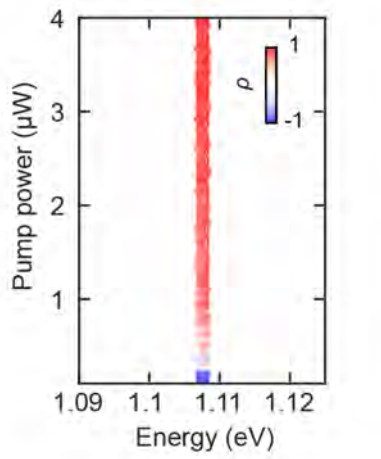

Figure 6.11: Pump power dependence of the optical switching behavior at $\nu = -1$ for a 1117 nm $\sigma-$ polarized pump. There is a clear power threshold below which optical switching fails. Data taken from Device M3.

Finally, a pump power dependence is also shown for the direct switching case in Fig. 6.11. Notably, the powers required for successfully switching the domain for this device (M3) is similar or even lower than what was required for optical initialization (M2). We attribute this to an increase in crystal quality between M3 and M2, as direct optical switching can also work for M2, just at higher power and over a more limited doping range, as evidenced by

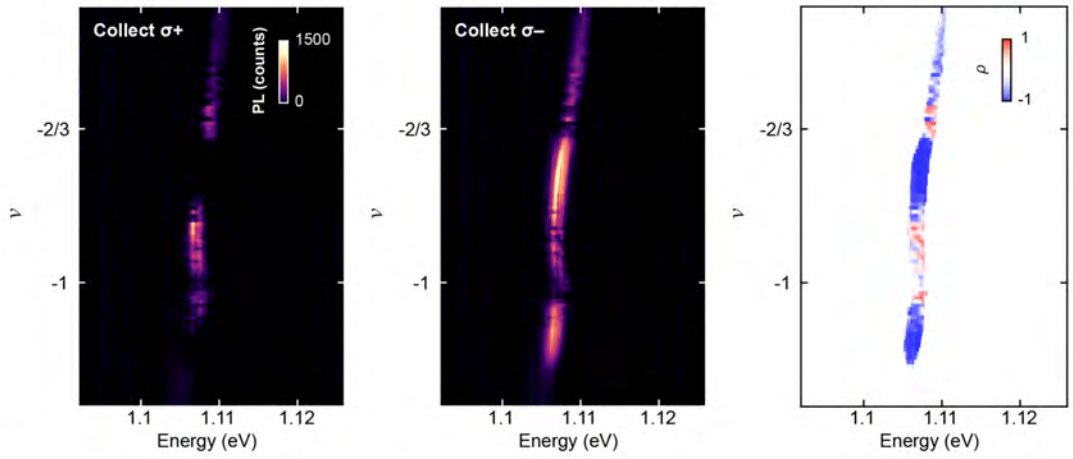

Figure 6.12: The same as Fig. 6.9 but for Device M2.

6.3.1 Repeatable writing of permanent domains

The direct optical switching effect is repeatable and extremely robust. Figure 6.13a shows polarization resolved PL spectra at $\nu = -2/3$ taken every 2 minutes over the course of 200 minutes, with a alternating circularly polarized PL pump being briefly turned on in between each spectra, repeatedly switching the measured domain between spin-up and spin-down states. Panel b shows a linecut of the DOCP measured during this process, illustrating its consistency.

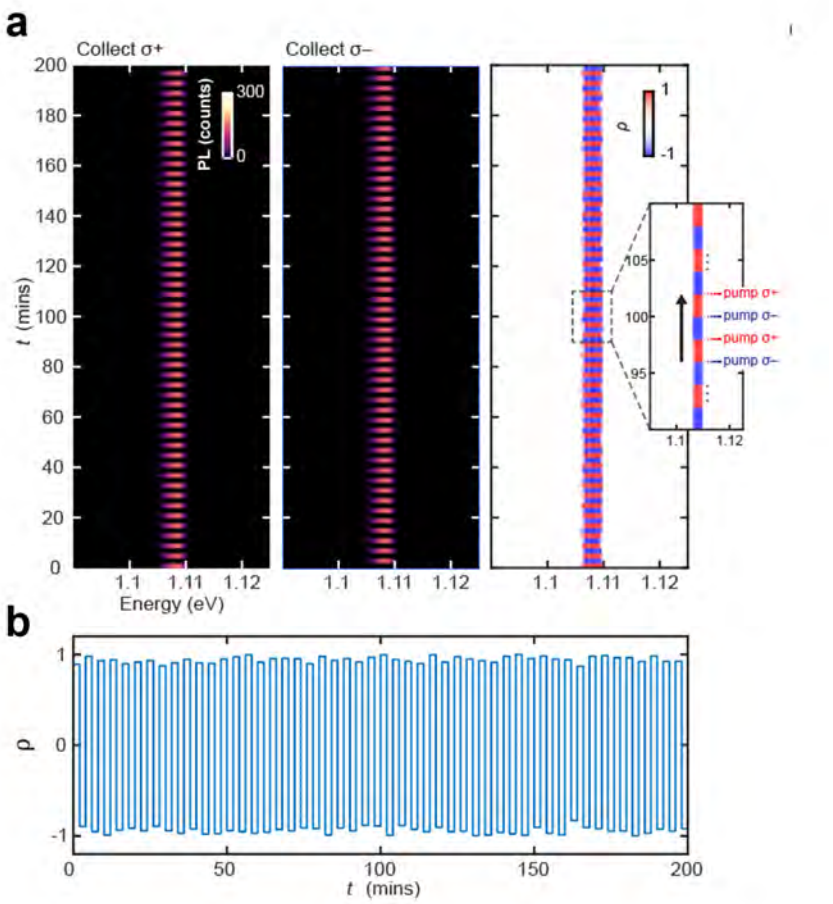

Figure 6.13: a) Polarization resolved PL for an optical switching sequence at $\nu = -2/3$ with a 3 μW, 1110 nm pump over the course of 200 minutes. The inset on the right shows the sequence order, in the domain is switched back and forth between a spin-up and spin-down domain by alternating pumping with $\sigma+$ and $\sigma-$ polarized light. b) The average value of ρ with respect to time. Full switching of the domain occurs every time. Data take from Device M3.

The same switching sequence was also done for $\nu = -1$, as shown in Fig. 6.14.

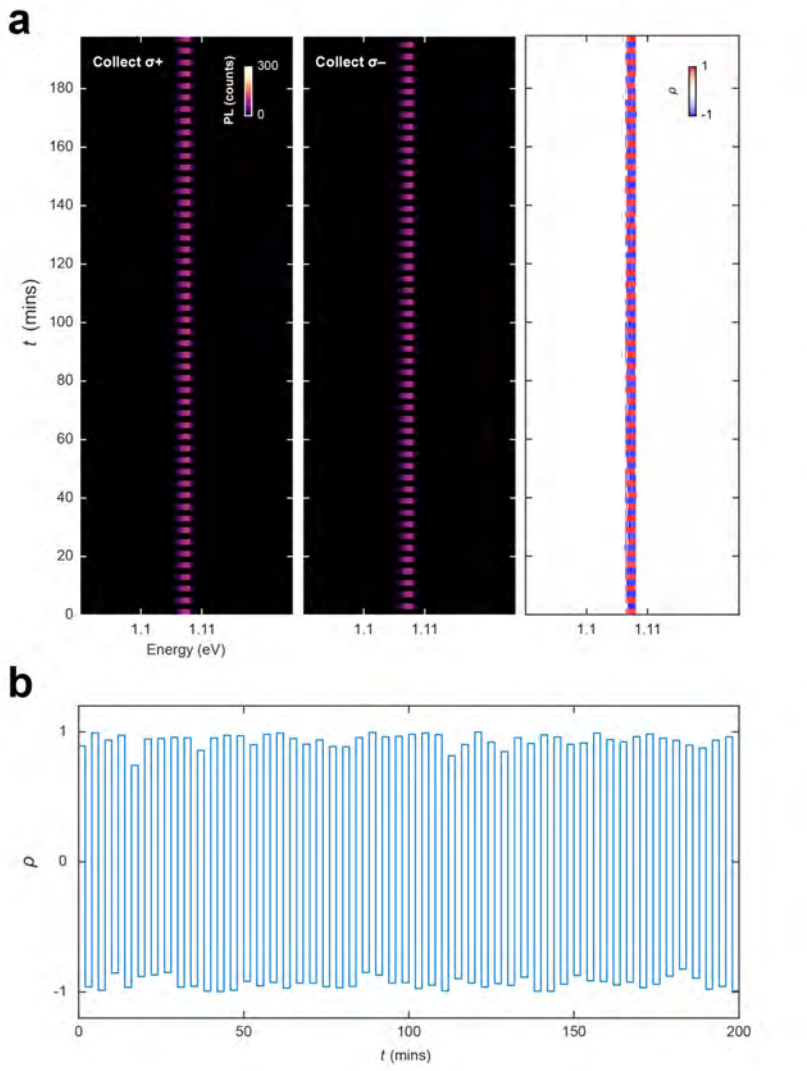

Figure 6.14: The same as Fig. 6.13 but for $\nu = -1$.

6.3.2 Domain mapping

After repeatedly implying that our pump was either initializing or directly switch a ”domain” and not the entire sample, it would be perhaps careless to not actually map out the sample to see if it is indeed a ”domain” that we are seeing initialized, and if so what it’s spatial extent it.

This is shown first for optical switching of $\nu = -2/3$ in device M3 in Fig. 6.15. Panel a shows the case of not turning the pump on at all, panel b shows the case of a 400 nW $\sigma-$ polarized pump, and panel c shows the case of a 600 nW $\sigma-$ polarized pump. As expected, when the pump is never

switched on, the entire $3.5x3.5\mu m^2$ region is uniformly $\sigma-$ polarized and thus spin-up. After turning on the 400 nW pump and then back off again, a roughly $1.5x2\mu m^2$ sized domain that has $\sigma+$ polarized PL and is thus spin-down, despite the surrounding sample still being spin-up. Finally, when the same thing is done with a 600 nW pump, the size of domain increases further.

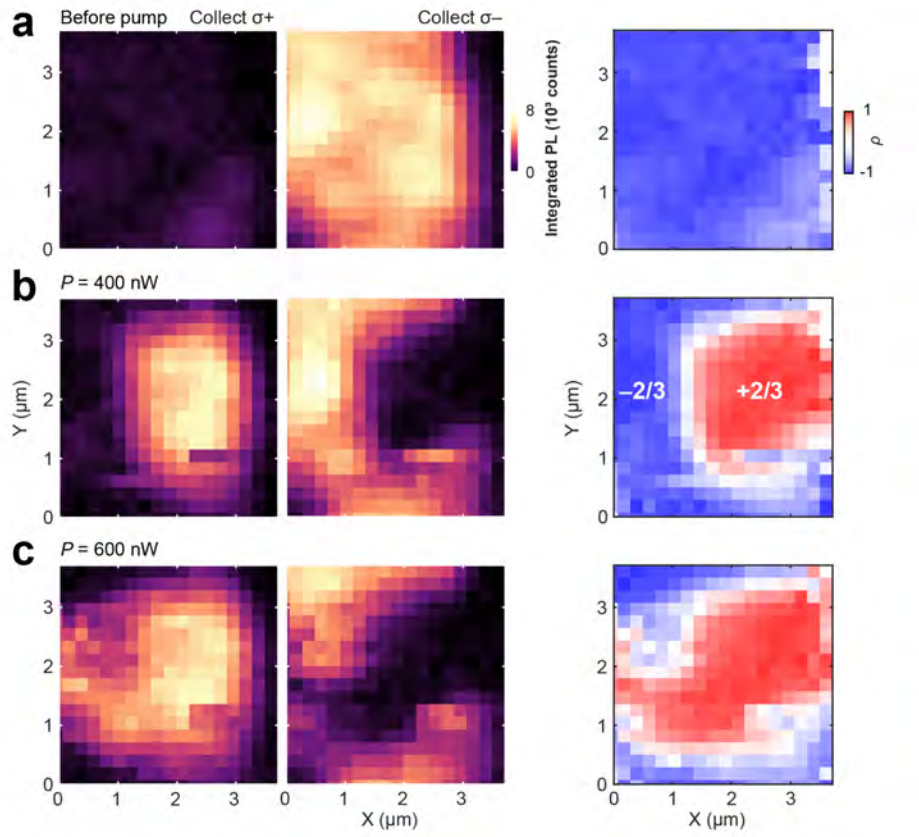

Figure 6.15: a) The left (middle) panel shows a spatial map of the integrated intensity for $\sigma+$ ($\sigma-$) polarized PL after the sample has been trained with a positive magnetic field and before the pump is turned on. The right panel shows the resulting degree of circular polarization ρ. b) The same as a) but after a 400 nW, 1117 nm $\sigma-$ polarized pump is briefly turned on to switch the domain to be spin-down. A spin-down domain with opposite Chern number as the rest of the sample is clearly visible. c) The same as b) but with a 600 nW pump. The initialized domain is nearly twice as large due to the increased pump power. All data taken from Device M3.

Figure 6.16 shows just the DOCP maps for the same type of measurement at $\nu = -1$. The results are roughly the same, but this time at a different spot on the sample which confines the domain on the right side by the graphite electrode.

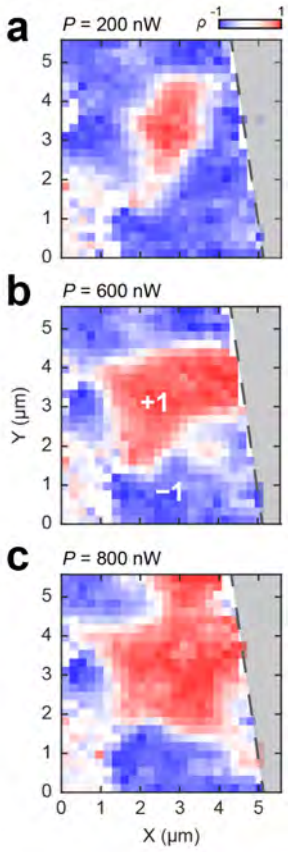

Figure 6.16: A spatial map of the degree of circular polarization of the PL after an 1117 nm a) 200 nW, b) 600 nW, or c) 800 nW $\sigma-$ polarized pump laser was used to create a spin-down domain at $\nu = -1$. Data taken from Device M3.

6.4 Outlook

In this chapter, we have demonstrated all-optical control over the magnetization direction, and thus sign of the Chern number, for integer and fractional Chern insulator domains of sizes up to 4 square microns. This opens up the possibility of selective patterning of Chern domains using a spatial light modulator, amplitude mask, or other spatial patterning technique.

Of course, with the opportunity for optical writing of spin-up and spin-down domains onto a sample, transport measurements become ever more interesting as a way to leverage the optical patterning technique.

Furthermore, there exists one remaining psuedospin in $tMoTe_2$ that we have not interacted with in this technique, that psuedospin being the layer psuedospin. By leveraging the dipolar exciton discussed in section 5.3.1, it may be possible to selectively pump carriers into the system that are both spin-valley polarized and layer-polarized. This could serve as a way to begin interacting with the layer psuedospin skyrmion lattice that gives rise to the topology in $tMoTe_2$, as well as allowing for potential control over any layer polarized states that might be found in $tMoTe_2$ [120].

References

1. Van Bommel, A. J., Crombeen, J. E. & Van Tooren, A. LEED and Auger electron observations of the SiC(0001) surface. *Surface Science* **48,** 463–472 (1975). https://doi.org/10.1016/0039-6028(75)90419-7.
2. Novoselov, K. S. *et al.* Electric field effect in atomically thin carbon films. *Science* **306,** 666–669 (2004). https://doi.org/10.1126/science.1102896.
3. Novoselov, K. S. *et al.* Two-dimensional gas of massless Dirac fermions in graphene. *Nature* **438,** 197–200 (2005). https://doi.org/10.1038/nature04233.
4. Zhang, Y., Tan, Y.-W., Stormer, H. L. & Kim, P. Experimental observation of the quantum Hall effect and Berry's phase in graphene. *Nature* **438,** 201–204 (2005). https://doi.org/10.1038/nature04235.
5. Novoselov, K. S. *et al.* Two-dimensional atomic crystals. *Proceedings of the National Academy of Sciences* **102,** 10451–10453 (2005). https://doi.org/10.1073/pnas.0502848102.
6. Dean, C. R. *et al.* Boron nitride substrates for high-quality graphene electronics. *Nature Nanotechnology* **5,** 722–726 (2010). https://doi.org/10.1038/nnano.2010.172.
7. Lopes dos Santos, J. M. B., Peres, N. M. R. & Castro Neto, A. H. Graphene bilayer with a twist: Electronic structure. *Physical Review Letters* **99,** 256802 (2007). https://doi.org/10.1103/PhysRevLett.99.256802.
8. Bistritzer, R. & MacDonald, A. H. Moiré bands in twisted double-layer graphene. *Proceedings of the National Academy of Sciences* **108,** 12233–12237 (2011). https://doi.org/10.1073/pnas.1108174108.
9. Rong, Z. Y. & Kuiper, P. Electronic effects in scanning tunneling microscopy: Moiré pattern on a graphite surface. *Physical Review B* **48,** 17427–17431 (1993). https://doi.org/10.1103/PhysRevB.48.17427.
10. Xiao, D., Liu, G.-B., Feng, W., Xu, X. & Yao, W. Coupled spin and valley physics in monolayers of MoS_2 and other group-VI dichalcogenides. *Physical Review Letters* **108,** 196802 (2012). https://doi.org/10.1103/PhysRevLett.108.196802.
11. Cao, T. *et al.* Valley-selective circular dichroism of monolayer molybdenum disulphide. *Nature Communications* **3,** 887 (2012). https://doi.org/10.1038/ncomms1882.
12. Mak, K. F., He, K., Shan, J. & Heinz, T. F. Control of valley polarization in monolayer MoS_2 by optical helicity. *Nature Nanotechnology* **7,** 494–498 (2012). https://doi.org/10.1038/nnano.2012.96.
13. Zeng, H., Dai, J., Yao, W., Xiao, D. & Cui, X. Valley polarization in MoS_2 monolayers by optical pumping. *Nature Nanotechnology* **7,** 490–493 (2012). https://doi.org/10.1038/nnano.2012.95.
14. Cao, Y. *et al.* Unconventional superconductivity in magic-angle graphene superlattices. *Nature* **556,** 43–50 (2018). https://doi.org/10.1038/nature26160.
15. Cao, Y. *et al.* Correlated insulator behaviour at half-filling in magic-angle graphene superlattices. *Nature* **556,** 80–84 (2018). https://doi.org/10.1038/nature26154.

16. Tang, Y. *et al.* Simulation of Hubbard model physics in WSe_2/WS_2 moiré superlattices. *Nature* **579,** 353–358 (2020). https://doi.org/10.1038/s41586-020-2085-3.

17. Regan, E. C. *et al.* Mott and generalized Wigner crystal states in WSe_2/WS_2 moiré superlattices. *Nature* **579,** 359–363 (2020). https://doi.org/10.1038/s41586-020-2092-4.

18. Wu, F., Lovorn, T., Tutuc, E., Martin, I. & MacDonald, A. H. Topological insulators in twisted transition metal dichalcogenide homobilayers. *Physical Review Letters* **122,** 086402 (2019). https://doi.org/10.1103/PhysRevLett.122.086402.

19. Cai, J. *et al.* Signatures of fractional quantum anomalous Hall states in twisted $MoTe_2$. *Nature* **622,** 63–68 (2023). https://doi.org/10.1038/s41586-023-06289-w.

20. Park, H. *et al.* Observation of fractionally quantized anomalous Hall effect. *Nature* **622,** 74–79 (2023). https://doi.org/10.1038/s41586-023-06536-0.

21. Xu, F. *et al.* Observation of integer and fractional quantum anomalous Hall effects in twisted bilayer $MoTe_2$. *Physical Review X* **13,** 031037 (2023). https://doi.org/10.1103/PhysRevX.13.031037.

22. Zeng, Y. *et al.* Thermodynamic evidence of fractional Chern insulator in moiré $MoTe_2$. *Nature* **622,** 69–73 (2023). https://doi.org/10.1038/s41586-023-06452-3.

23. Lu, Z. *et al.* Fractional quantum anomalous Hall effect in multilayer graphene. *Nature* **626,** 759–764 (2024). https://doi.org/10.1038/s41586-023-07010-7.

24. Dresselhaus, M., Dresselhaus, G., Cronin, S. & Souza Filho, A. G. *Solid State Properties: From Bulk to Nano* (Springer, Berlin, Germany, 2018).

25. Yu, P. & Cardona, M. *Fundamentals of Semiconductors: Physics and Materials Properties* 788 pp. Google Books: 5aBuKYBT_hsC (Springer Science & Business Media, 2010).

26. Dickinson, R. G. & Pauling, L. The crystal structure of molybdenite. *Journal of the American Chemical Society* **45,** 1466–1471 (1923). https://doi.org/10.1021/ja01659a020.

27. Wilson, J. & Yoffe, A. The transition metal dichalcogenides discussion and interpretation of the observed optical, electrical and structural properties. *Advances in Physics* **18,** 193–335 (1969). https://doi.org/10.1080/00018736900101307.

28. Momma, K. & Izumi, F. VESTA 3 for three-dimensional visualization of crystal, volumetric and morphology data. *Journal of Applied Crystallography* **44,** 1272–1276 (2011). https://doi.org/10.1107/S0021889811038970.

29. Wilson, J., Di Salvo, F. & Mahajan, S. Charge-density waves and superlattices in the metallic layered transition metal dichalcogenides. *Advances in Physics* **24,** 117–201 (1975). https://doi.org/10.1080/00018737500101391.

30. Sipos, B. *et al.* From Mott state to superconductivity in 1T-TaS_2. *Nature Materials* **7,** 960–965 (2008). https://doi.org/10.1038/nmat2318.

31. Fei, Z. *et al.* Edge conduction in monolayer WTe_2. *Nature Physics* **13,** 677–682 (2017). https://doi.org/10.1038/nphys4091.

32. Wu, S. *et al.* Observation of the quantum spin Hall effect up to 100 kelvin in a monolayer crystal. *Science* **359,** 76–79 (2018). https://doi.org/10.1126/science.aan6003.

33. Tang, S. *et al.* Quantum spin Hall state in monolayer 1T'-WTe_2. *Nature Physics* **13,** 683–687 (2017). https://doi.org/10.1038/nphys4174.

34. Cucchi, I. *et al.* Microfocus laser–angle-resolved photoemission on encapsulated mono-, bi-, and few-layer 1T'-WTe_2. *Nano Letters* **19,** 554–560 (2019). https://doi.org/10.1021/acs.nanolett.8b04534.

35. Shi, Y. *et al.* Imaging quantum spin Hall edges in monolayer WTe_2. *Science Advances* **5,** eaat8799 (2019). https://doi.org/10.1126/sciadv.aat8799.

36. Sajadi, E. *et al.* Gate-induced superconductivity in a monolayer topological insulator. *Science* **362,** 922–925 (2018). https://doi.org/10.1126/science.aar4426.

37. Fei, Z. *et al.* Ferroelectric switching of a two-dimensional metal. *Nature* **560,** 336–339 (2018). https://doi.org/10.1038/s41586-018-0336-3.

38. Li, T. & Galli, G. Electronic properties of MoS_2 Nanoparticles. *The Journal of Physical Chemistry C* **111,** 16192–16196 (2007). https://doi.org/10.1021/jp075424v.

39. Lebègue, S. & Eriksson, O. Electronic structure of two-dimensional crystals from ab initio theory. *Physical Review B* **79,** 115409 (2009). https://doi.org/10.1103/PhysRevB.79.115409.

40. Zhu, Z. Y., Cheng, Y. C. & Schwingenschlögl, U. Giant spin-orbit-induced spin splitting in two-dimensional transition-metal dichalcogenide semiconductors. *Physical Review B* **84,** 153402 (2011). https://doi.org/10.1103/PhysRevB.84.153402.

41. Yao, W., Xiao, D. & Niu, Q. Valley-dependent optoelectronics from inversion symmetry breaking. *Physical Review B* **77,** 235406 (2008). https://doi.org/10.1103/PhysRevB.77.235406.

42. Aivazian, G. *et al.* Magnetic control of valley pseudospin in monolayer WSe_2. *Nature Physics* **11,** 148–152 (2015). https://doi.org/10.1038/nphys3201.

43. Song, Y. & Dery, H. Transport theory of monolayer transition-metal dichalcogenides through symmetry. *Physical Review Letters* **111,** 026601 (2013). https://doi.org/10.1103/PhysRevLett.111.026601.

44. Xu, X., Yao, W., Xiao, D. & Heinz, T. F. Spin and pseudospins in layered transition metal dichalcogenides. *Nature Physics* **10,** 343–350 (2014). https://doi.org/10.1038/nphys2942.

45. Mak, K. F., Xiao, D. & Shan, J. Light–valley interactions in 2D semiconductors. *Nature Photonics* **12,** 451–460 (2018). https://doi.org/10.1038/s41566-018-0204-6.

46. Mak, K. F., McGill, K. L., Park, J. & McEuen, P. L. The valley Hall effect in MoS_2 transistors. *Science* **344,** 1489–1492 (2014). https://doi.org/10.1126/science.1250140.

47. Berkelbach, T. C., Hybertsen, M. S. & Reichman, D. R. Theory of neutral and charged excitons in monolayer transition metal dichalcogenides. *Physical Review B* **88,** 045318 (2013). https://doi.org/10.1103/PhysRevB.88.045318.

48. Mak, K. F. *et al.* Tightly bound trions in monolayer MoS_2. *Nature Materials* **12,** 207–211 (2013). https://doi.org/10.1038/nmat3505.

49. Ross, J. S. *et al.* Electrical control of neutral and charged excitons in a monolayer semiconductor. *Nature Communications* **4,** 1474 (2013). https://doi.org/10.1038/ncomms2498.

50. Yu, H., Liu, G.-B., Gong, P., Xu, X. & Yao, W. Dirac cones and Dirac saddle points of bright excitons in monolayer transition metal dichalcogenides. *Nature Communications* **5,** 3876 (2014). https://doi.org/10.1038/ncomms4876.

51. Singh, A. *et al.* Long-lived valley polarization of intravalley trions in monolayer WSe_2. *Physical Review Letters* **117,** 257402 (2016). https://doi.org/10.1103/PhysRevLett.117.257402.

52. Stier, A. V., McCreary, K. M., Jonker, B. T., Kono, J. & Crooker, S. A. Exciton diamagnetic shifts and valley Zeeman effects in monolayer WS_2 and MoS_2 to 65 Tesla. *Nature Communications* **7,** 10643 (2016). https://doi.org/10.1038/ncomms10643.

53. He, M. *et al.* Valley phonons and exciton complexes in a monolayer semiconductor. *Nature Communications* **11,** 618 (2020). https://doi.org/10.1038/s41467-020-14472-0.

54. Förste, J. *et al.* Exciton g-factors in monolayer and bilayer WSe_2 from experiment and theory. *Nature Communications* **11,** 4539 (2020). https://doi.org/10.1038/s41467-020-18019-1.

55. Li, Z. *et al.* Momentum-dark intervalley exciton in monolayer tungsten diselenide brightened *via* chiral phonon. *ACS Nano* **13,** 14107–14113 (2019). https://doi.org/10.1021/acsnano.9b06682.
56. Liu, E. *et al.* Valley-selective chiral phonon replicas of dark excitons and trions in monolayer WSe_2. *Physical Review Research* **1,** 032007 (2019). https://doi.org/10.1103/PhysRevResearch.1.032007.
57. Castellanos-Gomez, A. *et al.* Deterministic transfer of two-dimensional materials by all-dry viscoelastic stamping. *2D Materials* **1,** 011002 (2014). https://doi.org/10.1088/2053-1583/1/1/011002.
58. Splendiani, A. *et al.* Emerging photoluminescence in monolayer MoS_2. *Nano Letters* **10,** 1271–1275 (2010). https://doi.org/10.1021/nl903868w.
59. Mak, K. F., Lee, C., Hone, J., Shan, J. & Heinz, T. F. Atomically thin MoS_2: A new direct-gap semiconductor. *Physical Review Letters* **105,** 136805 (2010). https://doi.org/10.1103/PhysRevLett.105.136805.
60. Jones, A. M. *et al.* Spin–layer locking effects in optical orientation of exciton spin in bilayer WSe_2. *Nature Physics* **10,** 130–134 (2014). https://doi.org/10.1038/nphys2848.
61. Arora, A. *et al.* Valley-contrasting optics of interlayer excitons in Mo- and W-based bulk transition metal dichalcogenides. *Nanoscale* **10,** 15571–15577 (2018). https://doi.org/10.1039/C8NR03764G.
62. Zhang, Y. *et al.* Every-other-layer dipolar excitons in a spin-valley locked superlattice. *Nature Nanotechnology* **18,** 501–506 (2023). https://doi.org/10.1038/s41565-023-01350-1.
63. Shi, Q. *et al.* Bilayer WSe2 as a natural platform for interlayer exciton condensates in the strong coupling limit. *Nature Nanotechnology* **17,** 577–582 (2022). https://doi.org/10.1038/s41565-022-01104-5.
64. Terrones, H., López-Urías, F. & Terrones, M. Novel hetero-layered materials with tunable direct band gaps by sandwiching different metal disulfides and diselenides. *Scientific Reports* **3,** 1549 (2013). https://doi.org/10.1038/srep01549.
65. Kang, J., Tongay, S., Zhou, J., Li, J. & Wu, J. Band offsets and heterostructures of two-dimensional semiconductors. *Applied Physics Letters* **102,** 012111 (2013). https://doi.org/10.1063/1.4774090.
66. Kośmider, K. & Fernández-Rossier, J. Electronic properties of the MoS_2-WS_2 heterojunction. *Physical Review B* **87,** 075451 (2013). https://doi.org/10.1103/PhysRevB.87.075451.
67. Chaves, A. *et al.* Bandgap engineering of two-dimensional semiconductor materials. *npj 2D Materials and Applications* **4,** 1–21 (2020). https://doi.org/10.1038/s41699-020-0162-4.
68. Rivera, P. *et al.* Observation of long-lived interlayer excitons in monolayer $MoSe_2$–WSe_2 heterostructures. *Nature Communications* **6,** 6242 (2015). https://doi.org/10.1038/ncomms7242.
69. Ross, J. S. *et al.* Interlayer exciton optoelectronics in a 2D heterostructure p–n junction. *Nano Letters* **17,** 638–643 (2017). https://doi.org/10.1021/acs.nanolett.6b03398.
70. Wilson, N. R. *et al.* Determination of band offsets, hybridization, and exciton binding in 2D semiconductor heterostructures. *Science Advances* **3,** e1601832 (2017). https://doi.org/10.1126/sciadv.1601832.
71. Kim, J. *et al.* Observation of ultralong valley lifetime in WSe_2/MoS_2 heterostructures. *Science Advances* **3,** e1700518 (2017). https://doi.org/10.1126/sciadv.1700518.
72. Paik, E. Y. *et al.* Interlayer exciton laser of extended spatial coherence in atomically thin heterostructures. *Nature* **576,** 80–84 (2019). https://doi.org/10.1038/s41586-019-1779-x.

73. Robert, C. *et al.* Exciton radiative lifetime in transition metal dichalcogenide monolayers. *Physical Review B* **93,** 205423 (2016). https://doi.org/10.1103/PhysRevB.93.205423.

74. Robert, C. *et al.* Fine structure and lifetime of dark excitons in transition metal dichalcogenide monolayers. *Physical Review B* **96,** 155423 (2017). https://doi.org/10.1103/PhysRevB.96.155423.

75. Shinokita, K. *et al.* Continuous control and enhancement of excitonic valley polarization in monolayer WSe_2 by electrostatic doping. *Advanced Functional Materials* **29,** 1900260 (2019). https://doi.org/10.1002/adfm.201900260.

76. Rivera, P. *et al.* Valley-polarized exciton dynamics in a 2D semiconductor heterostructure. *Science* **351,** 688–691 (2016). https://doi.org/10.1126/science.aac7820.

77. Kuwabara, M., Clarke, D. R. & Smith, D. A. Anomalous superperiodicity in scanning tunneling microscope images of graphite. *Applied Physics Letters* **56,** 2396–2398 (1990). https://doi.org/10.1063/1.102906.

78. Suárez Morell, E., Correa, J. D., Vargas, P., Pacheco, M. & Barticevic, Z. Flat bands in slightly twisted bilayer graphene: Tight-binding calculations. *Physical Review B* **82,** 121407 (2010). https://doi.org/10.1103/PhysRevB.82.121407.

79. Trambly de Laissardière, G., Mayou, D. & Magaud, L. Numerical studies of confined states in rotated bilayers of graphene. *Physical Review B* **86,** 125413 (2012). https://doi.org/10.1103/PhysRevB.86.125413.

80. Fang, S. & Kaxiras, E. Electronic structure theory of weakly interacting bilayers. *Physical Review B* **93,** 235153 (2016). https://doi.org/10.1103/PhysRevB.93.235153.

81. Tong, Q. *et al.* Topological mosaics in moiré superlattices of van der Waals heterobilayers. *Nature Physics* **13,** 356–362 (2017). https://doi.org/10.1038/nphys3968.

82. Carr, S. *et al.* Twistronics: Manipulating the electronic properties of two-dimensional layered structures through their twist angle. *Physical Review B* **95,** 075420 (2017). https://doi.org/10.1103/PhysRevB.95.075420.

83. Wu, F., Lovorn, T., Tutuc, E. & MacDonald, A. H. Hubbard Model Physics in Transition Metal Dichalcogenide Moiré Bands. *Physical Review Letters* **121,** 026402 (2018). https://doi.org/10.1103/PhysRevLett.121.026402.

84. McGilly, L. J. *et al.* Visualization of moiré superlattices. *Nature Nanotechnology* **15,** 580–584 (2020). https://doi.org/10.1038/s41565-020-0708-3.

85. Anderson, E. *et al.* Programming correlated magnetic states with gate-controlled moiré geometry. *Science* **381,** 325–330 (2023). https://doi.org/10.1126/science.adg4268.

86. Nagaosa, N. & Tokura, Y. Topological properties and dynamics of magnetic skyrmions. *Nature Nanotechnology* **8,** 899–911 (2013). https://doi.org/10.1038/nnano.2013.243.

87. Zhang, Y., Liu, T. & Fu, L. Electronic structures, charge transfer, and charge order in twisted transition metal dichalcogenide bilayers. *Physical Review B* **103,** 155142 (2021). https://doi.org/10.1103/PhysRevB.103.155142.

88. Devakul, T., Crépel, V., Zhang, Y. & Fu, L. Magic in twisted transition metal dichalcogenide bilayers. *Nature Communications* **12,** 6730 (2021). https://doi.org/10.1038/s41467-021-27042-9.

89. Foutty, B. A. *et al.* Mapping twist-tuned multiband topology in bilayer WSe_2. *Science* **384,** 343–347 (2024). https://doi.org/10.1126/science.adi4728.

90. Handa, T. *et al.* Spontaneous exciton dissociation in transition metal dichalcogenide monolayers. *Science Advances* **10,** eadj4060 (2024). https://doi.org/10.1126/sciadv.adj4060.

91. Zhang, C. *et al.* Interlayer couplings, Moiré patterns, and 2D electronic superlattices in MoS_2/WSe_2 hetero-bilayers. *Science Advances* **3,** e1601459 (2017). https://doi.org/10.1126/sciadv.1601459.

92. Arovas, D. P., Berg, E., Kivelson, S. A. & Raghu, S. The Hubbard Model. *Annual Review of Condensed Matter Physics* **13,** 239–274 (Volume 13, 2022 2022). https://doi.org/10.1146/annurev-conmatphys-031620-102024.

93. Hubbard, J. Electron correlations in narrow energy bands. *Proceedings of the Royal Society of London. Series A. Mathematical and Physical Sciences* **276,** 238–257 (1997). https://doi.org/10.1098/rspa.1963.0204.

94. Huang, X. *et al.* Correlated insulating states at fractional fillings of the WS_2/WSe_2 moiré lattice. *Nature Physics* **17,** 715–719 (2021). https://doi.org/10.1038/s41567-021-01171-w.

95. Li, H. *et al.* Imaging local discharge cascades for correlated electrons in WS_2/WSe_2 moiré superlattices. *Nature Physics* **17,** 1114–1119 (2021). https://doi.org/10.1038/s41567-021-01324-x.

96. Wang, X. *et al.* Light-induced ferromagnetism in moiré superlattices. *Nature* **604,** 468–473 (2022). https://doi.org/10.1038/s41586-022-04472-z.

97. Wang, J. *et al.* Diffusivity reveals three distinct phases of interlayer excitons in $MoSe_2/WSe_2$ heterobilayers. *Physical Review Letters* **126,** 106804 (2021). https://doi.org/10.1103/PhysRevLett.126.106804.

98. Park, H. *et al.* Dipole ladders with large Hubbard interaction in a moiré exciton lattice. *Nature Physics* **19,** 1286–1292 (2023). https://doi.org/10.1038/s41567-023-02077-5.

99. Miao, S. *et al.* Strong interaction between interlayer excitons and correlated electrons in WSe_2/WS_2 moiré superlattice. *Nature Communications* **12,** 3608 (2021). https://doi.org/10.1038/s41467-021-23732-6.

100. Li, E. *et al.* Lattice reconstruction induced multiple ultra-flat bands in twisted bilayer WSe_2. *Nature Communications* **12,** 5601 (2021). https://doi.org/10.1038/s41467-021-25924-6.

101. Shabani, S. *et al.* Deep moiré potentials in twisted transition metal dichalcogenide bilayers. *Nature Physics* **17,** 720–725 (2021). https://doi.org/10.1038/s41567-021-01174-7.

102. Li, T. *et al.* Quantum anomalous Hall effect from intertwined moiré bands. *Nature* **600,** 641–646 (2021). https://doi.org/10.1038/s41586-021-04171-1.

103. Zhao, W. *et al.* Gate-tunable heavy fermions in a moiré Kondo lattice. *Nature* **616,** 61–65 (2023). https://doi.org/10.1038/s41586-023-05800-7.

104. Parker, J. H., Feldman, D. W. & Ashkin, M. Raman scattering by silicon and germanium. *Physical Review* **155,** 712–714 (1967). https://doi.org/10.1103/PhysRev.155.712.

105. Rahman, S., Sun, X., Zhu, Y. & Lu, Y. Extraordinary phonon displacement and giant resonance Raman enhancement in WSe_2/WS_2 moiré heterostructures. *ACS Nano* **16,** 21505–21517 (2022). https://doi.org/10.1021/acsnano.2c10092.

106. Liang, L. *et al.* Low-frequency shear and layer-breathing modes in Raman scattering of two-dimensional materials. *ACS Nano* **11,** 11777–11802 (2017). https://doi.org/10.1021/acsnano.7b06551.

107. Lui, C. H. *et al.* Observation of interlayer phonon modes in van der Waals heterostructures. *Physical Review B* **91,** 165403 (2015). https://doi.org/10.1103/PhysRevB.91.165403.

108. Yuan, L. *et al.* Twist-angle-dependent interlayer exciton diffusion in WS_2–WSe_2 heterobilayers. *Nature Materials* **19,** 617–623 (2020). https://doi.org/10.1038/s41563-020-0670-3.

109. Lin, K.-Q. *et al.* Large-scale mapping of moiré superlattices by hyperspectral Raman imaging. *Advanced Materials* **33,** 2008333 (2021). https://doi.org/10.1002/adma.202008333.

110. Zeng, H. *et al.* Optical signature of symmetry variations and spin-valley coupling in atomically thin tungsten dichalcogenides. *Scientific Reports* **3,** 1608 (2013). https://doi.org/10.1038/srep01608.

111. Placzek, G. *The Rayleigh and Raman Scattering* 218 pp. Google Books: UCNbiA6QDm0C (United States Atomic Energy Commission, Division of Technical Information, 1962).

112. Zhu, B., Chen, X. & Cui, X. Exciton binding energy of monolayer WS_2. *Scientific Reports* **5,** 9218 (2015). https://doi.org/10.1038/srep09218.

113. Lee, S. *et al.* Achieving near-perfect light absorption in atomically thin transition metal dichalcogenides through band nesting. *Nature Communications* **14,** 3889 (2023). https://doi.org/10.1038/s41467-023-39450-0.

114. Zhao, W. *et al.* Evolution of electronic structure in atomically thin sheets of WS_2 and WSe_2. *ACS Nano* **7,** 791–797 (2013). https://doi.org/10.1021/nn305275h.

115. *Light Scattering in Solids II* (eds Cardona, M. & Güntherodt, G.) (Springer, Berlin, Heidelberg, 1982).

116. Miller, B. *et al.* Tuning the Fröhlich exciton-phonon scattering in monolayer MoS_2. *Nature Communications* **10,** 807 (2019). https://doi.org/10.1038/s41467-019-08764-3.

117. Shimazaki, Y. *et al.* Strongly correlated electrons and hybrid excitons in a moiré heterostructure. *Nature* **580,** 472–477 (2020). https://doi.org/10.1038/s41586-020-2191-2.

118. Smoleński, T. *et al.* Interaction-induced Shubnikov–de Haas oscillations in optical conductivity of monolayer $MoSe_2$. *Physical Review Letters* **123,** 097403 (2019). https://doi.org/10.1103/PhysRevLett.123.097403.

119. Back, P. *et al.* Giant paramagnetism-induced valley polarization of electrons in charge-tunable monolayer $MoSe_2$. *Physical Review Letters* **118,** 237404 (2017). https://doi.org/10.1103/PhysRevLett.118.237404.

120. Dong, J., Wang, J., Ledwith, P. J., Vishwanath, A. & Parker, D. E. Composite Fermi liquid at zero magnetic field in twisted $MoTe_2$. *Physical Review Letters* **131,** 136502 (2023). https://doi.org/10.1103/PhysRevLett.131.136502.